

中九龍 幹線

Central Kowloon Route

九龍灣臨時填海工程

之具有力和令人信服的資料

二零一三年二月



路政署
Highways Department

路政署
合約編號 CE 43/2010 (HY)
中九龍幹線 – 設計及施工
九龍灣臨時填海工程
具有力和令人信服的資料

217722-REP-044-02
修正終稿 | 2013 年 2 月

目錄

	頁
1 前言	1
背景	1
九龍灣內的海底隧道	1
保護海港條例	1
報告結構	2
2 凌駕性公眾需要	2
引言	2
交通方面的理據	2
項目的效益	7
結論	8
3 沒有合理的不涉及填海的替代方案	9
引言	9
設計及施工安排的限制	9
不需填海之建造方案	10
使用填海的建造方法	14
替代走線	16
4 最少範圍的臨時填海	18
引言	18
填海的長度	18
填海的寬度	18
臨時填海的時間	19
最少填海要求的總結	19
5 公眾諮詢	20
前階段的公眾參與活動	20
2009年7月18日公眾論壇	20
2009年6月20日焦點小組會議	20
公眾參與活動結論	20
現階段的公眾參與活動	20
現時有關中九龍幹線的公眾意見	21
諮詢區議會	21
諮詢海濱事務委員會	21
九龍灣臨時填海專業論壇	21
九龍灣臨時填海專題討論	22

6 結論	23
有關臨時填海的凌駕性公眾需要	23
沒有合理而不涉及填海工程的建造方式	23
最小的填海範圍	23
第二期公眾參與活動	23
獨立專家審查	23
符合保護海港條例	23

附錄

附錄一

林興強教授 - 關於九龍灣臨時填海工程具有力和令人信服的材料報告之獨立專家審查

附錄二

吳宏偉教授 - 關於九龍灣臨時填海工程具有力和令人信服的材料報告之獨立專家審查

1 前言

背景

1.1 中九龍幹線全長 4.7 公里，採用雙程三線分隔車道的設計，連接西九龍的油麻地交匯處與東九龍的啟德發展區及九龍灣道路網，成為貫通中九龍的快速道路。中九龍幹線總平面圖及縱剖面請見圖 1-1。

1.2 於 2007 年至 2009 年間的勘測和初步設計階段中，我們曾研究 40 多個中九龍幹線的走線方案。在比較各方案對區內樓宇、社區設施、環境、土地及交通方面的影響，參考公眾參與活動中所收到的公眾意見後，選取現時的走線。立法會、油尖旺、九龍城和觀塘區議會均普遍支持選定的走線。

九龍灣內的海底隧道

1.3 幹線由九龍城碼頭至啟德發展區有一段長約 370 米的隧道會經過九龍灣海床。由於現場的種種限制，該段隧道需以臨時填海方法建造。



圖 1-1 - 中九龍幹線的走線

保護海港條例

不准填海的推定

1.4 《保護海港條例》源自 1996 年保護海港協會以私人法案形式呈交立法局，該草案於 1997 年 6 月正式通過成為法例，並經法律程序一再修訂，《保護海港條例》藉設定不准在海港內進行填海工程的推定，以達致保護和保存海港的目的，再於 1999 年 12 月修訂至涵蓋整個維港的範圍。

1.5 條例第三條規定：

- (1) 海港須作為香港人的特別公有資產和天然財產而受到保護和保存，而為此目的，現設定一個不准進行海港填海工程的推定。[第 3 條(1)段]
- (2) 所有公職人員和公共機構在行使任何歸屬他們的權力時，須顧及第(1)款所述的原則以作為指引。[第 3 條(2)段]

1.6 《保護海港條例》將『填海』明確地定義為『任何為將海床或前濱海形成為土地而進行或擬進行的工程』，條例中『填海』的釋義是針對所形成土地，意思可推斷為超越海平面的工程。故此，縱使進行只有小規模填海要求的工程，例如興建碼頭、登岸梯級等，亦需要符合《保護海港條例》。

城市規劃委員會對保護海港協會有限公司案件的終審法院判決(2004 年 1 月 9 日)

1.7 城市規劃委員會曾於 2002 年 12 月及 2003 年 2 月就灣仔北分區計劃大綱草圖（編號 5/H25/1）作出決定，包括在維港範圍內填海的建議。保護海港協會就該決定經司法程序提出反對，認為城市規劃委員會作出非法、不合理及不合乎邏輯的決定，該反對意見在高等法院的聆訊中獲判勝訴。

1.8 在 2004 年 1 月 9 日終審法院的判決中，上訴被駁回。終審法院裁定—

- (a) 為了貫徹保護和保存海港這個強而有力的法定原則，不准許進行海港填海工程的推定，只能被具有凌駕性公眾需要的填海工程所推翻。這可以稱為“凌駕性公眾需要的測試”；
- (b) 如果還有其他合理解決方法，就不能把填海工程說成有凌駕性需要。因為當其他合理解決方法可以滿足公眾需要的時候，就沒有所謂的凌駕性需要；以及
- (c) 所建議的填海工程範圍，不應超越凌駕性需要所要求的最低限度。

1.9 公眾需要將是社區的需要，包括社區對經濟、環境和社會的需要。只有迫切和即時的需要方可稱為凌駕性需要。這個需要必須令人信服，也就是實際上有必要去凌駕公眾保護和保存海港的強烈需要。這個需要必須是即時的需要，並且在規劃時已經考慮到的一個在明確和合理的時間內將出現的需要。如果這個需要不會在一定時間內出現，就不足以推翻不准填海的推定了。當前迫切的需要，是遠遠超越那些「人們樂於擁有的」、「應有的」、「可取的」或「有益的」事物。但另一方面，亦未達到「非到

最後才會需要」或公眾「不可或缺」的地步。當前的需要是顧及規劃工作的時間表，在確實而合理的時間內會出現的需要。

1.10 判詞亦指出，當有另一個合理的方案可取代填海，填海工程則不具凌駕性公眾需要。所有情況均應一併考慮，包括每個方案對經濟、環境和社會方面所造成的影響，並要顧及所涉及的成本、時間和引致的延誤。建議的填海範圍，不應超越為符合凌駕性需要所要求的最低限度，每個建議的填海範圍均必須具備理據。

1.11 要符合凌駕性公眾需要測試的準則，公職人員或公共機構必須以有力和令人信服的資料證明填海是具凌駕性公眾需要。

保護海港協會對律政司司長案件的原訟法庭一審判決(2008年3月20日)

1.12 政府擬建的中環灣仔繞道是一條沿香港島北岸而建的幹道，以疏導現有東西走廊的交通。興建中環灣仔繞道的一段明挖回填式隧道，需要在灣仔前公眾貨物裝卸區及銅鑼灣避風塘進行臨時填海。臨時填海預計會維持約 6 年。工程完成後，將臨時填海及將海床回復原狀。政府當時認為，此臨時填海工程毋須受到《保護海港條例》的約束。

1.13 保護海港協會向高等法院提出訴訟的理據是《保護海港條例》並沒有明確分辨形成永久土地的填海和臨時填海的分別。保護海港協會尋求作出澄清，即使填海屬過渡性質，甚至是為了避免永久性填海，填海工程仍須符合不准填海的推定，除非能通過「凌駕性公眾測試」去說明其需要性，否則不可合法地進行。

1.14 原訟法庭判保護海港協會勝訴，並重申《保護海港條例》和不准填海的推定適用於中環灣仔繞道計劃中建議的臨時填海工程。

報告結構

1.15 本報告包括具有力和令人信服的資料，以證明興建中九龍幹線的海底隧道所建議在九龍灣的臨時填海工程，符合“保護海港條例”的要求。本報告根據 2004 年 8 月 19 日房屋及規劃地政局發出的技術通告第 1/04 號而準備。技術通告是為公職人員和公共機構在考慮及批准填海建議前提供準則，包括對臨時填海工程在公眾諮詢過程裡的資料。

1.16 本報告的後部分內容如下-

- (a) **第 2 部分**提供支持中九龍幹線工程凌駕性公眾需要的資料和評估;
- (b) **第 3 部分**說明建議在九龍灣的臨時填海沒有合理的替代方案;
- (c) **第 4 部分**闡述建議的填海工程的範圍將會是最低限度;
- (d) **第 5 部分**描述為臨時填海工程所進行的公眾諮詢，並總結了公眾的意見;及
- (e) **第 6 部分**提出對臨時填海工程的結論，並描述推薦的方案。

2 凌駕性公眾需要

引言

2.1 房屋及規劃地政局技術通告第 1/04 的準則，提供了中九龍幹線工程的凌駕性公眾需要之評估方法。技術通告指出，第一個步驟是，確定項目是否有迫切和即時的公眾需要。“公眾需要”被定義為社區的經濟、環境和社會需要。社區的需要是指大眾至需要的，而不是滿足小一部分人的特別需求和利益。

2.2 根據房屋及規劃地政局技術通告 1/04 中所說“令人信服的”是指具有必要的力量去壓倒公眾保護和保存海港的強烈需要。這是需要被有力和令人信服的資料支持（例如研究結果，預測，成本和效益分析等），以支持填海工程項目的凌駕性需要。

2.3 “目前需要”這個詞被定義為證明在一個明確和合理的時間框架內將出現的需要。要滿足這一點，必須有一個具體的實施方案和堅定承諾並獲得有關政府部門的、與相關部門的認可（如適用）。

2.4 下面介紹中九龍幹線目前迫切的公共需要，將提供給香港社會的利益：

交通方面的理據

(一) 概覽

2.5 現時連接九龍東西主要幹道的交通，包括龍翔道，界限街，太子道西，亞皆老街，窩打老道，加士居道行車天橋及漆咸道北已接近飽和，交通擠塞時有發生。該區政府已實施交通管理及改善措施。然而，由於現有的東西幹道兩端都是高度發展的地區，近乎沒有可改善交通的空間。因此，這些措施只能在短期內紓緩該區的交通問題。

2.6 擬建的中九龍幹線是一條貫通九龍半島的三線雙程主幹路，連接西面的西九龍與東面的啟德發展區。幹線的西面出口連接西九龍油麻地交匯處。經由交匯處，車輛就可以分別前往西區海底隧道、尖沙咀、西九龍文化區、西九龍公路、8 號幹線和 3 號幹線。東面出口在啟德發展區，然後分別連接到九龍灣，東九龍，觀塘繞道，將軍澳隧道，T2 道路和將軍澳 - 藍田隧道。中九龍幹線連同 T2 道路及將軍澳 - 藍田隧道將形成一個策略性道路網，即 6 號幹線，連接西九龍和將軍澳。

2.7 中九龍幹線西面的西九龍文娛藝術區和東面的啟德發展區均已取得長足發展，隨著這些發展的階段性完成，對在九龍區內連接東西策略性道路和關鍵匯合處的交通產生顯著影響。

2.8 早在二十年前，已確證需要有一條直接連接東西九龍的交通路線，以應付橫跨九龍的交通需求及紓緩現時九龍中部交通擠塞的狀況。往後的幾年裡，隨著西九龍，九龍灣及將軍澳的發展，交通量不斷增長，橫貫九龍的交通需求也有所增加。為廣大公眾和道路使用者提供一條可以紓緩擠塞的東西方向道路的需求，已是刻不容緩；而興建中九龍幹線便能滿足這需求。此外，如圖 2-1 所示，擬建的啟德發展區及西九龍文娛藝術區的發展無疑進一步加大了對幹線的需求。



圖 2-1 - 未來東西九龍的發展項目

2.9 東西九龍之間的道路交通，目前是由龍翔道，界限街，太子道，亞皆老街，窩打老道和漆咸道北組成。除了龍翔道及加士居道天橋外，這些現有的東西方向道路，經常被頻密的道路交界處和信號控制的路口限制了交通流量。根據在 2011 年進行的綜合交通調查，對現有的路口和道路的表演作基線研究，以及現有的交通問題進行了匯總。我們還注意到在 2011 年交通統計年報，超過 60%往返東西九龍的車輛交通（圖 2-2 中的交通調查線 A-A）是商用車（即的士，公共小巴，貨車，旅遊車和巴士）。



圖 2-2 - 九龍區的現有道路的服務水平

2.10 現有的主要東西公路走廊（龍翔道，太子道西及界限街），一直被交通容量不足的問題所困擾。部分歸結為最近幾年九龍半島和新界的西部（如西九龍填海區，大嶼山）和東部（如將軍澳）的物業發展迅速，而沒有提升的交通容量導致交通出現容量不足的情況。一些交通擠塞的實例顯示在圖 2-3。



圖 2-3 - 九龍中、西部現有的交通狀況

2.11 其中許多道路走廊已經達到了繁忙時間的交通設計可承載能力，例如，在繁忙時間於太子道西及界限街的方向流量，達到的行車量/容車量比率分別為 0.8 和 1.1，顯示已接近或超過承載的能力。2011 年西九龍及東九龍的行車量/容車量的比率總結在下列表 2-1。

表 2-1 在 2011 年東西九龍關鍵道路的表現

道路	方向	行車量/容車量比率 (V/C)	
		2011 (現有道路)	
		上午	下午
龍翔道 (從獅子山隧道路至竹園路)	東行	0.9	0.8
	西行	0.9	0.9
	西行 (竹園道支路)	0.9	0.6
界限街 (從大坑東道至基堤道)	東行	1.0	1.1
太子道西 (從基堤道至嘉道理道)	西行	0.8	0.7
亞皆老街 (從嘉齡道至天光道)	東行	0.8	0.9
	西行	0.8	0.8
窩打老道 (碧街至登打士街)	北行	0.9	1.0
	南行	0.9	0.7

道路	方向	行車量/容車量比率 (V/C)	
		2011 (現有道路)	
		上午	下午
加士居道天橋 (彌敦道東側)	東行	0.8	>1.3
	西行	1.2	1.1
漆咸道北 (從蕪湖街至平治街)	東行	1.1	1.1
	西行	0.8	1.2
	西行 (遠側的自由流通車道)	1.3	0.4
東九龍走廊 (從馬頭角道至漆咸道北)	東行	1.0	1.1
	西行	0.8	0.6

說明:

行車量/容車量比率 (V/C) 是一個指標，它反映的道路性能。一個 V/C 比等於或低於 1.0，表示道路有足夠的能力，以應付車輛交通量的考慮，所產生的交通暢順。V/C 比率高於 1.0，則表示交通開始擠塞；高於 1.2 則表示更嚴重的交通擠塞與流量的進一步增加，速度會逐漸減慢。

2.12 中九龍幹線將提供一個新的路線，繞開堵塞的道路網絡，從而顯著地減少行車時間。據估計在 2021 年，於繁忙時間內，使用中九龍幹線從西九龍到東九龍的行車時間只需要約 5 分鐘，而沒有中九龍幹線的行車時間則需要 30-35 分鐘。中九龍幹線也將大大減少在主要東西走廊上的行車量，紓緩交通擠塞。因路面的交通情況顯著改善，鄰近地區包括黃大仙、何文田及九龍城也將受惠。

2.13 中九龍幹線也將與東西九龍的高速道路網連接，成為策略性道路網的重要組成部分。在這方面，東面的啟德交匯處將連接中九龍幹線和九龍灣的道路網絡，從而提高了觀塘及啟德發展區與西九龍之間的交通便利，以及為政府提出的起動九龍東計劃提供基礎交通設施配套。中九龍幹線將會與在啟德發展區擬建中的 T2 主幹路，以及將軍澳-藍田隧道，組成全長 12.5 公里的 6 號幹線，直接連繫西九龍和將軍澳。

2.14 在中九龍幹線西面的油麻地交匯處有四通八達的支路連接西九龍公路及連翔道。車輛可經西九龍公路，南往香港島西部，西至香港國際機場和葵涌貨櫃碼頭，北行前往新界西北。車輛亦可經連翔道進出西九龍發展區、廣深港高速鐵路(XRL)西九龍站及西九龍文化區。

2.15 以下段落總結了在九龍東、西和中部發現的交通問題。

(二) 西九龍的交通情況

2.16 在西九龍內區的各交界處 (如柯士甸道西/柯士甸道/廣東道，連翔道/佐敦道，廣東道/匯翔道) 觀察到的總流量可見，交通主要由往返住宅及辦公樓的活動形成，故此一般在週一至週五的繁忙時間最為明顯。在更主要的路口，一些車龍主要從下游的交界處伸延，例如，在佐敦道東行進入佐敦道/渡船街/廣東道交界處，在週六中午繁忙時間車龍已延伸到連翔道/佐敦道交界處。

2.17 從加士居道的道路聯絡能力評估的結果顯示，加士居道天橋東行和西行的長車龍也影響車輛通過該路段的實際需求。從觀察得知，在加士居道天橋上，東行和西行的車龍最遠分別可及窩打老道和佛光街。

(三) 中九龍的交通情況

2.18 九龍半島中央部分的道路網的特點是由東西和南北道路基本上組成一個網格的形式。在目前的研​​究中特別值得關注的是在道路等級制度中較高級的道路，即幹道、主要幹路和地區支路，對跨區交通提供高吞吐能力具有重要的作用。

2.19 雖然上述的一些道路在規劃時被列為主要支路，主要負責跨區的交通，但事實上，由於某些原因，這些道路有一定行車量是來自地區性的交通。

2.20 中九龍區的路口一般都在平日高峰時段比較繁忙（例如柯士甸道/漆咸道南/暢運道路口，亞皆老街/彌敦道路口，亞皆老街/窩打老道/公主道路口，亞皆老街/洗衣街路口及漆咸道北/蕪湖街路口）。車龍的長度還顯示，大部分東西向道路的關鍵路口，如太子道西及界限街，平日的車龍比週末的繁忙時間還要長。

2.21 在亞皆老街/洗衣街路口與亞皆老街/染布房街路口也觀察到長車龍。根據觀察，在平日和週末的時間，洗衣街北行線/旺角道路口的車龍，會影響實際需要通過亞皆老街/洗衣街路口的車輛。因為車龍的影響，該路口在週末計算出的剩餘容車輛將高於平日。同樣在亞皆老街/染布房街路口，亞皆老街西行到亞皆老街/洗衣街路口的車龍也將影響到實際需要通過在亞皆老街/染布房街路口的車輛。洗衣街與染布房街之間的亞皆老街行車道的短距離是限制因素之一，也加劇了道路網絡的車龍問題。

2.22 行車時間調查的結果也顯示，沿中九龍區的重要道路（即界限街，太子道西，佐敦道）在上午和下午繁忙時間，平均的行駛時速慢於其他重要道路。這主要是受交界處停車（例如渡船街/窩打老道路口及亞皆老街/塘尾道路口）進出大廈影響。

(四) 東九龍的交通情況

2.23 東九龍區的道路網的特點是一系列密集的主要道路，呈西北-東南方向走向(啟德隧道-啟福道走廊、觀塘繞道、太子道東-觀塘道走廊和清水灣道走廊)並接近垂直相交；三條策略性道路，即龍翔路，將軍澳隧道及東區海底隧道，以及一些支路。目前的研究特別關注的 T2 主幹路，即上述那一類西北-東南方向的主要道路，因為 T2 主幹路亦能紓緩這些道路的交通狀況。另外，九龍灣內的道路和路口會包括在啟德機場南停機坪的道路和發展的研究裡，因為這些道路將直接連接南停機坪與啟德發展區外的地區。

2.24 在東九龍區的道路交匯處，由於交通來自工業和商業的活動，所以在週一至週五的繁忙時間最為繁忙。然而，在路口的通行能力評估結果顯示，這些關鍵的路口，除了偉業街/偉發道路口超負荷運作之外，在週一至週五的繁忙時間仍然在可接受的水平運作；該路口的超負荷運作源於通過該路口觀塘繞道往觀塘及藍田區的繁忙交通流量而成。

(五) 道路網絡可靠性

2.25 如圖 2-4 所示，於 2005 年 5 月 9 日在太子道東發生了一宗棚架倒塌的重大意外，由於這太子道東是其中一條最重要的東西走廊，事故導致整個九龍區的交通嚴重癱瘓。



圖 2-4 - 2005 年 5 月 9 日在太子道東發生的棚架倒塌事故

2.26 擬建的中九龍幹線，可以作為九龍中部東行及西行線車輛的緊急走廊。2005 年 6 月公布的“緊急事故交通協調工作組報告”中指出，由於惡劣天氣狀況，九龍中部東行及西行的交通受到嚴重影響。工作組還表示，在九龍南北方向的交通較為發達，但東西方向的道路依然有不足之處。他們認為有需要增加東西方向道路的行車容量。

(六) 交通管理措施

2.27 即使政府已實施了一些地區性的交通管理和改善措施，然而，由於現有的東西幹道兩端都是高度發展的地區，幾乎沒有改善的空間。因此，這些措施只能在短期內紓緩該區的交通問題。為了有效解決九龍中部東西行的交通問題，應盡快落實中九龍幹線的工程以提供另一條替代路線，繞開堵塞的路段並增加東西走廊的容車量。

(七) 交通預測

2.28 交通研究預測在沒有中九龍幹線的情況下東西走廊行車量增加的後果。2021 年的交通量預測已考慮了新的土地利用總體規劃假設及人口預測，以確保交通量預測是符合目前的戰略和地方的規劃意向，以上種種證實了對幹線的需要性。第三次整體運輸研究(CTS 3)，基礎區域交通模型(BDTM) 及區域性人口及就業矩陣(TPEDM) 都用來參考和審視有和沒有中九龍幹線對該區的交通狀況。

2.29 如圖 2-5 所示，在沒有中九龍幹線的情況下，未來的交通狀況在 2021 年預期將會變得惡劣。表 2-2 總結了在 2021 年有和沒有中九龍幹線的情況下東西走廊的表現。



圖 2-5 - 2021 年在東西九龍的交通狀況

道路	方向	行車量/容車量比率 (V/C)			
		2021(沒有中九龍幹線)		2021(有中九龍幹線)	
		上午	下午	上午	下午
漆咸道北 (從蕪湖街至平治街)	東行	1.3	1.2	1.1	1.0
	西行	1.0	1.2	1.0	0.7
	西行 (遠邊自由流動車道)	1.3	0.9	1.1	1.1
東九龍走廊 (從馬頭角道至漆咸道北)	東行	1.3	1.3	1.1	1.1
	西行	0.7	0.7	1.1	1.0
中九龍幹線	東行	-	-	0.6	0.7
	西行	-	-	0.7	0.6

說明:
行車量/容車量比率 (V/C) 是一個指標, 它反映的道路性能。一個 V/C 比等於或低於 1.0, 表示道路有足夠的能力, 以應付車輛交通量的考慮, 所產生的交通暢順。V/C 比率高於 1.0, 則表示交通開始擠塞; 高於 1.2 則表示更嚴重的交通擠塞與流量的進一步增加, 速度會逐漸減慢。

2.30 在一般情況下, 如果 2021 年沒有中九龍幹線的話, 現有的主要路線的服務水平預計保持在“F” - “爬行駕駛速度”, 而如果 2021 年有中九龍幹線, 服務水平會提高到“D” - “降低駕駛速度”(參考圖 2-2)。

2.31 主要路口的剩餘容車量, 表 2-3 及圖 2-6 簡介現有情況, 2021 年有中九龍幹線情況和 2021 年沒有中九龍幹線情況的表現。

表 2-2 在 2021 年關鍵的行車量/容車量的有關東西道路總結

道路	方向	行車量/容車量比率 (V/C)			
		2021(沒有中九龍幹線)		2021(有中九龍幹線)	
		上午	下午	上午	下午
龍翔道 (從獅子山隧道至竹園路)	東行	1.2	1.1	0.9	1.0
	西行	1.0	1.0	0.9	0.8
	西行(支路從竹園道)	1.1	0.6	0.9	0.5
界限街 (從大坑東道至基堤道)	東行	1.2	1.3	0.9	0.9
太子道西 (從基堤道至嘉道理道)	西行	1.1	0.8	0.9	0.7
亞皆老街 (從嘉齡道至天光道)	東行	1.1	1.0	0.7	0.7
	西行	1.1	0.9	0.7	0.8
亞皆老道 (從皮特街至登打士街)	北行	1.0	0.9	1.0	0.9
	南行	1.2	0.8	1.1	0.7
加士居道天橋 (彌敦道東側)	東行	1.3	>1.3	1.1	1.2
	西行	1.3	1.3	1.1	1.2

表 2-3 主要路口的表現

路口	2011 年	2021 年沒有中九龍幹線	2021 年中九龍幹線
界限街 / 窩打老道	10%	-10%	20%
太子道西 / 窩打老道	10%	-20%	20%
太子道西 / 嘉道理道	20%	-10%	10%
亞皆老街 / 彌敦道	10%	-20%	10%
漆咸道北 / 蕪湖街	-10%	-20%	5%

2.32 在 2021 年沒有中九龍幹線的情況下, 全部的剩餘容車量數目都變負值。這表示路口沒有剩餘容車能力, 及交通擠塞的情況將會惡化。

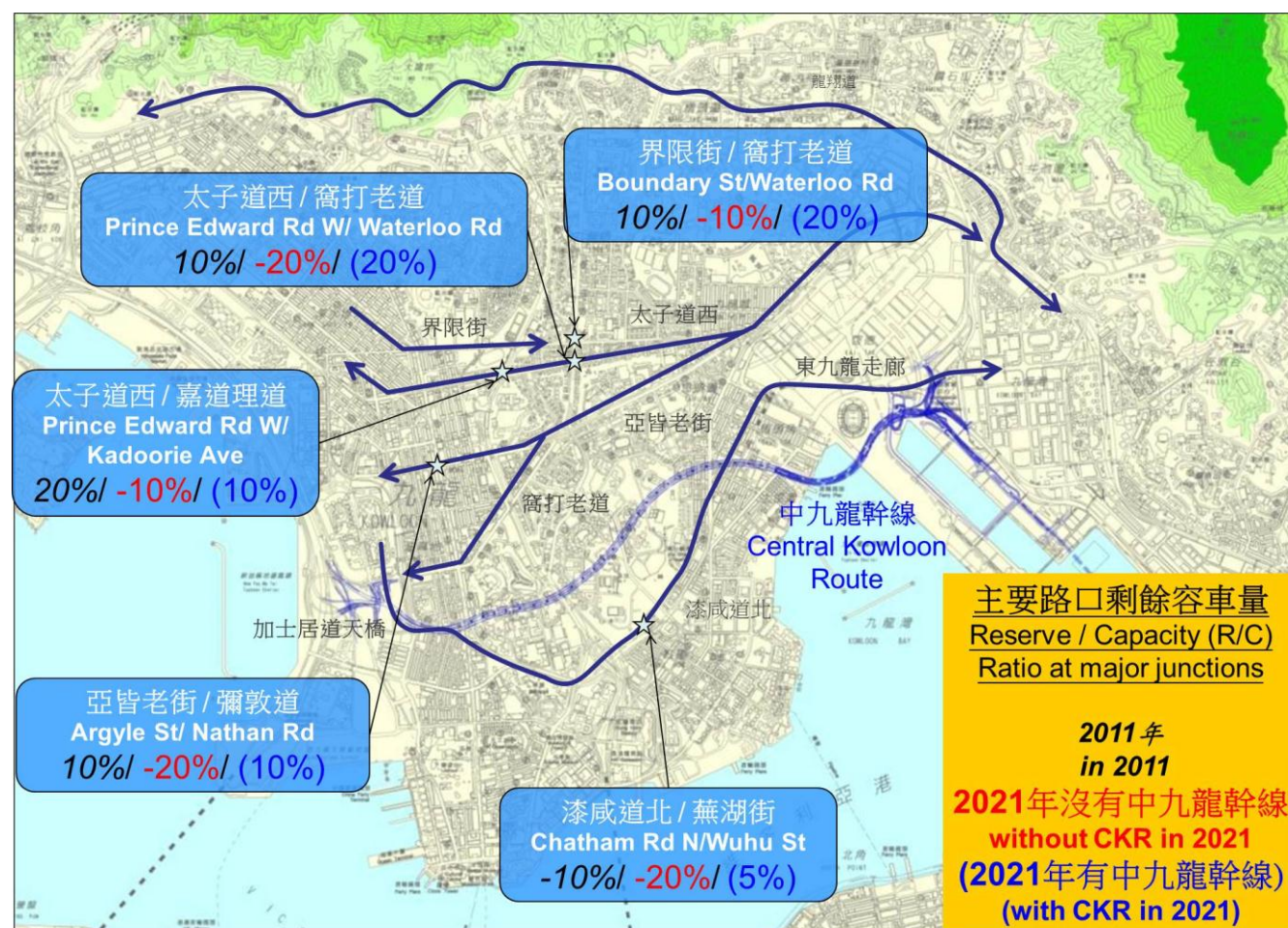


圖 2-6 - 九龍主要路口剩餘容車量

項目的效益

(一) 經濟效益

2.37 中九龍幹線主要的經濟效益是節省行駛時間和路程，令乘客直接受惠，可以享受更直接和快捷的旅程往返東西九龍。中九龍的交通同樣間接受惠（例如在窩打老道行駛），擠塞路線如亞皆老街，窩打老道及佐敦道的車輛將分流到中九龍幹線，令行駛的速度提高，並因此減少行車時間。雖然公共巴士所節省行車時間相對較小，但較高的車輛佔用率意味著公共交通節省的行車時間是總節省時間的一個重要組成部分。

2.38 預計在 2021 年，在早上繁忙時間，用中九龍幹線從西面到東面行車時間只需要約 5 分鐘，與沒有中九龍幹線的情況下節省約 25 至 30 分鐘。如果任何東西走廊被堵塞引致嚴重交通擠塞，中九龍幹線的重要性更高。

2.39 節省時間值是以相對每組乘客的節省時間(以小時)為單位，乘以該組時間價值 (VOT)。VOT 因此反映乘客為節省一小時的願付價格。對每組旅客 VOT 的評估是基於 2002 年的出行特徵調查，並折算成當前的價格。預計在 2030 年，節省的行車時間將會達到每日 12 萬旅客小時，每年帶來的經濟價值約為 26 億港元。

2.40 乘客從地面道路分流到隧道會減少交通意外。根據運輸署提供的交通意外統計，在 2006 年至 2010 年隧道的每公里車輛意外率比地面道路低 85%。

2.41 基於為期 48 年的預算，包括建設和營運期間，與假設的實際折扣率，中九龍幹線項目預計產生 195.03 億港元的淨現值，7.5% 的內部收益率和 1.8 的效益成本比率。分析可見，發展中九龍幹線的經濟效益足以支付開支及成本，因此中九龍幹線項目是經濟可行的。

(二) 環境效益

2.42 各條橫跨九龍半島的市區幹道接近或已超過其設計負荷能力，造成交通阻塞和長長車龍。中九龍幹線項目的主要目標是紓緩目前東西幹道在繁忙時間的交通擠塞；這些幹道包括龍翔道，界限街，太子道西，亞皆老街，窩打老道，加士居道行車天橋及漆咸道北。

2.43 中九龍幹線將現有連接東西九龍主要道路的交通分流，減少地面道路的車輛數目，從而紓緩交通擠塞所造成的污染，改善環境。

2.44 中九龍幹線通車後，這些連接東西九龍主要道路的交通情況（例如平均行駛速度）將能得到改善，這將導致減少污染物，如二氧化碳，氮氧化物和可吸入懸浮粒子等。

2.45 沿中九龍幹線而建的三座通風大樓，通過採用先進的技術，如空氣淨化系統 (APS)，靜電除塵器 (ESP) 和二氧化氮去除系統，令廢氣濃度大幅下降。

(八) 結論

2.33 現時來往九龍東西的主要道路交通已接近或已超出這些道路的容車輛，所以經常出現較交通擠塞情況。上期及近期的交通研究一直對東西走廊的交通需求預測增加，並確認需要一條額外的東西主幹線，以避免道路網會受到更廣泛、更頻繁的交通堵塞，甚至造成交通癱瘓。

2.34 2021 年的交通預測也確定雙程三線主幹路及其連接道路，從現有的東西走廊和區內道路網提供足夠的分流，疏導交通。

2.35 中九龍幹線將連接九龍東西兩端的高速公路，從而形成策略性道路網絡的一個重要組成部分。中九龍幹線會紓緩現有東西主幹道的交通擠塞。在 2021 年，用中九龍幹線來往西九龍與九龍灣的行車時間會從約 30-35 分鐘減至約 5 分鐘。

2.36 通過交通及運輸研究，建設中九龍幹線的需求已被確立。研究亦顯示，建設中九龍幹線是有當前迫切需要的。

2.46 連接東西九龍主要道路的 2021 年交通量預測已輸入環保署最新的 EmFAC-HK V2.1 軟件模型，它已反映了最新排放控制措施。中九龍幹線的環境影響評估（EIA）已使用同一個的 EmFAC 模型。EmFAC-HK 模型會考慮多項因素，包括交通流量，行駛速度，區域性車輛-公里-行駛（VKT），車輛組合等，以估計有關路段每年的二氧化碳，氮氧化物和可吸入懸浮粒子的總排放。在下面的表 2-4 中總結。

表 2-4 預計的年排放量為的主要的東西走廊

物質的廢氣排放	2021 年 中九龍幹線帶來的削減 ^[1] , 噸 / 年
二氧化碳	約 20,000
氮氧化物	約 18
可吸入懸浮粒子	約 2

^[1] 只考慮九龍區主要東西交通走廊

(三) 社會效益

2.47 未來中九龍幹線完工後，行車時間將會縮短，提高區域間的連接及支持社會發展。

結論

2.48 因為建設中九龍幹線以紓緩現時交通擠塞有迫切需要，及因為中九龍幹線可以改善環境，也可以帶來經濟及社會效益，證明建造中九龍幹線是有凌駕性公眾需要的。

3 沒有合理的不涉及填海的替代方案

引言

3.1 這部分會了解不用在九龍灣臨時填海建造海底隧道的可能性。我們先會考慮選定走線可不可以用不需臨時填海的其他合理方案建造海底隧道，然後再考慮其他不需要填海的走線。

設計及施工安排的限制

東端佈局

3.2 如圖 3-1 所示，鑽挖隧道會從油麻地開始，經過京士柏，何文田及馬頭圍，在地面以下約 40 米至 140 米深的岩石層建造，以確保中九龍幹線的建設和經營不會與大廈地基的樁柱相衝突，及確保走線上的大廈的正常用途。由於中九龍幹線會與九龍灣及啟德的道路網連接，豎向走線會從馬頭圍道東面以 4% 的坡度爬升。在九龍灣下的中九龍幹線縱截面如圖 3-1 所示。

3.3 因為 4% 坡度爬升的一段路超過 500 米長，此斜度根據交通規劃及設計手冊要求，隧道有 4 條東向行車道以提供一條給重型車輛用的爬坡車道。此外，由於在九龍灣的平面半徑為 330 米，東西線行車道，需要加闊最大 3 米以符合設計手冊，並給駕駛者一個足夠的安全視距。

3.4 施工方案是根據幾何功能性要求和已知的地質條件。對於一個非常深及闊的(大約 47 至 58 米)海底隧道結構來說，設計必定十分複雜及要求有一個完善的設計方案。

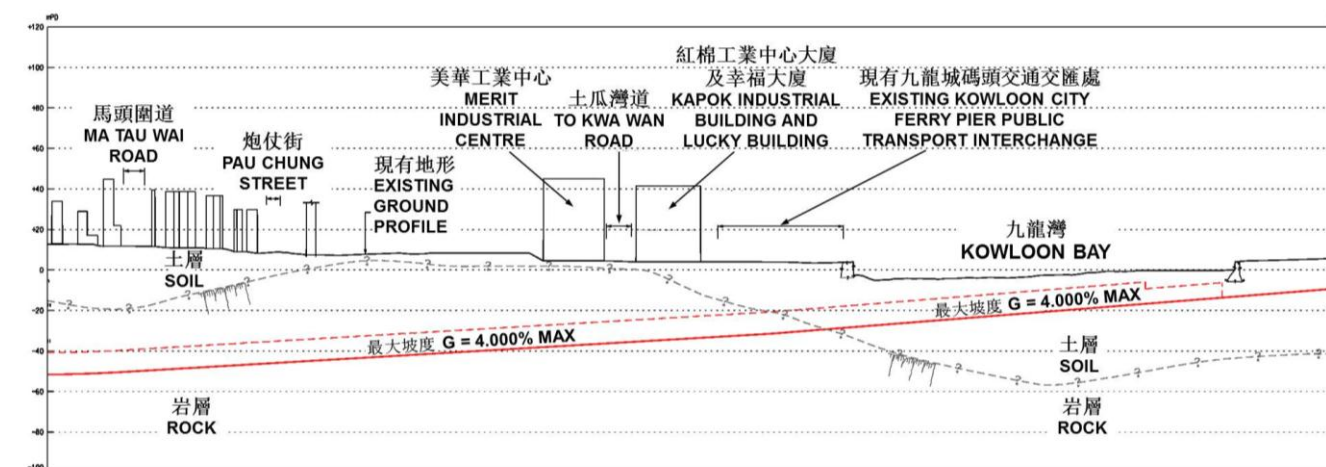
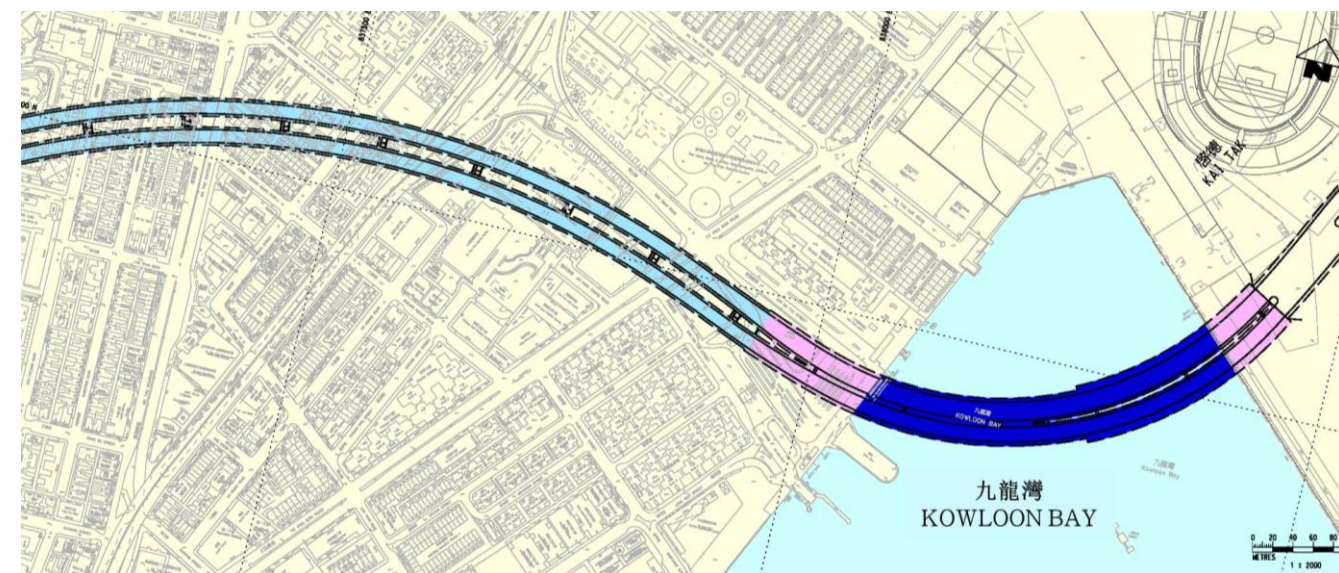


圖 3-1 – 東端佈局圖

九龍城渡輪碼頭

3.5 此碼頭供市民乘坐渡輪來往馬頭角及北角使用。工程會在碼頭的北面進行。為了保持正常的渡輪活動，將會實施合理的安排。

馬頭角公眾碼頭

3.6 由於建造中九龍幹線的海底隧道，需要拆卸馬頭角公眾碼頭。工程期間，公眾碼頭會在景雲街附近的海濱走廊臨時重置。工程完工後，碼頭會於原位重置。

香港中華煤氣有限公司 (HKCG) 石腦油碼頭

3.7 這碼頭正在被用來接收海運而來的石腦油，然後將之轉送到附近的香港中華煤氣有限公司馬頭角廠房。據香港中華煤氣有限公司表示，目前每年會輸送三十六次的海運石腦油。在施工期間，為了繼續正常裝運，海上通道將要維持。

不需填海之建造方案

3.8 我們已考慮下面兩種不需填海的建造方案來建設海底隧道：

- (a) 沉管式隧道 (IMT)；及
- (b) 隧道鑽挖機 (TBM)。

(一) 沉管式隧道 (IMT)

3.9 根據這方案，一個 220 米闊及 30 米深的坑道會跟著隧道走線在海床疏浚海泥（見圖 3-2）。隧道組件（大約 47 米至 58 米闊及 16.5 米高）會於場外預製然後浮拖到隧道走線及沉落坑道指定的位置。隧道連接後，坑道會回填到現有的海床。沉管隧道典型剖面及典型回填安排如圖 3-3 及圖 3-4 所示。

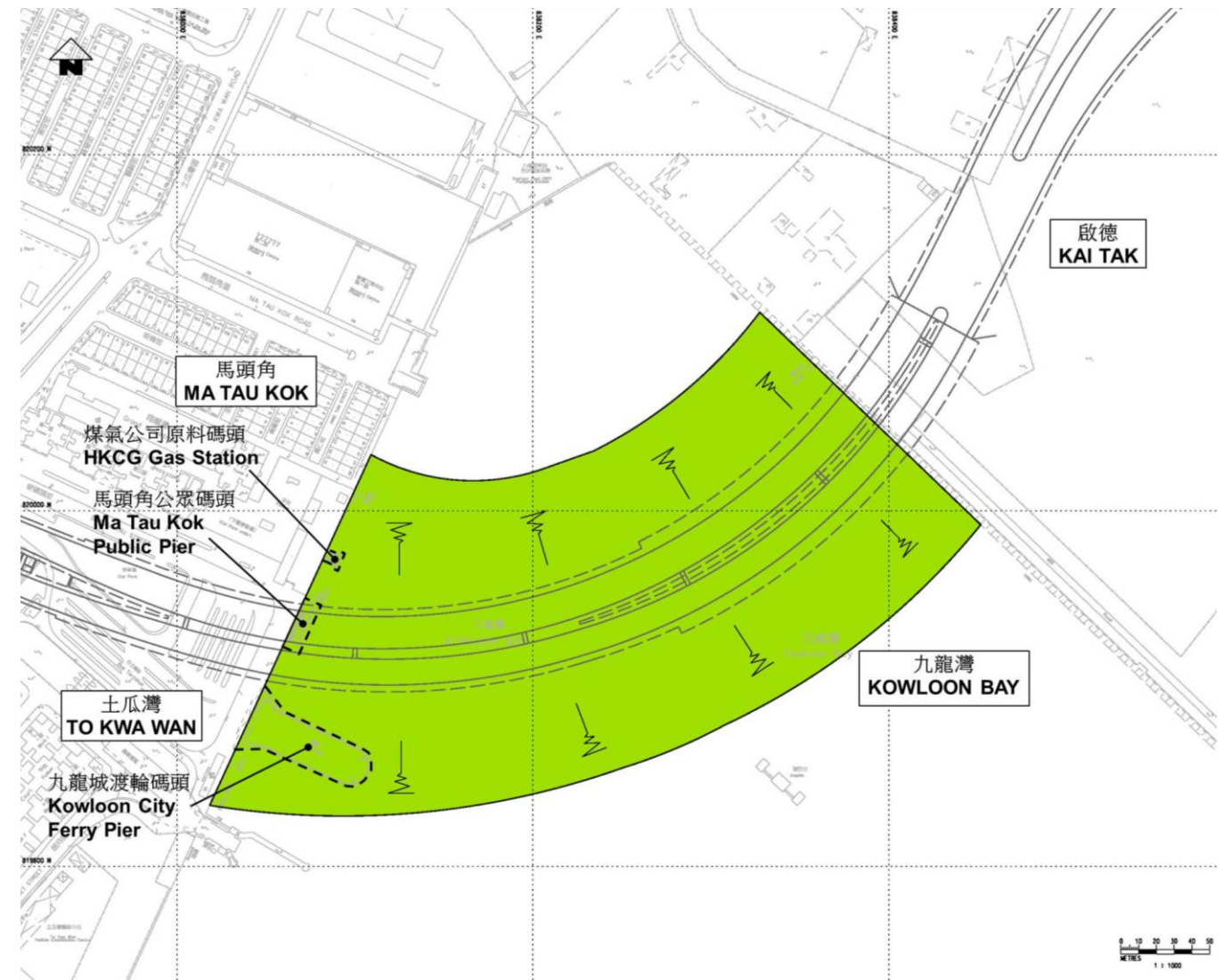


圖 3-2 - 工程影響的設施

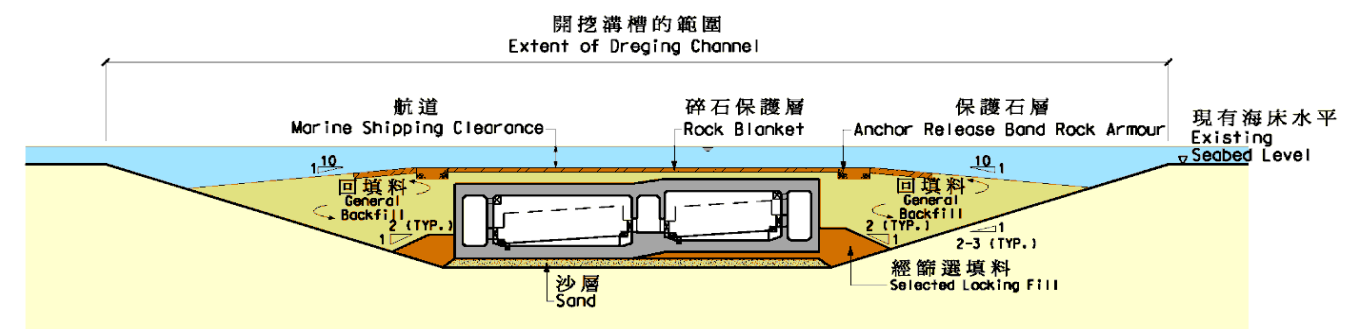


圖 3-3 - 沉管式隧道方案的典型剖面圖

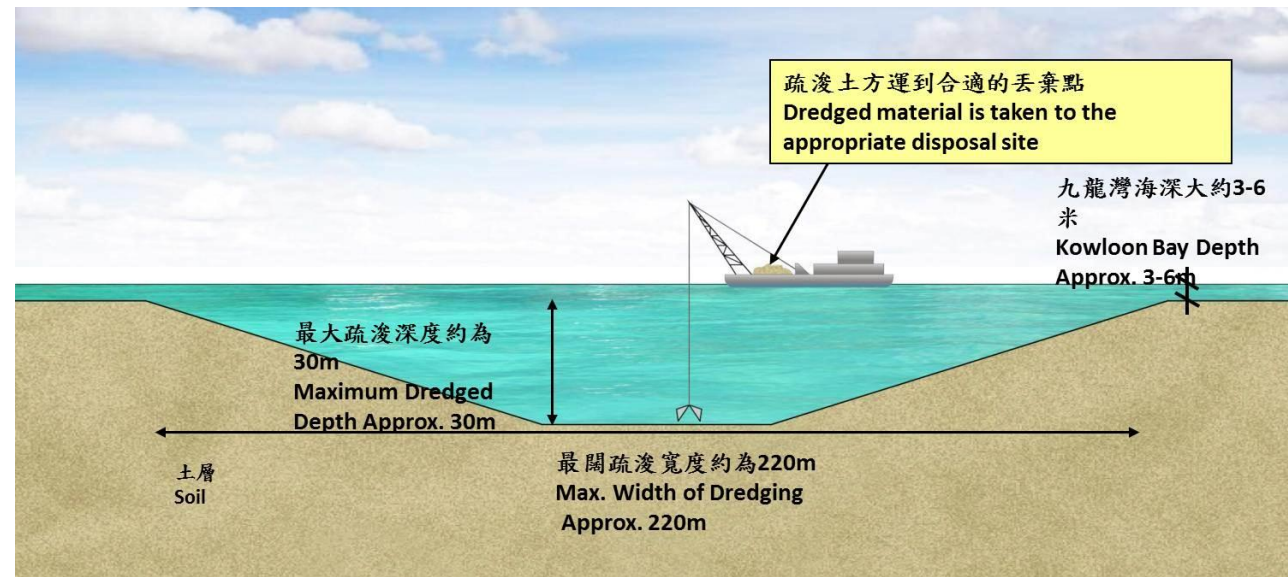


圖 3-4 (a) 第一階段 - 在海床進行大面積疏浚

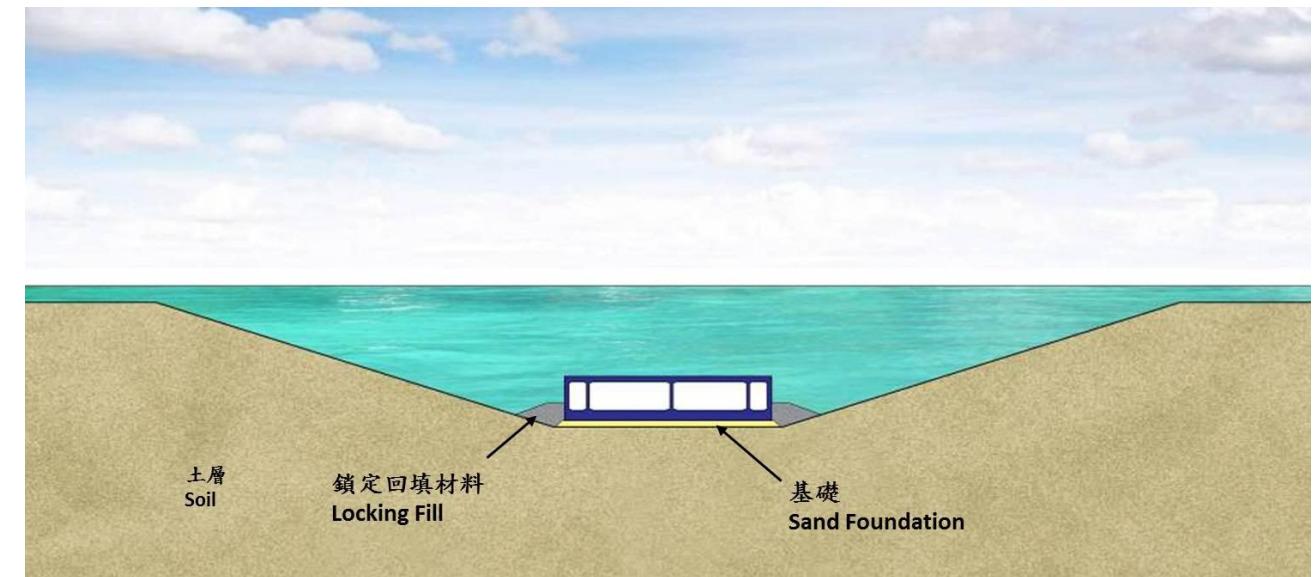


圖 3-4 (c) 第三階段 - 沉放及接駁預製組件和回填鎖定

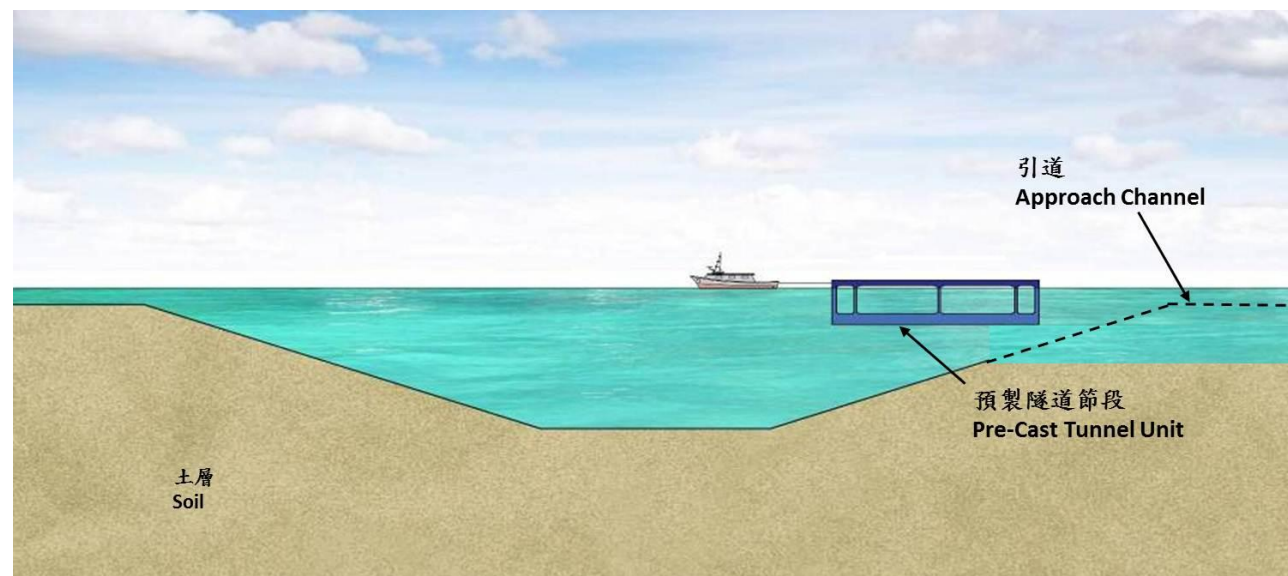


圖 3-4 (b) 第二階段 - 將預製隧道組件浮運到指定地點

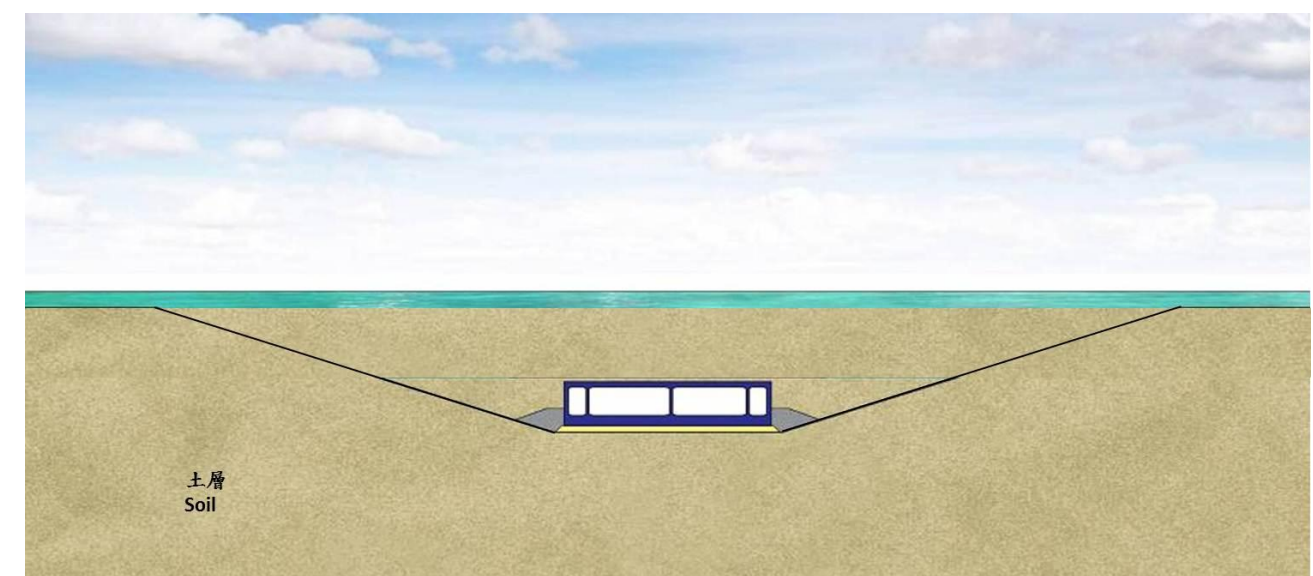


圖 3-4 (d) 第四階段 - 回填把海床恢復原狀

3.10 浮拖沉管式隧道預製件的例子如圖 3-5 所示。



圖 3-5 - 沉管式隧道的例子

3.11 挖掘沉管隧道之疏浚槽將需要移走和處理約 75 萬立方米的海泥。另外，由於九龍灣只有 6 米至 8 米深，一條 1,300 米長，150 米闊及 12 米深的引道需在海床挖掘運送隧道組件，從而造成總數約 180 萬立方米的海泥需疏浚和處理（見圖 3-6）。

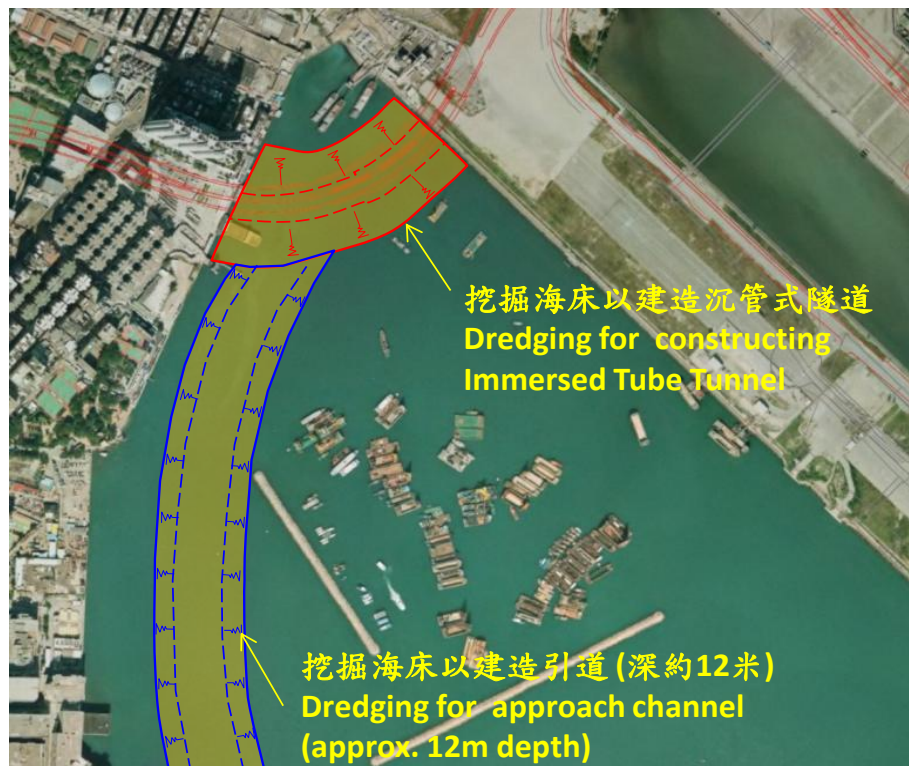


圖 3-6 - 因沉管隧道所需的疏浚槽及航道

3.12 現有的馬頭角及啟德海堤，及旁邊私人樓宇地基結構的完整性都會被坑道影響（見圖 3-7）。中華煤氣公司的碼頭及九龍城碼頭也會需要在建造期間暫時搬遷。

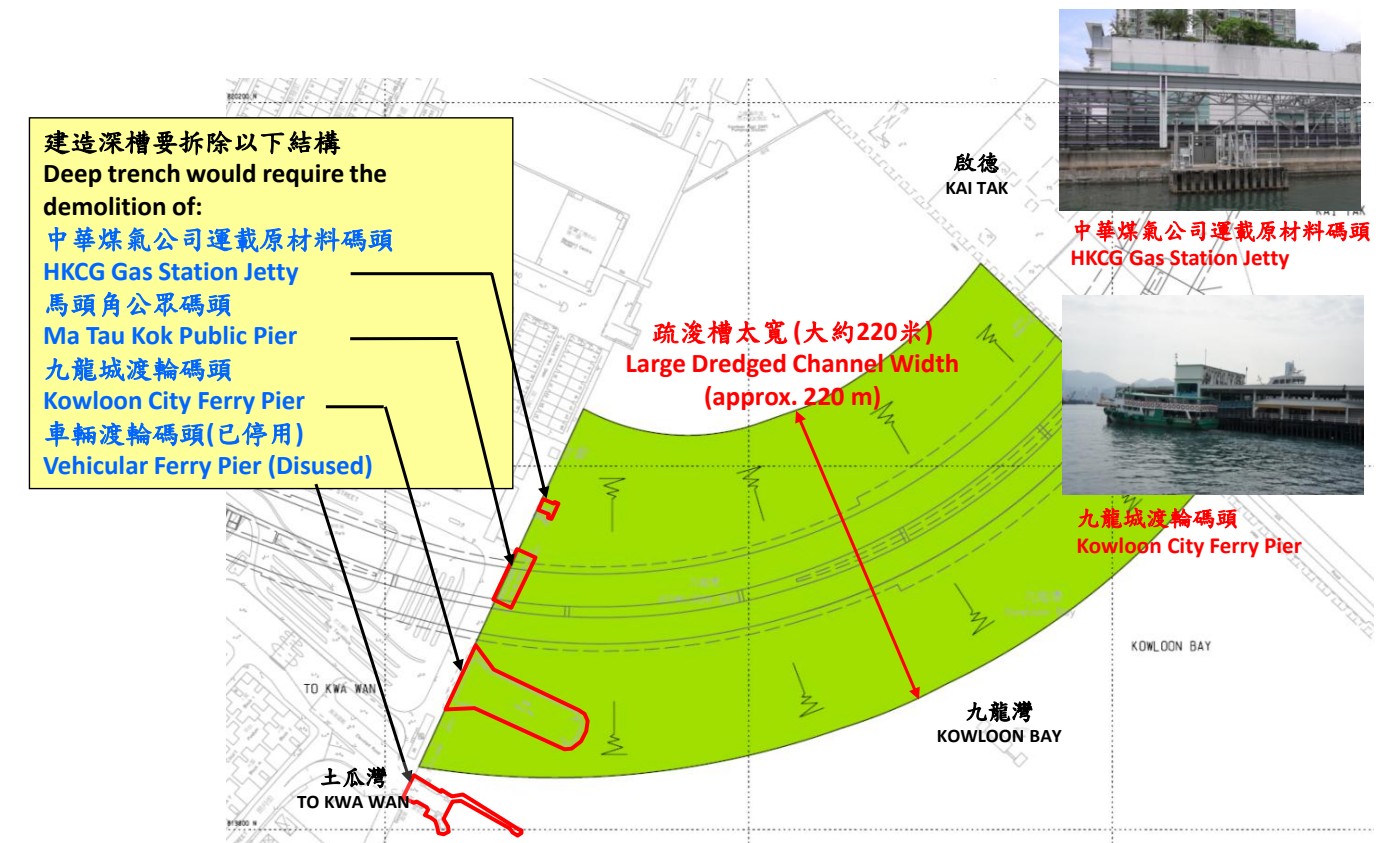


圖 3-7 - 疏浚槽會影響的結構

3.13 由於需要放置沉管節段和挖掘引道而要疏浚的大量海泥、及對海堤，私人樓宇，中華煤氣公司碼頭，及渡輪碼頭等產生影響，沉管式隧道不是一個合理的方案。

(二) 隧道鑽挖機

3.14 此方法涉及以隧道鑽挖機(“TBM”)鑽挖圓形隧道，穿越現有海床下的土壤。鑽挖後的隧道表面，會以預製混凝土隧道襯砌作保護。隧道鑽挖機的如圖 3-8 所示。



圖 3-8 - 隧道鑽挖機

3.15 在建造混凝土襯砌之前，隧道內需施用 300 千帕至 500 千帕的氣壓（或 3 至 5 倍的大氣壓）以支撐隧道挖掘面及防止隧道滲水。因此，需要有足夠的覆土以抵受隧道內壓力。覆土厚度將取決於地質條件，考慮到九龍灣海床土壤的低強度性（不排水抗剪強度低至 4 千帕），如圖 3-9 所示，所需覆土厚度約為隧道直徑的 1.5 倍。東行隧道（3 條行車線及 1 條爬坡線）的直徑約為 20.5 米。西行隧道（3 條行車線）的直徑約為 17 米。所需覆土厚度於是分別為 30.75 米及 25.5 米。

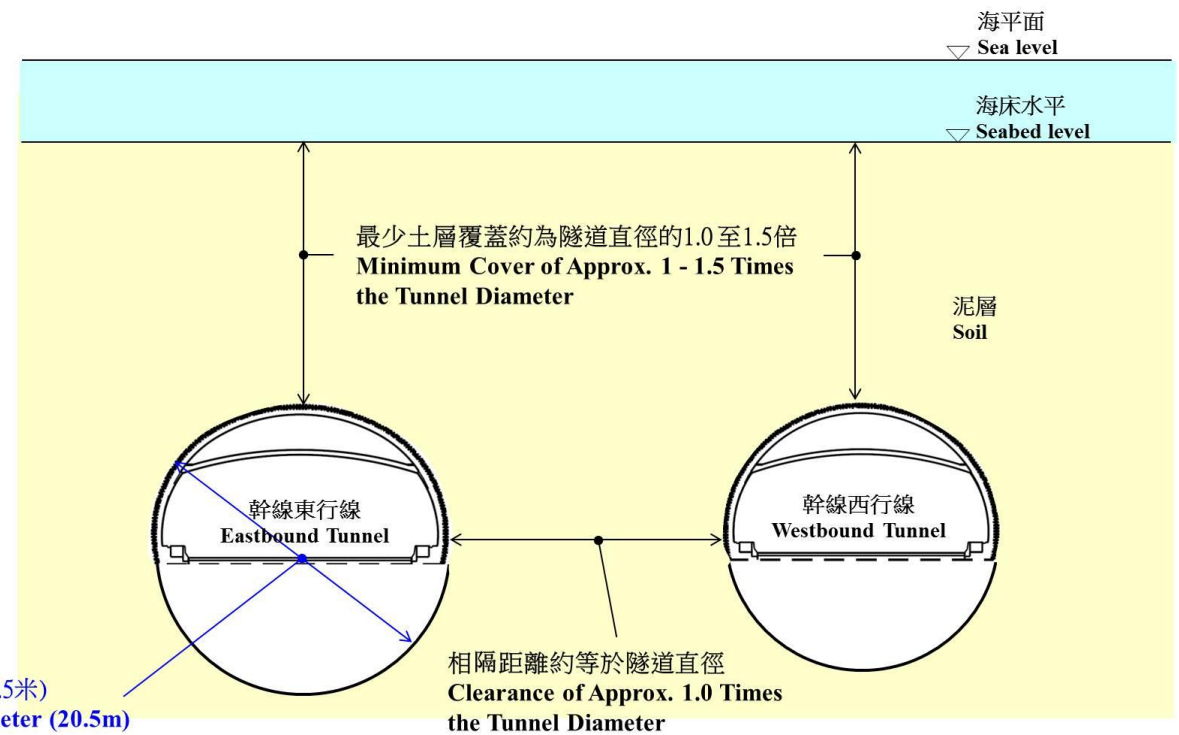


圖 3-9 - 隧道鑽挖機所需的覆土

3.16 因隧道需徐徐爬升至地面以連接九龍灣和啟德的道路網，如圖 3-10 所示，西端的最厚覆土僅有 17 米，東端更僅有 2 米，均少於 1.5 倍隧道直徑。

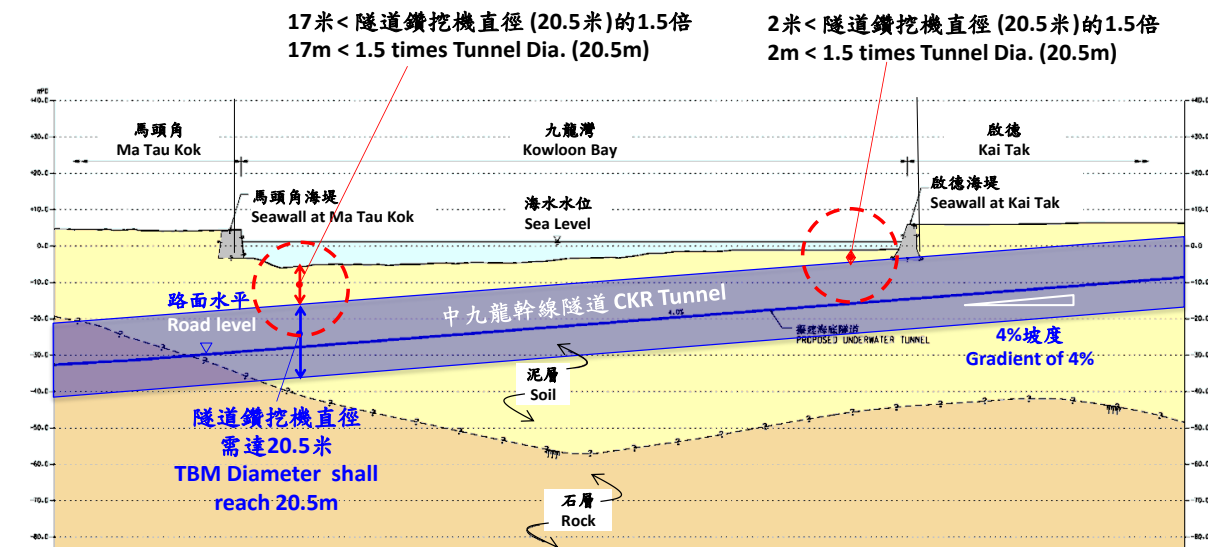


圖 3-10 - 九龍灣可用覆土

3.17 可用覆土不足以維持支持隧道挖掘面和防止隧道滲水所需的氣壓，因此會引致圖 3-11 所示的爆裂。

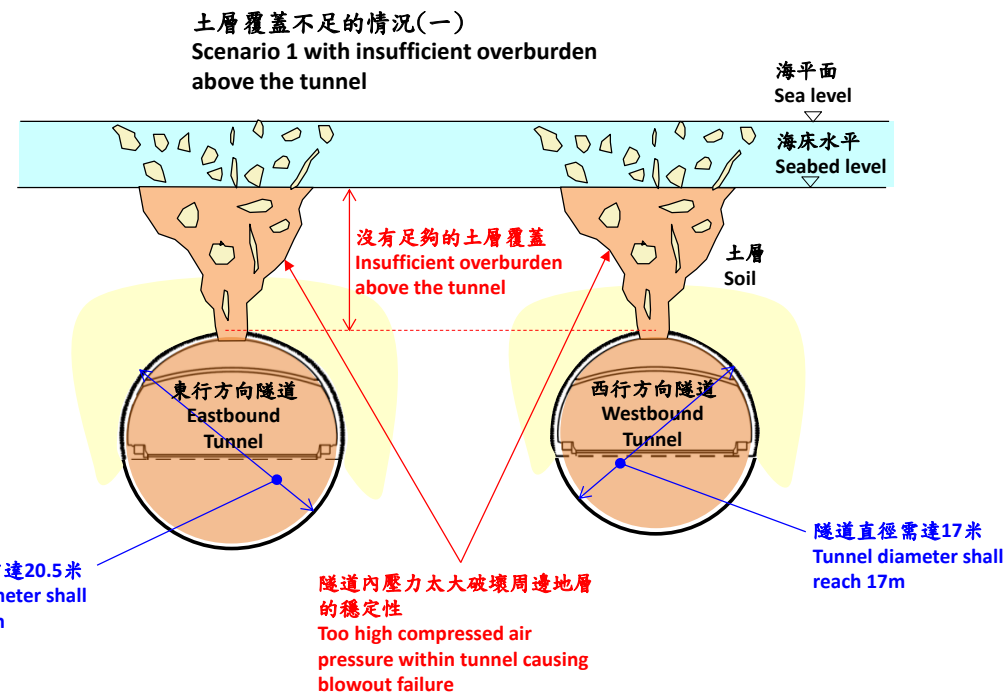


圖 3-11 - 爆裂情況

3.18 另一方面，如降低氣壓，氣壓將不足以支撐挖掘段及防止地下水滲入。因此，如圖 3-12 所示，隧道亦會因挖掘面坍塌和過量地下滲流而發生事故。

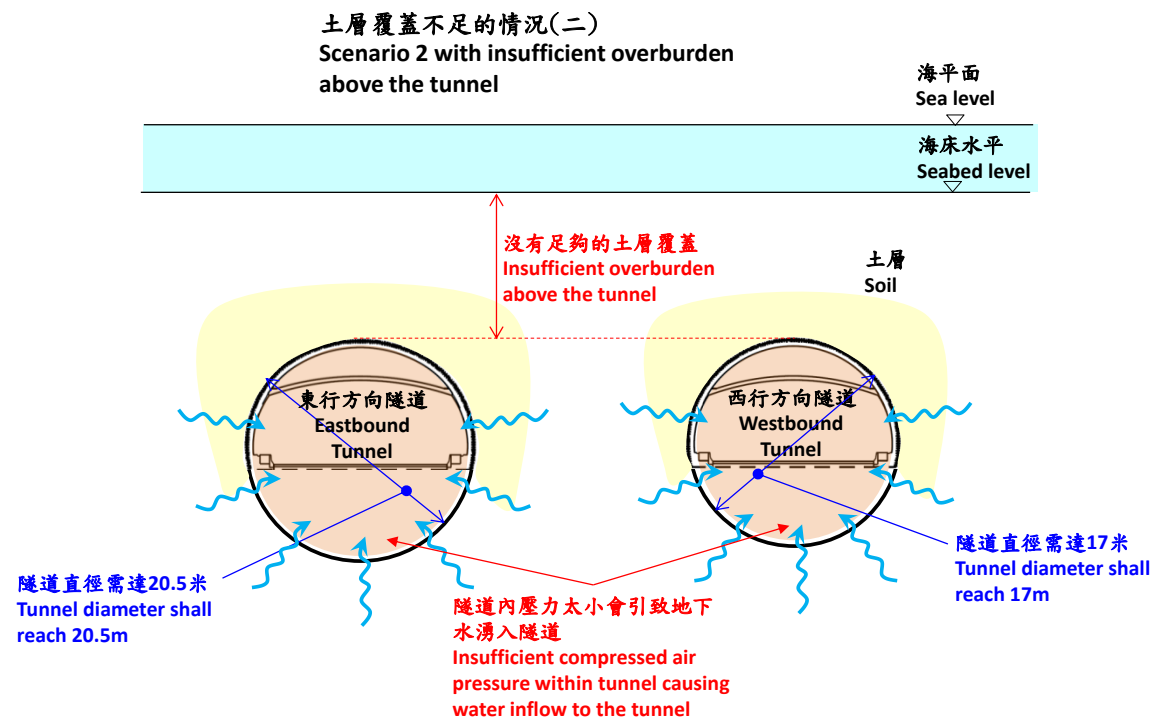


圖 3-12 - 滲流情況

3.19 綜合以上原因，採用隧道挖掘機建造海底隧道將對施工人員和公眾構成危險。隧道挖掘機因而不是合理的替代方案。

使用填海的建造方法

3.20 基於沉管隧道和隧道挖掘機都不是合理的替代方案，我們考慮是否可用圖 3-13 所示的臨時填海配合明挖回填方法建造海底隧道。

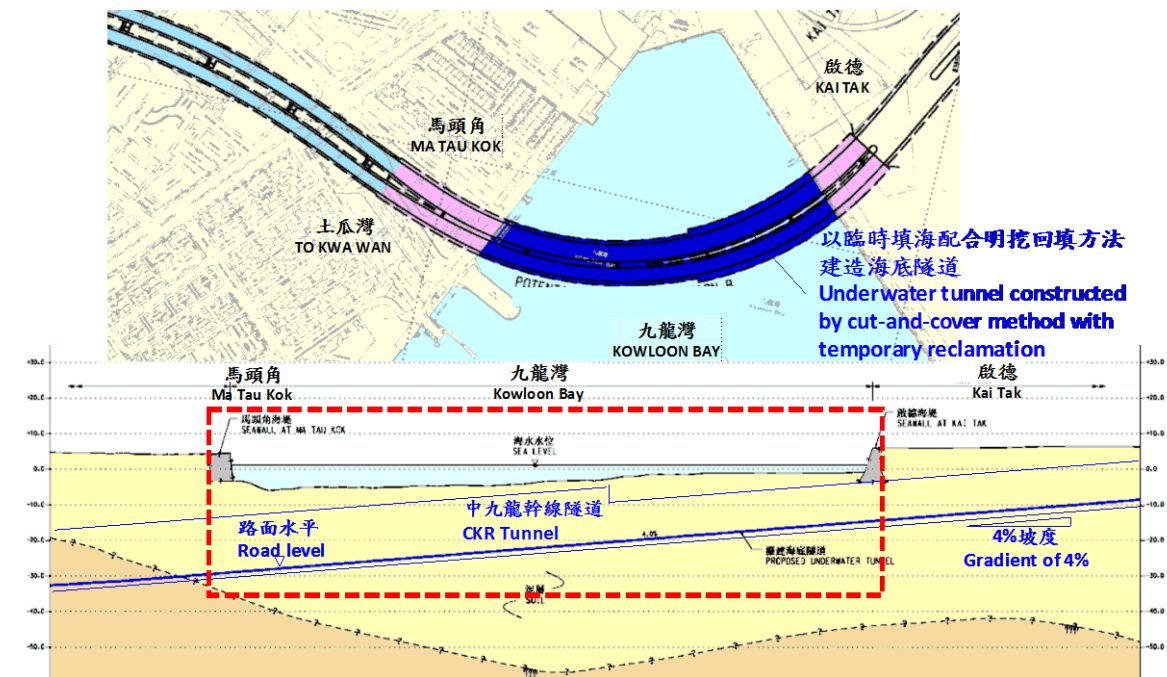


圖 3-13 - 臨時填海配合明挖回填法

3.21 在香港，多數的樓宇、地鐵及基建項目都使用明挖回填的方法建造隧道的。建造海底隧道或連接海底隧道的下沉式道路，使用臨時填海提供一個乾燥的工作平台及明挖回填隧道的建造方法亦已廣泛運用，並被認為是最實用的方法之一。圖 3-14 展示了在臨時填海範圍內使用明挖回填方法建造隧道的例子。



圖 3-14 - 臨時填海配合明挖回填法的例子

3.22 採用此方法，臨時海堤將使用大直徑管樁沿海底隧道走線建造。臨時海堤圍起的空間內將進行填海，形成工作平台。隔牆將於平台上建造以構成圍堰。圍堰內將展開挖掘工程以配合隧道結構的建造。臨時填海及海堤將在隧道完工後移除，海床也將恢復至原本水平。圖 3-15 展示了供參考的建造次序。

3.23 用臨時填海形成工作平台之後，將安裝臨時擋土結構來做大型挖掘。擋土結構類型取決於挖掘深度，水平面及地質條件。對於需要愈 20 米深度挖掘的海底隧道、高潮位超過水平標高正 2 米（海平面）及大約 9 米的海相沉積軟土，臨時擋土牆需能支撐來自附近土壤和海水的強大壓力。地下連續牆因其有較大的抗土壓和水壓的能力，被認為是擋土牆的首選結構類型。地下連續牆需穿透足夠的深度亦或深入石層（若石層不深）以提供抗傾覆穩定性和止水保護。

3.24 連續牆安裝後，為了提供乾燥工作平台，大型挖掘及側向支撐可進行。隧道建造完成後，現有的海床平面及移除剩下的臨時填海。最後，海床會被重建回原來的樣子。



圖 3-15 (a) - 明挖回填法配以臨時填海 - 第一步

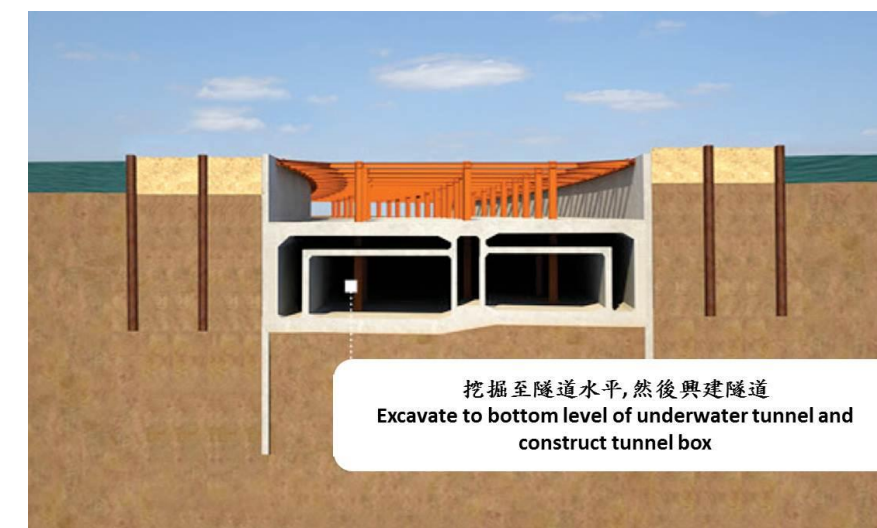


圖 3-15 (b) - 明挖回填法配以臨時填海 - 第二步

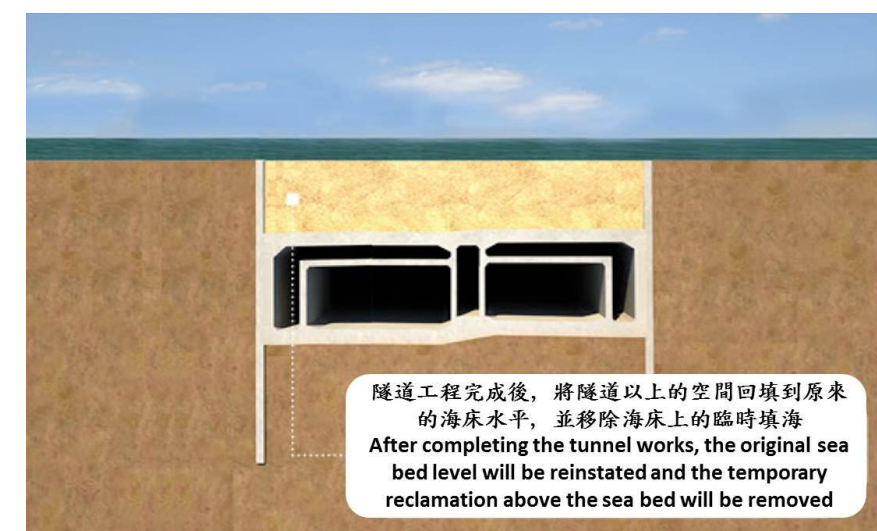


圖 3-15 (c) - 明挖回填法配以臨時填海 - 第三步

3.25 臨時填海將分兩階段進行，以維持進入中華煤氣公司石腦油碼頭的海上通道，及避免影響位於前啟德機場跑道與馬頭角之間、排放進九龍灣的現有箱形雨水渠。第一階段於九龍灣海面近啟德發展區處進行約 1.8 公頃的填海，以建造需時 26 個月、180 米長的隧道，海床於完工後將恢復至原有水平。第二階段於九龍城輪渡碼頭對開海域進行約 2.0 公頃的填海，以建造需時 26 個月、190 米長的隧道，海床亦會恢復至原有水平。九龍城輪渡碼頭之乘客服務於施工期間將保持正常。此兩階段臨時填海的安排詳見於圖 3-16 及圖 3-17。



圖 3-16 - 九龍灣兩階段臨時填海的安排

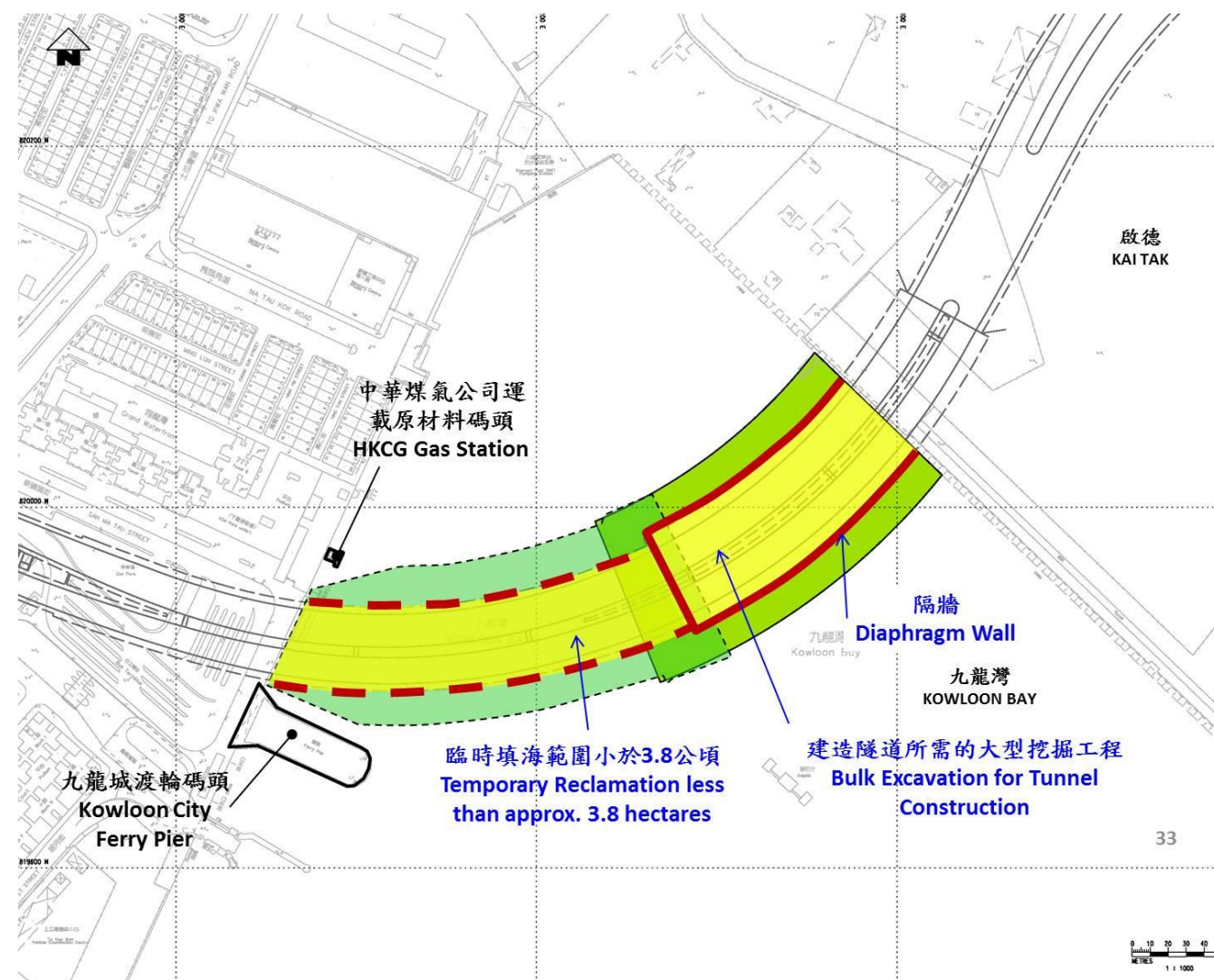


圖 3-17 - 九龍灣兩階段臨時填海的安排

3.26 綜合以上理由，使用明挖回填法配合臨時填海以建造海底隧道是可行的並是唯一安全可行的建造方法。

替代走線

3.27 我們在 2007 年至 2009 年進行勘測及初步設計研究亦曾探討有否其他替代走線，包括走線 A，C 至 E 及選取的走線（走線 B）。見於圖 3-18。

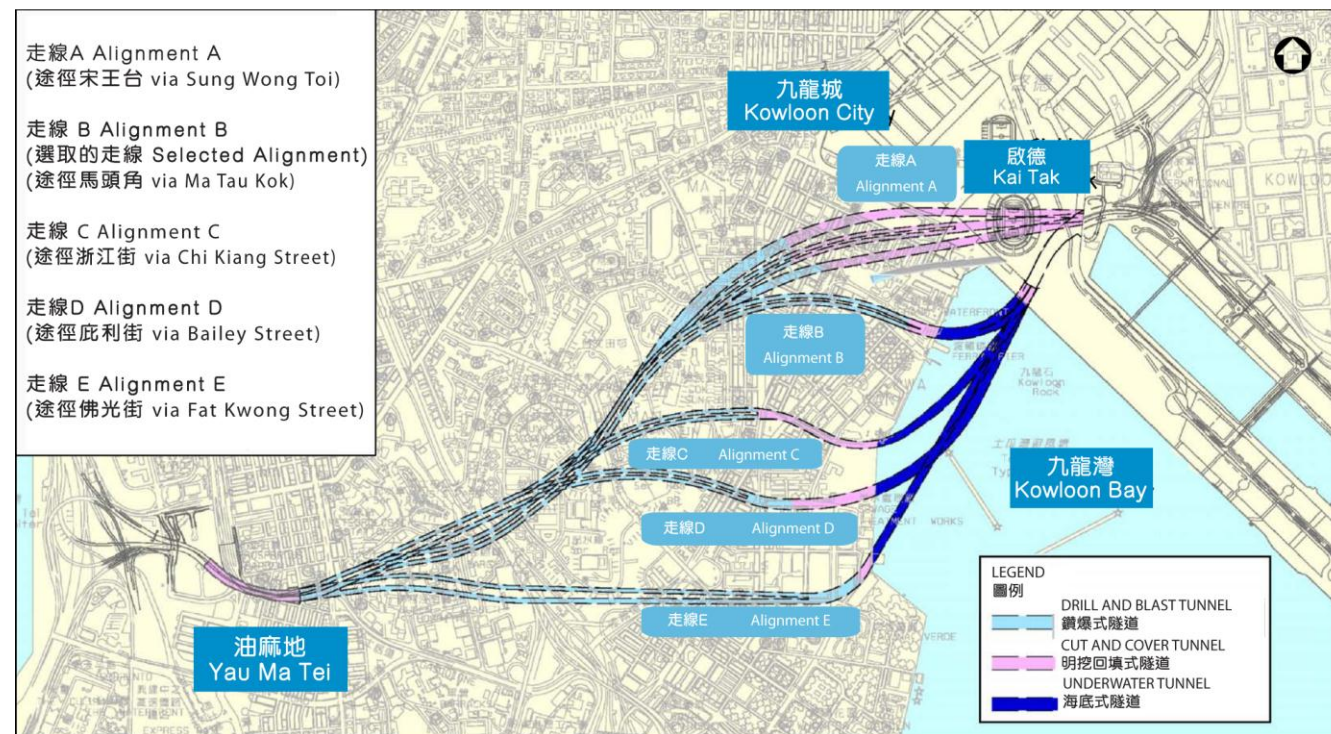


圖 3-18 - 勘测及初步設計階段的替代走線方案

3.28 走線 A 是全陸地走線，不涉及填海。唯走線 A 有一段約 600 米長的隧道會經土瓜灣木廠街一帶的數十幢私人樓宇。受影響的私人樓宇需要被收回及拆卸，以進行工程。走線 A 並不是合理的替代走線。

3.29 雖然走線 C 至 E 皆穿過現有道路及沿岸未發展地帶，再經海路連接啟德交匯處，但亦會涉及收回及拆卸私人樓宇，而它們所需的填海範圍比走線 B 較大，所以走線 C 至 E 亦非合理替代走線。唯有走線 B，即現時選取的走線，只需臨時使用現有的九龍城碼頭公共交通交匯處進行建造工程，但不涉及收回及拆卸私人樓宇，而且所需填海範圍亦最小。

4 最少範圍的臨時填海

引言

4.1 本章探討建造九龍灣海底隧道所需臨時填海範圍的因素並確立最小範圍臨時填海的方案。

填海的長度

4.2 如下圖 4-1 所示，海底隧道的軸線為一條半徑約 330 米的曲線。這是位於九龍城輪渡碼頭公共交通匯處與啟德河之間以最小半徑連接的最短反轉曲線。海底隧道的長度即臨時填海的長度亦為最小。



圖 4-1 - 填海的長度

填海的寬度

4.3 隧道寬度受約 330 米的曲線半徑控制。如圖 4-2 所示，這是符合交通規劃及設計手冊第二卷 3.3.5 節視距要求的最小半徑，以提供確保交通安全的合適視野。

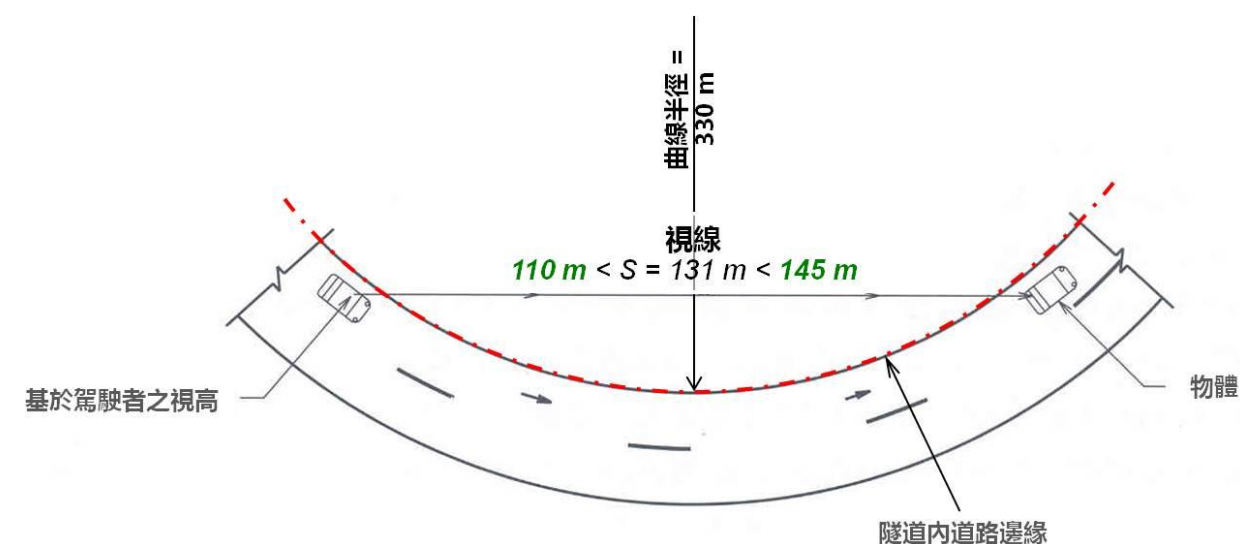


圖 4-2 - 視距要求

- 4.4 如下圖 4-3 所示，臨時填海的寬度由 87 米至 98 米不等並由以下構成：
- (a) 由連續牆構成的圍堰寬度由 47 米至 58 米不等；及
 - (b) 連續牆兩邊各 20 米寬的工作平台。

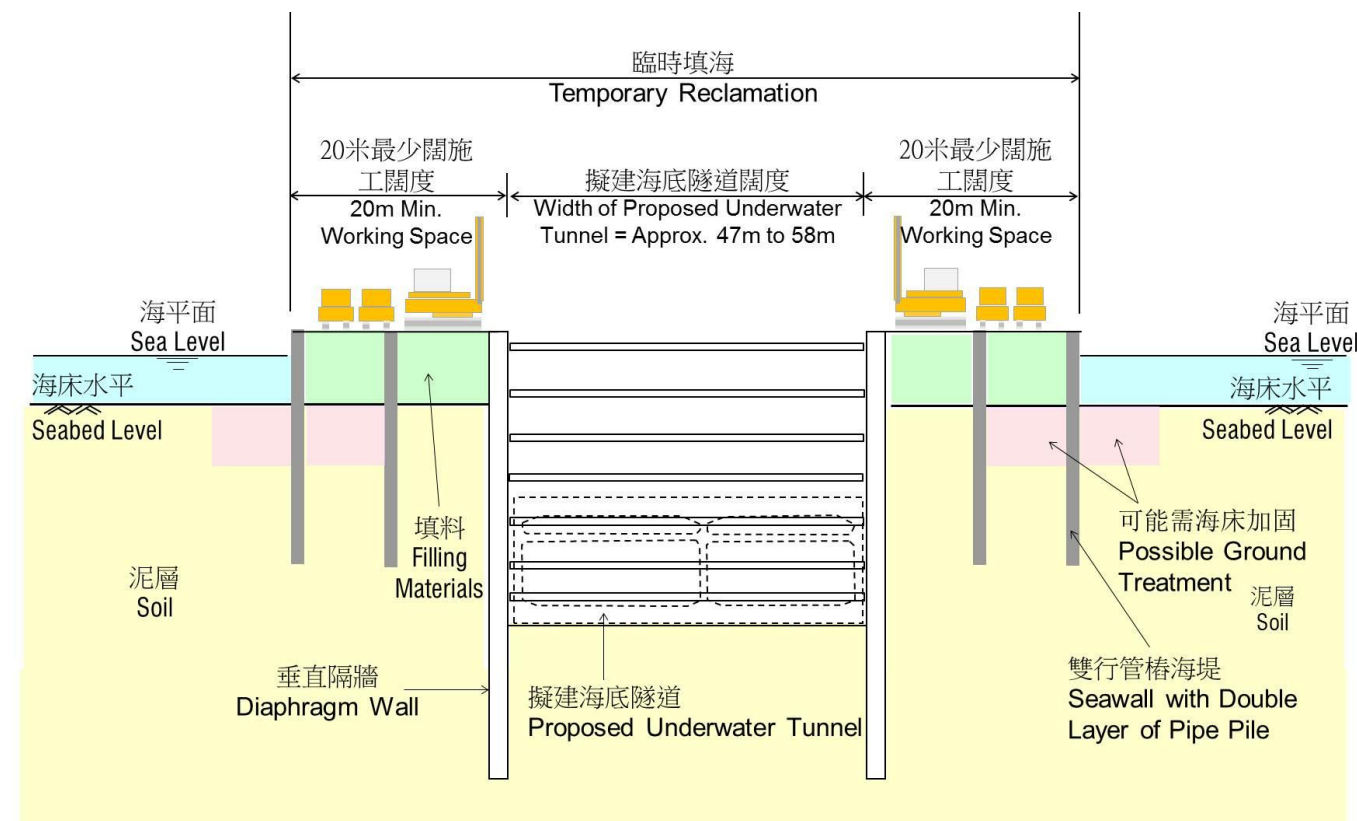


圖 4-3 - 臨時填海典型剖面

- 4.5 海底隧道的寬度及臨時填海的寬度都已為所需最小。

4.6 對於 4.4(a)段落，第三章 3.25 段已解釋，隧道將分兩階段建造：

- (a) 第一階段於九龍灣海面近啟德發展區處進行約 1.8 公頃的填海，以建造需時 26 個月、約 180 米長的隧道，海床於完工後將恢復至原有水平；及
- (b) 第二階段於九龍城輪渡碼頭對開海域進行約 2.0 公頃的填海，以建造需時 26 個月、約 190 米長的隧道，海床亦會恢復至原有水平。

4.7 對於第一階段需建的隧道，因要維持啟德發展區的海堤下的附近的最少水深，通風槽被安排在隧道兩邊。此段長約 58 米。對於第二階段需建的隧道，因有足夠淨高，通風槽被安排在隧道上方以減少填海的面積，此段因此長約 47 米。

4.8 對於 4.4(b)段，需以工作平台提供建造機械(起重機，自動傾斜卡車，挖土機等)所需的操作空間，利用駁船輸送材料的裝卸區域，施工車輛的活動。根據以相同方法建造海底隧道的中環-灣仔繞道項目的建造經驗，20 米的寬度剛好滿足這些用途。因此，擬臨時填海的寬度為最小的，圖 4-4 及 4-5 釋。

臨時填海的時間

4.9 臨時填海的總週期約為 52 個月。石樁、海堤、地下連續牆、開挖及隧道箱涵的建造各需 5 至 6 個月完成；填海、回填、移除填料和恢復原狀各需 1 至 2.5 個月完成。因一些工作可同步進行，每一階段需時約 26 個月完成。

最少填海要求的總結

4.10 已就海底隧道的建造、填海、海堤、受影響設施的重置等工程要求作詳細檢討，以準確確立所需臨時填海的最小範圍。

4.11 兩個階段的填海各持續時間不會超過 26 個月，計劃於 2015 年初至 2019 年中/底進行。

4.12 結論是，臨時填海面積已是最小的。臨時填海總面積不超過 3.8 公頃，任何時間的最大填海面積不超過 2.0 公頃。



圖 4-4 - 中環-灣仔繞道的臨時填海



圖 4-5 - 中環-灣仔繞道的臨時填海

5 公眾諮詢

前階段的公眾參與活動

5.1 路政署在 2007 年展開中九龍幹線的勘測及初步設計工作。由於工程項目會對交通、土地運用及環境有重大影響，我們採取全面的公眾參與策略，透過公眾論壇、焦點小組會議、外展活動、採訪、問卷調查、實地考察及規劃比賽，收集公眾對各主要範疇的意見。我們透過這些活動與各持份者包括居民、業主委員會、社區組織、商戶及區議會建立良好的溝通。我們亦就中九龍幹線項目諮詢油尖旺、九龍城和觀塘區議會，以及立法會交通事務委員會。

5.2 勘測研究的其中一個主要課題是選出一條合適的走線。我們檢討了過往在中九龍幹線研究過的 40 多個方案，並擬定出 14 個新的方案。我們比較各方案對社區設施重置、環境、土地及交通方面的影響，並參考公眾與過程中所收集到的意見，選取現時的走線。走線已獲立法會、油尖旺、九龍城和觀塘區議會的普遍支持。

5.3 透過公眾參與活動，我們了解到公眾普遍認為需要建造中九龍幹線，並希望中九龍幹線能有效接駁東九龍和西九龍的道路網，以紓緩交通擠塞。同時，應妥善保育油麻地警署、廟街夜市、天后廟及榕樹頭文化。

2009 年 7 月 18 日公眾論壇

5.4 通過長期與提案中的中九龍幹線東部的居民討論有關臨時性填海的事宜，最終對提案中的臨時填海的意見達成基本共識，不反對臨時填海，但是只有在沒有合理的備選方案的時候才可以選擇填海，並在期間需要考慮環境因素。

5.5 一些成員認為，其實市民的願望是可以有小規模永久九龍灣填海工程以提供新的社區設施，如公園、圖書館，休憩處及一條連續的散步徑，連接馬頭角啟德機場發展區。少數公眾更表達了在九龍灣地區進行小規模永久性填海可以為九龍灣提供減少臭味問題的機會。

5.6 設計小組已經收到了公眾提出關於小規模永久性填海的提案，但是根據對相關條例的理解，此類提案只有在通過高等法院根據保護海港條例第三條設定的三項測試後才可被考慮。由於中九龍幹線的提案中沒有涉及永久性填海，此提案應該被列為單獨考慮項目。

2009 年 6 月 20 日焦點小組會議

5.7 此項工程的歷史在專題小組會議中已經介紹給各個出席者。不同走線的供選方案以及此工程將會對公眾設施及環境的影響已在會議中討論過。

5.8 出席單位包括保護海港協會，海港之友，香港工程師學會，香港建築師學會，香港測量師學會以及九龍城區議會的成員。

5.9 會議提出馬頭圍公眾碼頭的拆除以及其它附屬的碼頭重置方案將會為加強海港前線形象及新置九龍灣公眾設施帶來機會。

公眾參與活動結論

5.10 就中九龍幹線優選走線及提案的工程，我們已經向公眾成員，油尖旺區議會，九龍城區議會，觀塘區議會以及立法會運輸委員會進行過諮詢活動。

5.11 總體情況上，大部分的公眾以及各團體代表都支持此建議的走線方案並對臨時填海提案沒有顯著反對。

現階段的公眾參與活動

5.12 中九龍幹線第二期公眾參與活動於 2012 年 12 月 5 日正式展開，就中九龍幹線的詳細設計及施工安排收集公眾意見。

5.13 在為期三個月的公眾參與活動期間，路政署舉行了不同類型的活動，如焦點小組會議、諮詢會和簡介會。包括與幹線沿途居民、專業學會、環保團體、玉器市場等的焦點小組會議和諮詢會。並向不同的區議會和海濱事務委員會簡介和諮詢他們的意見。

5.14 由於隧道需要於九龍灣段以臨時填海方式建造，項目統籌機構必須按《保護海港條例》的要求提出其有力和令人信服的資料，證明臨時填海有凌駕性的公眾需要。就此，路政署舉行了不同類型的公眾參與活動，包括一個海濱事務委員會諮詢會、九龍灣臨時填海專業論壇及九龍灣臨時填海專題討論的公眾論壇。

5.15 為方便公眾參與討論，第二期公眾參與摘要分別以中文及英文出版。此外，第 26 及 27 期中九龍幹線通訊則以中英文出版及廣泛派發，有助公眾了解中九龍幹線項目及項目進度。摘要及通訊詳細解說中九龍幹線的主要關注事項，包括中九龍幹線的效益、設計、綠化及景觀、文物保育、重置公共設施、環境影響、施工安排以及九龍灣段臨時填海的需要。公眾參與活動亦包括巡迴展覽，於油麻地、觀塘、九龍城及何文田地區展出隧道模型及虛擬場景模型。

5.16 為推廣第二期公眾參與活動，路政署向社區不同的持份者，包括沿線及就近幹線的居民、學校、社區組織、商業大廈、商戶、區議會、地區組織、專業學會及環保團體，發出約 50,000 封邀請信，鼓勵各界人士踴躍參與第二期公眾參與活動。路政署亦於兩份中文報刊（東方日報和頭條日報）及一份英文報刊（The Standard）刊登廣告，於 2013 年 1 月 4 日，11 日，18 日，25 日及 2 月 1 日刊出，大力宣傳及鼓勵公眾參加公眾論壇，希望不同背景的持份者就中九龍幹線的詳細設計提供意見及作出討論。

5.17 表 5-1 展示所有第二期的公眾參與活動。

表 5-1 – 第二期的公眾參與活動

日期	公眾參與活動
2012 年 12 月 11 日	諮詢會 (駿發花園居民)
2012 年 12 月 12 日	焦點小組會議 (京士柏)
2012 年 12 月 13 日	諮詢會 (油尖旺區議會)
2012 年 12 月 13 日	焦點小組會議 (馬坑涌)
2012 年 12 月 14 日	焦點小組會議 (馬頭角)
2012 年 12 月 15 日	焦點小組會議 (佐敦西)
2012 年 12 月 15 日	焦點小組會議 (油麻地)
2012 年 12 月 16 日	諮詢會 (翔龍灣居民)
2012 年 12 月 17 日	焦點小組會議 (樂文)
2012 年 12 月 18 日	焦點小組會議 (海心)
2012 年 12 月 19 日	焦點小組會議 (常樂)
2012 年 12 月 19 日	焦點小組會議 (愛俊)
2012 年 12 月 20 日	焦點小組會議 (愛民)
2013 年 1 月 2 日	焦點小組會議 (玉器市場商販)
2013 年 1 月 4 日	焦點小組會議 (環保團體)
2013 年 1 月 7 日	簡介會 (海濱事務委員會)
2013 年 1 月 8 日	簡介會 (觀塘區議會)
2013 年 1 月 8 日	簡介會 (黃大仙區議會)
2013 年 1 月 10 日	九龍灣臨時填海專業論壇
2013 年 1 月 12 日	公眾論壇 (油尖旺區議會)
2013 年 1 月 17 日	簡介會 (油尖旺區議會交通及運輸委員會)
2013 年 1 月 17 日	簡介會 (九龍城區議會)
2013 年 1 月 18 日	諮詢會 (偉恆昌新邨)
2013 年 1 月 19 日	公眾論壇 (九龍城區議會)
2013 年 1 月 22 日	諮詢會 (香港建築師學會)
2013 年 1 月 26 日	諮詢會 (京士柏居民)
2013 年 2 月 1 日	簡介會 (油尖旺區議會社區建設委員會)
2013 年 2 月 2 日	九龍灣臨時填海專題討論
2013 年 2 月 4 日	諮詢會 (香港規劃師學會、香港城市設計學會及香港園境師學會)

現時有關中九龍幹線的公眾意見

5.18 以下部份概述了公眾及不同持份者就有關九龍灣臨時填海的公眾參與活動中發表的重點意見。

5.19 公眾和當區居民普遍認為中九龍幹線能有效接駁東九龍及西九龍的道路網絡，以紓緩交通擠塞。有個別環保團體及公眾卻指出，興建更多道路設施並不能有效地改善交通擠塞問題，他們認為加強交通需求管理，才是解決交通擠塞的方法。然而這意見亦經獨立運輸專家檢閱，他指出香港私家車擁有率比較低，而且道路使用者主要為商用車輛，所以有需要建造中九龍幹線。

5.20 大多數參加者，包括當區居民和公眾，就中九龍幹線九龍灣臨時填海建議沒有強烈意見。一些居民更建議把臨時填海轉為永久填海，從而有助解決九龍灣海岸的臭味問題及改善與啟德地區的行人接駁。

諮詢區議會

5.21 油尖旺、九龍城、黃大仙及觀塘區議會均認同中九龍幹線能有效接駁東九龍及西九龍的道路網，以紓緩交通擠塞。他們促請政府盡快落實中九龍幹線的工程。有不少區議員表示，中九龍幹線通車後會有助減少於油麻地、何文田及九龍城的路面行車量，從而有效改善這些地區的交通情況及環境。

5.22 有些區議員表達支持臨時填海的建議及認同顧問公司就填海徵詢專業人士意見的做法。有九龍城區區議員進一步建議，研究合理的方法，有助控制九龍灣海岸的臭味問題。

諮詢海濱事務委員會

5.23 路政署和顧問公司向海濱事務委員會匯報其有力和令人信服的資料以證明九龍灣段的臨時填海有凌駕性的公眾需要，以及解釋中九龍幹線的詳細設計及施工安排。

5.24 海濱事務委員會大致認同項目的策略性需要及其走線，並且認可因建造中九龍幹線而需進行臨時填海工程的需要。

九龍灣臨時填海專業論壇

5.25 由於項目工程需要在九龍灣段以臨時填海方式建造，項目統籌機構須要按《保護海港條例》的要求，證明臨時填海有凌駕性的公眾需要。就此，顧問公司於專業論壇向有關的專業及學界人士，匯報其有力和令人信服的資料以支持臨時填海有凌駕性的公眾需要。匯報完結後，路政署邀請了兩名獨立專家檢閱顧問公司所提供的資料。

5.26 專業及學界人士對顧問公司及兩名獨立專家所提供就中九龍幹線的凌駕性公眾需要的理據，並沒有異議。

5.27 專業及學界人士普遍認為沒有其他合理的建造方式及其他幹線走線能夠取代填海工程，他們認為隧道鑽挖機及沉管式隧道建造方法均不是替代建造中九龍幹線九龍灣段海底隧道的合理建造方案。

5.28 專業及學界人士普遍認為臨時填海工程的建議比其他建造方式對海床造成較少損害及滋擾。

九龍灣臨時填海專題討論

5.29 按《保護海港條例》的要求，證明臨時填海有凌駕性的公眾需要，在九龍灣臨時填海專題討論的公眾論壇上，就著(1)臨時填海有沒有凌駕性的公眾需要、(2) 沒有其他合理替代填海的方案和 (3) 所需的填海範圍是最小。顧問公司就匯報其有力和令人信服的資料以支持臨時填海有凌駕性的公眾需要。匯報完結後，路政署邀請了兩名獨立專家審閱顧問公司所提供的資料。

5.30 公眾人士同意解決交通擠塞的迫切需要而建造中九龍幹線 (1) 有凌駕性的公眾需要; 公眾人士並同意 (2) 沒有其他安全可靠的合理替代填海的方案和 (3) 現時建議所需的填海範圍亦是最小的。

6 結論

有關臨時填海的凌駕性公眾需要

6.1 大多數參加者，包括油尖旺、九龍城及觀塘區議會、幹線沿途居民和公眾，認同中九龍幹線能有效接駁東九龍及西九龍的道路網絡，以紓緩交通擠塞。他們促請政府盡快落實中九龍幹線的工程。海濱事務委員會亦表示認同興建中九龍幹線有策略性需要。不同的專業學會亦表示不會質疑興建中九龍幹線的需要。

6.2 多個區議員表示，中九龍幹線通車後會有助減少於油麻地、何文田及九龍城的道路行車量，從而有效改善當區的交通情況及環境。

6.3 在九龍灣臨時填海專題討論的公眾論壇上，公眾人士同意解決交通擠塞的迫切需要而建造中九龍幹線有凌駕性的公眾需要。

6.4 因此，公眾認為以臨時填海方式建造中九龍幹線是有凌駕性的公眾需要。

沒有合理而不涉及填海工程的建造方式

6.5 中九龍幹線臨時填海的需要性是由顧問公司及二名專業人士提出，而海濱事務委員會表示不會質疑臨時填海的需要性，包括沒有其他走線及合理的建造方式代替填海工程的理由。

6.6 專業及學界人士於專業論壇都認同沒有其他合理的建造方式及其他幹線走線能夠取代填海工程，他們認為隧道鑽挖機及沉管式隧道建造方法均不是合理的替代建造中九龍幹線九龍灣段的海底隧道的建造方案。

6.7 在九龍灣臨時填海專題討論的公眾論壇上，公眾人士同意沒有其他安全可靠的合理取代填海的方案。

6.8 雖然有個別書面意見建議把中九龍幹線的走線向北移來避免填海工程，但公眾大致認為沒有其他合理的建造方式取代填海工程。

最小的填海範圍

6.9 中九龍幹線臨時填海的需要性是由顧問公司及兩位專業人士提出，而海濱事務委員會表示不會質疑臨時填海的需要性，包括臨時填海會對海岸造成的少量損害。

6.10 在專業論壇期間，專業及學界人士都認為臨時填海會對海岸造成少量損害。

6.11 在九龍灣臨時填海專題討論的公眾論壇上，公眾人士同意現時建議所需的填海範圍是最小的。

6.12 因此，路政署就最小填海範圍已與公眾達成共識。

第二期公眾參與活動

6.13 我們在 2012 年 12 月初展開中九龍幹線的第二期公眾參與活動，以收集公眾對中九龍幹線的詳細設計及施工安排的意見。到目前，我們已按計劃舉行過了一連串的公眾參與活動，包括為沿線居民、環保團體、專業學會及其他持分者舉行十多場的焦點小組會議，以及於油麻地、何文田、土瓜灣和觀塘不同地點進行五次巡迴展覽。

6.14 我們亦已諮詢油尖旺、九龍城、黃大仙及觀塘的區議會，和海濱事務委員會。此外，我們亦在 2013 年 1 月 12 日及 1 月 19 日分別在油尖旺區及九龍城區舉行兩場公眾論壇，廣泛探討中九龍幹線項目。我們藉此機會感謝各界人士積極參與並提供寶貴意見。

獨立專家審查

6.15 因應保護海港條例及為進行與此報告相關的公眾參與活動，我們聘請了兩位獨立專家審評員，他們需要：

- 提供嚴謹的審查報告，考慮中九龍幹線在九龍灣填海的必要性。
- 確認提議中臨時填海的論據是有力的和令人信服的。
- 確定項目通過“凌駕性公眾需要測試”的要求。
- 確認並無其他切實可行性選擇替代的填海工程。
- 確認擬填海的範圍是最小的。

6.16 獨立專家的審查請參閱附錄一和附錄二。

符合保護海港條例

6.17 總括而言，保護海港條例中關於禁止填海的三項測試準則均已通過：

- 為配合中九龍幹線的建造及符合公眾對此道路網絡的凌駕性需要，在九龍灣填海有當前迫切的需要。所有填海都是臨時的且在項目完成後會被移除，海床也將恢復至原有水平。
- 沒有除臨時填海以外的合理性替代方案可用於建造中九龍幹線九龍灣段的海底隧道。
- 填海範圍為最小所需範圍。

附錄一

林興強教授 - 關於九龍灣臨時
填海工程具有力和令人信服的
材料報告之獨立專家審查



PolyU Technology & Consultancy Company Ltd
理大科技及顧問有限公司

中九龍幹線必要性的交通論證 —獨立專家評估 (編號：Hy(S)Q/062/2012)

項目編號：P12-0276

William H.K. LAM 林興強
18 February 2013

1. 引言

2012年12月28日，香港特別行政區路政署(HyD)委任理大科技及顧問有限公司(PTeC)林興強教授(協議編號：Hy(S)Q/062/2012)從交通合理性方面對中九龍幹線(CKR)的必要性提供獨立“專家”評估服務。

而且，根據最低限度的臨時填海範圍與首選最短路線長度及相關公路設計標準的關係，“專家”對中九龍幹線最低限度的臨時填海範圍提供了相關論證。

2. 項目描述

中九龍幹線採用雙程三線分隔車道的設計方案(包括3.9公里長的隧道)，穿過中九龍分別與西邊的西九龍及東邊的啓德發展區相連接。在西九龍，中九龍幹線的西邊連接油麻地交匯處，穿過交匯處直達西區海底隧道，尖沙咀，西九龍填海區，西九龍公路，8號幹線及3號幹線。在啓德發展區東邊，中九龍幹線分別連接九龍灣，東九龍，觀塘繞道，將軍澳隧道，T2路段，將軍澳-藍田隧道。中九龍幹線與T2路段，將軍澳-藍田隧道共同組成連接西九龍和將軍澳新市鎮的策略公路幹線，簡稱6號幹線。

按照以前設定的目標，中九龍幹線應在2016年建造完成。現時計劃在2015年初開始建造，到2020年尾建造完成及通車。

3. 交通評估

下面的評估是基於最新的中九龍幹線交通影響評估草擬報告-設計與建造(編號：REP-081-00)，中九龍幹線補充交通研究最終報告(編號：HMW 1/2010 (TT))，修訂過的最新經濟評估草擬報告(編號：REP-077-01)，以及由路政署“顧問”，Arup-Mott MacDonald，合資公司提供的補充材料。

3.1 現有的道路網

現時，由主要幹道構成的東-西走廊(“走廊”)為中九龍地區提供交通服務，像龍翔道，界限街，太子道西，亞皆老街和天橋，漆咸道北，東九龍走廊，加士居道天橋。



該“走廊”主要作為中九龍地區東西方向的連接路線，也為九龍半島東西方向的長途交通提供服務。

作為中九龍地區的主要幹線，該“走廊”同時為不同地區提供南北方向的連接，也為到達鄰近地區提供出行之路。然而，這些支路，橋下通道，天橋與“走廊”連接構成的多個交匯處會產生大量互相抵觸的車流。因此，該“走廊”處於過度飽和狀態，並且，從當地到其鄰近地區車輛過度使用該“走廊”，導致它沒有空間為東-西方向長途交通提供服務。現時，沿“走廊”支路或其主要路段的樽頸處，交通排隊通常導致其他車輛的堵塞，以及交通狀況的逐漸惡化。

發生在該“走廊”附近的輕微交通事故往往導致嚴重的道路擠塞和延誤。在某些重大情況下，整個九龍地區的交通嚴重擠塞，並且導致走廊通道完全癱瘓（例如 2005 年 5 月 9 日發生在太子道東的嚴重塌棚架事故）。這些都清楚地證明，中九龍道路網的穩定性和可靠性已經達到令人不可接受的程度。

3.2 現有交通狀況

現時“走廊”已經處於超出設計通行能力的運行狀態。在該“走廊”主要道路交叉口常常出現交通排隊情況。最大排隊長達200米，甚至更長。這些擠塞的路口主要包括：

- 麗翔道 海泓道東行/麗翔道交叉口;
- 馬頭涌道南行/宋皇台道交叉口;
- 柯士甸道 柯士甸道西西行/柯士甸道/廣東道交叉口;
- 佐敦道東行/渡船街/廣東道交叉口;
- 佐敦道東行/彌敦道交叉口;
- 界限街東行/窩打老道交叉口;
- 亞皆老街東行/窩打老道/公主道交叉口;
- 亞皆老街東行/染布房街交叉口;
- 旺角道 洗衣街東行/旺角道交叉口;
- 漆咸道北南行/蕪湖街交叉口;
- 啓祥道西行/宏照道交叉口;
- 臨豐街 常怡道東行(MegaBox對開)/宏照道交叉口;
- 偉業街東行/偉發街交叉口;
- 匯翔街 廣東道東行/匯翔街交叉口。



以上路口的容量評估證實，目前，一些主要道路交叉口處於接近或超過容量的運行狀態。中九龍地區大多數路口（例如，亞皆老街/洗衣街，亞皆老街/彌敦道，柯士甸道/漆咸道南/暢運道）在高峰時段普遍處於臨界飽和狀態，因此只有很少的剩餘容量 (R.C.) 為東-西方向長途車流提供服務。

總言之，現時，日常的交通排隊佔據了該“走廊”上的道路空間，給中九龍地區東-西方向交通帶來不可接受的延誤。

3.3 交通預測

預計中九龍幹線在 2020 年末或 2021 年初開始投入使用，通過比較基本（無中九龍幹線）和設計（有中九龍幹線）兩種方案下的交通預測開展最新交通影響評估。基於標準的交通預測方法，“顧問”為中九龍地區測試了 5 組方案來預測未來幾年高峰時段的交通狀況。這些測試方案如下所示，總的結果列於表 1 中：

1. 2016 基本方案：2016 – 中九龍幹線建造階段方案(即無中九龍幹線和6號幹線);
2. 2021 基本方案：S2021/A – 無中九龍幹線和6號幹線(Route 6)方案;
3. 2021 設計方案：2021/C – 有中九龍幹線(CKR)和將軍澳-藍田隧道(TKO-LTT)方案，而T2路段還不能使用，只是作為保守的設計方案來測試;
4. 2026 基本方案：S2026/A – 無中九龍幹線和6號幹線方案;
5. 2026 設計方案：S2026/G – 有中九龍幹線和6號幹線方案。

表 1：5 種測試方案的建模假設和結果

方案	中九龍幹線	6 號幹線	T2 路段	將軍澳-藍田隧道	流量建模結果	
					走廊主要道路的 V/C 比率	中九龍主要道路交叉口的 RC
方案 S2016	×	×	×	×	許多路段的 v/c 比率大於 1.0.	一些主要交叉口的 RCs 為負值.
方案 S2021/A	×	×	×	×	多數路段大於 1.0. 有些路段高達 1.30.	18 個主要交叉口的 RCs 為負值 (6 個交叉口 RC < -15%).
方案 S2021/C	✓	✓	×	✓	大多數路段截面的 v/c 比率小於 1.0. 少量路段為 1.1.	許多主要交叉口的 RCs 為正值(3 個交叉口 RC < -15%).
方案 S2026/A	×	×	×	×	多數路段的 v/c 比率大於 1. 一些路段為 1.40.	18 個主要交叉口的 RCs 為負值(小於 S2021A 對應的 RC 值).
方案 S2026G	✓	✓	✓	✓	大多數西行路段的 v/c 比率小於 1. 少數路段為 1.20	多數主要交叉口的 RCs 為正值(3 個交叉口 RC < -15%).

注釋：V/C 比率=路段流量和路段通行能力的比率; RC =信號交叉口的剩餘容量



3.4 結果總結

根據預測，未來經濟增長將會導致東西走廊上的交通需求持續增加。因此，東西走廊上的大多數主要道路在一般的早晚高峰時間將會超出負荷 10%到 30%。

關於設計方案 (有中九龍幹線)，與對應基本方案相比較，受影響地區內的交通擁擠狀況將會普遍得到改善。在 2021 年和 2026 年，和無中九龍幹線相比較，關鍵交叉口處的剩餘容量一般會增加。

鑒於主要道路和擁擠交叉口處交通狀況的明顯改善，這充分證明導致交叉口交通問題的主要原因是因為鄰近地區人口和就業的增加，而非中九龍幹線所引致。

在最新的交通影響評估草擬報告中，對於關鍵路段和交叉口，“顧問”也提出過一些臨時的/長期的當地交通改善措施。然而，這些措施只能在局部地區帶來有限的舒緩作用。要徹底改善來往中九龍東西方向的交通問題，必須儘早興建中九龍幹線。

“顧問”證實，提出的中九龍幹線走線是必需的，從而把現時東-西走廊上的交通分流出來，以此緩解該“走廊”上的交通壓力。

另外，中九龍幹線能夠使乘客從縮短的行車時間方面得到益處。基於“顧問”的交通模型預測，在修訂過的最新經濟評估草擬報告(編號：REP-077-01)中，表6詳細列出了由中九龍幹線產生的平均節省時間。注意到對私家車而言，從2021年到2060年，中九龍幹線每年節省時間效益額僅在23%到29%之間。然而，每年超過70%的節省時間效益額則屬於不同類型的商用車輛，包括的士，小巴，貨車，客車和公共巴士。



表 6 從 2021 年到 2060 年有中九龍幹線每年節省時間 (乘客小時)

類型	2021	2030	2040	2050	2060
汽車	(23%) 10470	33,525	42,155	50,001	(29%) 57847
的士	4,362	12,652	15,981	19,008	22,035
特殊用途汽車 (SPB)	3,649	11,011	14,480	17,634	20,789
客貨車	1,100	3,661	4,658	5,565	6,472
輕型貨車 (LGV)	887	2,991	3,802	4,539	5,277
中型貨車 (MGV)	715	2,096	2,670	3,191	3,713
重型貨車 (HGV)	134	368	466	555	644
拖車 (TU)	326	1,048	1,293	1,516	1,738
公交巴士 (PT)	23,846	57,388	65,740	73,333	80,926
總額 (100%)	45,490	124,740	151,246	175,343	199,440

來源: 修訂過的最新經濟評估草擬報告(編號：REP-077-01)

4. 最低限度的臨時填海範圍

4.1 中九龍幹線的選址限制

為了評估有否用最低限度的臨時填海範圍來滿足中九龍幹線的建造要求，“專家”對滿足相關公路設計標準的首選最短路線長度進行了獨立評估。從圖 1 中可以看出，在啓德發展區，提出的 S 曲線對要求的最低限度的臨時填海範圍有重大的影響。“專家”認為中九龍幹線至少有四個選址限制，這些限制與首選最短 S 曲線長度有密切關係。這四個選址限制總結如下：

- (1) 在東部，中九龍幹線需要與 T2 路段相連接構成完整的 6 號幹線。
- (2) 中九龍幹線的一個關鍵連接點位於啓德發展區之交匯處。它與啓福路，啓祥路，以及未來啓德發展區的其他道路相連接。為了構建一個立體交匯點，中九龍幹線的主幹道需要爬升到地面水平線之上，如圖 1 所示。
- (3) 該路線可以避免回收現有住宅土地。在這個原則下，只有穿越海底是可行的方案，且最短的海底路線需要從九龍城碼頭走廊下面穿過，直達啓德發展區。
- (4) 在通過啓德河的河灣處有一個限制，要滿足一條最小寬度為 15 米的行人道。因此，需要考慮反向曲線(S 曲線)的最小可行平面曲線半徑是否合理。

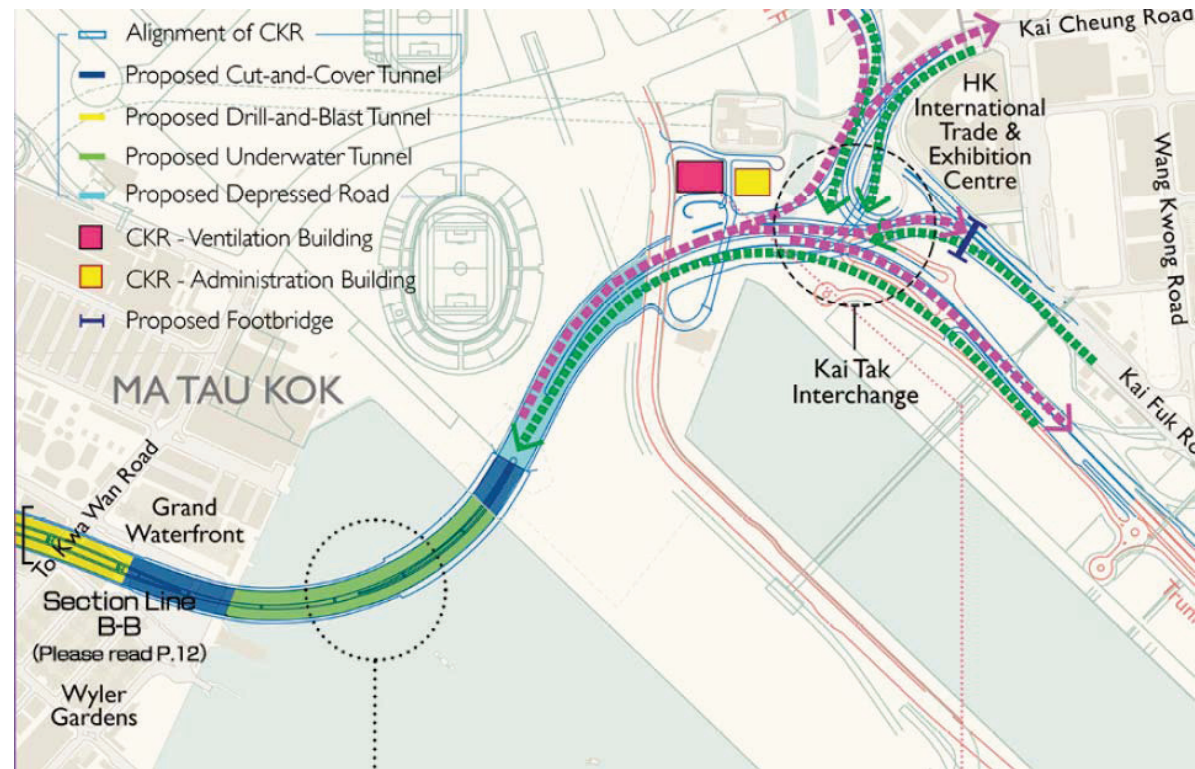


圖 1 -中九龍幹線在啓德發展區的 S 曲線

4.2 公路設計標準

鑒於提出的中九龍幹線啓德發展區 S 曲線路線，爲了驗證中九龍幹線最低限度的臨時填海範圍的合理性，有必要評估其是否滿足相關的公路設計標準（特別是 S 曲線的最小可行半徑）。考慮到中九龍幹線主幹道的設計速度爲 80 公里/小時，中九龍幹線海底路段 S 曲線的最小可行半徑是 330 米，最大坡度爲 4% 的路段長度大約是 900 米。

在香港，交通規劃設計手冊(TPDM) 對公路設計速度有如下不同的要求：

- 公路的設計速度與公路的各種設計特性有密切關係，例如：最小平面和垂直面曲線，路面傾斜度，能見距離，指示牌和路標等。下表(a)比較了香港，英國，美國郊區和市區的公路設計速度。



(a) Design speed 設計速度

		香港(HK)	英国(UK)	美国(USA)
郊區	Rural area	100 km/h	120 km/h	80 - 110 km/h
市區	Urban area	70 km/h (80 km/h for new roads) or above	Less than 120 km/h	80 - 110 km/h

由於中九龍幹線位於九龍市區，其主要目的是爲九龍東西方向的長途交通提供服務，因此，從上表(a)可以看出，中九龍幹線主幹道 80 公里的設計速度屬於國際公路設計標準的下限。

在啓德發展區，爲了平衡中九龍幹線平面曲線處的離心力，可行的最大路面傾斜度設定爲 7%。因此，滿足要求的最小平面曲線半徑爲 $R_{min} = V^2/2.822 (7\%)$

中九龍幹線設計速度 $V = 80$ 公里/小時; $R_{min} = V^2/2.822 (7\%) = 324 \text{ 米} < 330 \text{ 米}$

通過上面的分析可知，中九龍幹線海底路段 S 曲線的最小半徑 330 米接近滿足要求的最小平面曲線半徑。

另一方面，爲了道路安全，還需要驗證在中九龍幹線海底路段上，330 米長的最小 S 曲線半徑是否能夠提供最小能見距離(S)。下表(b)是根據香港，英國，美國採用的設計速度計算出的最小能見距離。

(b) Sight distance 能見距離

Design speed (km/h)	Minimum sight distance (m)				
	香港 (HK)		英国 (UK)		(USA) 美国
	Desirable	Absolute	Desirable	Absolute	
120	295	215	295	215	250
110	-	-	-	-	220
100	215	160	215	160	185
90	-	-	-	-	160
85	160	120	160	120	-
80	145	110	-	-	130
70	120	90	120	90	105



因為中九龍幹線主幹道的設計速度為 80 公里/小時，因此，最小能見距離(S)不能小於 110 - 145 米，最小能見距離受最小平面曲線半徑(R) 330 米的影響。這個結論可從下面的關係中得到。

$$s = \sqrt{8RT}$$

在中九龍幹線海底的公路隧道中，左側車道中心與障礙物之間的距離等於 $(3.65/2) + 3.0 + 1.7 = 6.525$ 米，

把 $R=330$ ， $T=6.525$ 米代入上面的等式中， S 就等於 **131** 米。所以，最小能見距離(S) 位於可行最低要求的 110 - 145 米之間。

考慮到中九龍幹線的設計速度為 80 公里/小時，基於下面的表(c)，為了從九龍城碼頭走廊下及啓德地面上穿過，選擇的最大可行坡度為 4%，從而縮短海底隧道的長度和減小臨時填海的範圍。

(c) Gradients 坡度

Design speed (km/h)	Maximum gradient				
	香港(HK)		英国(UK)		(USA)
	Desirable	Absolute	Desirable	Absolute	美国
120					-
110	4%	8%	3%	4%	5%
70 - 100					between 5% and 12%

上面的分析，證明在啓德發展區的中九龍幹線最短 S 曲線設計能夠滿足相關的公路設計標準，且是可行最小的。因此，在建造中九龍幹線過程中，建議的走線能夠達到最低限度的臨時填海範圍。



5. 獨立評估和結論

5.1 凌駕性公眾需要

為了評估中九龍幹線對當地的交通影響，“顧問”已經實施了綜合交通調查以便對區域交通模型進行校準驗證。結果證明模型的最大誤差通常小於 10%。採用已經校準的區域交通模型，“顧問”開展了未來設計年有中九龍幹線和無中九龍幹線兩種情況下的交通預測和經濟評估。該評估證實，中九龍幹線是至關重要的，因為它能夠緩解中九龍地區的交通擁堵問題。“專家”認為，“顧問”提出的假設及交通預測是合理的，並且支持“顧問”的評估結果。

根據以前運輸研究(例如 CTS-3)的預測，沿九龍東西走廊的交通需求將會進一步增加。以前的研究也證實，確實需要增加一條東西幹線(中九龍幹線)以避免更廣泛和頻繁的交通擠塞，也為了避免由於發生事故(例如 2005 年 5 月 9 日的嚴重塌棚架事故)而導致重要路段和主要交叉口的交通堵塞。

現場交通調查證明：中九龍地區的東西走廊已經處於超出負荷運行狀態。沿東西走廊的擠塞並不限於平時工作日的早晚高峰時段。根據 2011 年年度交通調查報告，九龍東西走廊上的交通流量(通過調查線 A-A)在工作日的上午 8 點和下午 7 點確實處於飽和狀態。

根據“顧問”對 2021 年有中九龍幹線和無中九龍幹線兩種情況下的交通預測，“專家”在走廊調查線 A-A 上實施服務水平(LOS)的分析(對九龍東西方向的交通)。結果發現，到 2021 年，有中九龍幹線和無中九龍幹線兩種情況下調查線上的服務水平分別為 D 和 F。下表列出了不同服務水平標準。



Level of Service	V/C Ratio	交通狀況 Corresponding Traffic Condition
A	Up to 0.3	自由流狀況.
B	>0.3 - 0.5	暢通的车流狀況.
C	>0.5 - 0.75	般暢通的中流狀況.
D	>0.75 - 0.9	穩定性的中流狀況.
E	>0.9 - 1.1	不穩定性的中流狀況.
F	> 1.1	強迫性的车流狀況.

“專家”認為，到 2021 年，如果無中九龍幹線，東西走廊之間的道路服務水平將是 F，不能滿足社會需求是不能夠接受的。

交通管理措施已經發揮作用，最大程度地提高現有道路容量及抑制高峰時段的交通需求。但所有這些措施還不能解決沿東西走廊的交通擠塞問題。因此，建造中九龍幹線是完全必要的，雖然實時行車時間系統 (JTIS) 和電子道路收費 (ERP) 對中九龍幹線有輔助作用，但不能夠替代中九龍幹線。這是因為如果不建設中九龍幹線，現時的東西走廊就沒有剩餘容量來滿足持續增加的私家車和商用車出行。

2011 年年度交通調查證實，穿越九龍東西走廊之間 (通過調查線 A-A) 的車輛，超過 60% 是商用車輛 (例如：的士，小巴，貨車，客車和公共巴士)。為了滿足未來經濟增長產生的商用交通需求，有必要興建中九龍幹線來提高九龍半島東西走廊的連貫性和可靠性。然而，“專家”建議，政府應該解決需求問題來調節走廊地區的土地開發，避免在中九龍幹線開通前加重走廊地區的交通擠塞問題。

最後，“專家”贊同“顧問”為雙程 3 線中九龍幹線所做的交通影響評估結果，“專家”認為，從交通需求角度考慮，有必要建設中九龍幹線，以避免給中九龍地區帶來不可承受的交通擠塞。

5.2 最低限度的臨時填海範圍



最低限度的臨時填海範圍與首選最短路線長度及相關公路設計標準有密切的關係。鑒於上述 4 個中九龍幹線選址的客觀限制，建議中的反向曲線 (S 曲線) 能夠滿足最低限度的臨時填海範圍要求。

在建造中九龍幹線過程中為了減小臨時填海範圍，啓德發展區的中九龍幹線最短 S 曲線的設計參數 (例如：設計速度是 80 公里/小時，平面曲線半徑是 330 米，最大坡度是 4%) 是可接受的，但屬於國際標準的可行範圍下限。

為了道路安全的目的，中九龍幹線首選最短路線充份考慮了選址的客觀限制和有關公路設計標準。因此，中九龍幹線最低限度的臨時填海範圍是合理的。

5.3 結論

(1) 研究發現，當路段的 V/C 比率 (路段流量對路段通行能力的比率) 接近 0.9 或主要交叉口的剩餘通行能力低於 10% 的時候，將會出現不穩定性的车流狀況和隨機性的車輛排隊。如果不開通中九龍幹線，在未來幾年，這種不穩定性的车流狀況將會持續惡化，且變得不可接受。

(2) 總言之，從交通論證方面，為了在九龍東西走廊上提供剩餘通行能力，以滿足未來經濟發展增加的交通需求，雙程三線的中九龍幹線具有凌駕性公眾需要。此外，“專家”認為，交通預測結果甚至可能偏低，因為在草擬和補充的交通影響評估報告中沒有充分考慮香港近期的經濟增長及最新的未來發展規劃帶來的影響。

(3) 最後，根據最低限度的臨時填海範圍與首選最短路線長度及相關公路設計標準的關係，“專家”贊同中九龍幹線 S 曲線的設計，認為具有最小可行半徑的 S 曲線 (在啓德地區) 是合理的。同時，“專家”也認同，為了道路安全的目的，中九龍幹線最低限度的臨時填海範圍考慮了選址的客觀限制和公路設計的標準。

***** END *****



PolyU Technology & Consultancy

Company Limited

理大科技及顧問有限公司

Prepared by

Ir Professor William H.K. Lam

BSc, MSc, PhD, CEng

Chair Professor of Civil & Transportation Engineering

Department of Civil and Environmental Engineering

The Hong Kong Polytechnic University

Yuk Choi Road

Hung Hom, Kowloon

HONG KONG

Tel : (852) 2766-6045

Fax : (852) 2334-6389

E-mail: cehklam@polyu.edu.hk

Web Site: www.cse.polyu.edu.hk/~cehklam

香港九龍紅磡理工大學 QR 棟 6 樓 QR603 室

QR603, 6/F, QR Core, The Hong Kong Polytechnic University, Hunghom, Kowloon, Hong Kong.

電子郵編 E-mail: ptec@inet.polyu.edu.hk 電話 Tel: (852) 3400 2704 / 3400 2714 傳真 Fax: (852) 2356 7583

附錄二

吳宏偉教授 - 關於九龍灣臨時
填海工程具有力和令人信服的
材料報告之獨立專家審查

獨立專家評審報告

中九龍幹綫（CKR）施工方法評審

目錄

1. 引言
2. 評審原則和審閱的文件
3. 九龍灣地區的地質和地貌條件
4. 施工方法的選擇
5. 結論

參考文獻

圖表

附錄 — 四篇學報論文

- a. **Ng, C. W. W.**, Rigby, D., Lei, G. & Ng, S. W.L. (1999). 短地下連續牆的工作性能. 英國岩土工程學報, 1999, 49 (5): 681-694.
- b. **Ng, C. W. W.**, Rigby, D., Ng, S. W.L & Lei, G. (2000). 香港壁板樁的現場監測研究. 美國岩土及環境岩土學報, 126 (1): 60-73.
- c. **Ng, C. W. W.**, Lu, H. & Peng, S.Y. (2012). 雙平行隧道開挖對已有樁基影響的三維離心試驗研究. 隧道與地下空間技術, 已接收. <http://dx.doi.org/10.1016/j.tust.2012.07.008>.
- d. Wong, K. S., **Ng, C. W. W.**, Chen, Y.M. & Bian, X.C. (2012). 隧道開挖面在砂土中被動破壞的離心模型試驗及數值模擬研究[J], 隧道與地下空間技術, 28: 297-303.

吳宏偉

香港科技大學土木及環境工程學系講座教授

岩土工程離心機實驗所主任

中國教育部長江學者講座教授

劍橋大學邱吉爾學院海外院士

香港工程科學院院士

1. 引言

香港特區政府路政署計劃興建一條長約 4.7 公里的橫貫中九龍的幹道，採用雙程三線分隔車道的設計，將連接西九龍填海區和東九龍擬建啟德發展區。中九龍幹道西端連接現有西九龍公路的油麻地交匯處，向東連接擬建啟德發展區的 T2 主幹道，延伸至將來的將軍澳-藍田隧道。所有這些幹道將會成為連接西九龍和將軍澳的香港 6 號幹綫的一部分。

受特區政府路政署委託，2007 年莫特麥克唐納-邁進-安誠顧問聯營公司 (JV) 依據合同 (合同號: CE58/2006(HY))，對中九龍幹綫 (CKR) 和加士居道行車天橋擴闊工程進行了初步設計。隨後於 2010 年年末，奧雅納-莫特麥克唐納聯營公司 (AMMJV) 依據合同 (合同號: CE43/2010 (HY)) 對此進行了詳細設計。

本人作為獨立專家參與了全程設計的評審^[5]。對於擬建的中九龍幹綫，主要有兩個技術難點：首先是在九龍城和九龍灣附近道路的走線選擇問題；其次是採用何種施工方法。在之前的獨立專家審核報告^[5]中，已經討論了中九龍幹綫的重要性，並確定了合理的道路走線。因此，本次的審核報告將著重於審核和評估擬採用的施工方法。

2. 評審原則和審閱的文件

本次獨立評審，本人對以下四個文件作了詳細評估：

- 中九龍幹綫 — 設計與施工：隧道施工的岩土風險管理草案 (2012 年 7 月 27 日)
- 中九龍幹綫 — 設計與施工：更新的經濟評價修訂草案 (2012 年 10 月 24 日)
- 中九龍幹綫 — 設計與施工：關於九龍灣臨時填埋的最終驗證材料 (2012 年 12 月 21 日)
- 中九龍幹綫 — 2013 年 1 月 11 日舉行的，關於九龍灣海底隧道建設的專業會議上的發言稿

除此以外，本人還參加了許多相關會議。包括 2013 年 1 月 7 日由海濱事務委員會承辦的會議，1 月 11 日的專業論壇，以及在油麻地 (2013 年 1 月 12 日) 和九龍城 (2013 年 1 月 19 日) 舉辦的公共論壇。

在本評估報告中，將結合本人已有研究成果、發現和出版物，對擬採用的施工方法進行綜合評審。

3. 九龍灣地區的地質和地貌條件

本人於 1999 年在九龍灣地區承擔過一個科研項目，研究 40 米長的壁板樁的工作性能，因此對九龍灣地區進行過獨立的場地勘察。該樁位於九龍灣，且毗鄰原啟德機場跑道東部，具體位置參見圖 1，Ng 等^[4]於 2000 年對該方樁進行了壓樁試驗。圖 2 詳細記錄了測井曲線以及測量的標準貫入數（STP-N）。該論文的副本附在附錄中。Ng 等^[3]詳細記錄了該方樁施工引起的地表水平和垂直位移。如圖 2 所示，該場地是由人工填海形成，相對基準面高程約為 4.5 米，地下水位於地表以下 3 米。該地質剖面由上到下依次為：6 米人工填土、9.5 米海洋粘土沉積物、7.5 米砂質粘土（機可能是沖積形成）、4.8 米第四紀沖積砂層以及約 12 米全風化花崗岩殘積土，底層為上侏羅紀到晚白堊紀的花崗岩。由圖可知，在所有土層中標準貫入錘擊數很小而且很分散。作為初步估計，土體不排水抗剪強度（單位：kPa）可以通過標準貫入數（SPT-N）與經驗係數 4 相乘得到，由此可以清晰的看到，九龍灣地區表層 30 到 40 米土體的抗剪強度很低。Ng 等^[3]於 1999 年對該區地下連續牆的工作性能進行了三位數值反分析，得到的有效抗剪參數（有效粘聚力 C' 和有效內摩擦角 ϕ' ）同樣印證了上述結果。具體圖表和其它分析結果可以參見所附的論文副本。除此以外，根據 Ng 等^[3]在該測試場地收集得到的鑽孔資料，可以看出該區基岩埋深顯著增加。由奧雅納-莫特麥克唐納聯營公司（AMMJV）提供的勘察結果和上述發現相吻合。

4. 施工方法的選擇

任何地下建築物（如隧道）的施工方法選取都必須要首先考慮地質情況和岩土體性質。對於擬建的中九龍線，西線所處位置基岩埋深非常淺，非常適合隧道施工。但是在土瓜灣道以東地質情況急劇惡化，在九龍灣地區基岩埋深降至海平面以下 50 米。

關於擬建中九龍幹綫隧道的最佳走綫，在九龍城和九龍灣地區存在一些施工難點，這些急需解決的問題包括：

- 人口密度大，大量私人領地和住房 — 擬建中九龍幹綫涉及的任何房屋拆遷和土地徵用都將面臨所有權問題，而且為了避免公共恐慌，任何由施工引起的地表位移和房屋破壞都必須被認真處理。
- 擬建幹綫東端惡劣的地質情況 — 正如第三部分所提到的基岩埋深大，上覆巨厚的軟弱土層（抗剪強度很低），因此基於經濟和安全考慮，不宜採用鑽挖法施工。
- 道路坡度設計必須考慮安全性和合理性。

奧雅納-莫特麥克唐納聯營公司（JV）通過對超過 40 個方案的篩選，確定了 5 個優選方案（編號為 A 到 E）。雖然選綫 A（由許多幹綫組成的內陸綫）可以避免臨時填海，但是道路通過

地區下部缺乏足夠基岩來支持建築基礎。隧道如果採用明挖法，沿綫的許多私人住宅都必須被拆除，但在現有的工期和資金支持下，這幾乎是不可能完成。除此以外，為了與九龍灣道路網和 T2 主幹道相連，選綫 A 要求中九龍幹綫必須採用大坡度的設計方案。根據以上要求和困難點，基本可以排除走綫 A 的可行性。而且，擬建的路塹段無法和未來的啟德發展中心的多功能綜合體育館協調統一。

對於選綫 C, D 和 E，它們都需要穿過大量的私人領地和民用建築。任何房屋拆遷和土地徵用都將面臨所有權問題。與這三條選綫相關的隧道施工問題將在後面進行討論。因此，這三條走綫也不宜採用。

選綫 B 作為唯一的可行方案，奧雅納-莫特麥克唐納聯營公司研究並提出了三種可供選擇的隧道施工方法。他們分別是：

- 沉管法（IMT）
- 鑽挖法/鑽爆法
- 圍堰明挖法（需要臨時填海）

前兩種施工方法不需要進行填海，但是第三種需要在九龍灣地區進行部份臨時填海。沉管法施工會涉及河床的大面積疏浚，最大疏浚深度為 30 米，最闊疏浚寬度約為 220m。但是如此大的清淤量有可能會引起嚴重的環境問題，如何處理挖到的淤泥也是一個巨大的挑戰。為了建造深槽，需要拆除九龍城渡輪碼頭，中華煤氣公司運載原材料碼頭和馬頭角公眾碼頭，而且碼頭角永久海堤需要進行加固，以避免過度的地表沉降。但是和選綫 C, D 和 E 的疏浚量相比，選綫 B 的疏浚量是微乎其微的。

對於鑽挖法或者鑽爆法，為保證安全，需要良好的地質條件及足夠的土層覆蓋厚度來提供支護，防止隧道的被動失穩破壞^[6]。考慮到九龍灣的高地下水位，以及不利的土體條件和性質，可以採用泥漿護壁法或者土壓平衡法進行隧道施工（如圖 3 所示）。圖 4 所示的大直徑隧道掘進機只是作為一個參考。由於採用雙程三線道路設計以及東部啟德交匯處存在的高程要求，這些都使得鑽爆法變得非常不利，但又沒有其它的替代設計方法（如圖 5 所示）。同時考慮到西線所需的超大直徑鑽孔隧道（最大可至 20.5m）以及九龍灣東部非常小的土層覆蓋厚度（小於 1.5 倍的隧道直徑），因此對隧道施工面施加恒定壓力，以抵抗外部呈三角形分佈的土壓力和水壓力的做法將會變得極其困難和危險。這些不利條件會對施工工人和公眾產生潛在的風險。比如，1998 年 2 月 23 日在英國碼頭區(Docklands)輕軌線施工過程中，隧道施工面產生了擠出破壞（如圖 6 和圖 7 所示）。主要原因是泥水盾構面的上覆土層厚度太小（C/D 太小），導致被動破壞產生，該破壞發生於早上 5 點鐘，在當地的一所小學的操場上形成了一個直徑為 22 米的深為 7 米的巨坑，該隧道失穩還導致 100 米外的居民玻璃破碎^{[1][2]}。不難想像，如果失穩發

生時，小學生們正在操場上玩耍，那麼將會產生嚴重的傷亡。同樣我們需要注意的是，英國碼頭區(Docklands)輕軌線隧道直徑只有 5.2 米，遠遠小於擬建中九龍線隧道的直徑（最大為 20.5 米）。

本人最近在香港科技大學岩土離心機實驗室，模擬了直徑為 4.46 米的隧道的被動破壞（如圖 8 所示）。研究表明，隧道的被動失穩破壞是受上覆土層厚度與隧道直徑的比例（C/D）控制的，而且很難進行預測^{[6][8]}。C/D 的值越小，施工的風險就越大。為了獲取足夠的上覆土層保護而加大擬建中九龍幹綫隧道的埋置深度，這同樣不是一個可行的方案，因為加深隧道位置將使得中九龍線無法與啟德交匯區連接。

一些工程師可能認為，在九龍灣隧道施工前，對土地進行注漿或者進行冷凍。但這些方法的風險性很大，而且可能會對海灣環境產生危害。世界範圍內的隧道上施工經驗表明，在淺埋區和不良地質區，採用鑽挖法施工是極其危險的。同時，隧道掘進機法（TBM）同樣不可行，因為擬建隧道直徑最大將至 20.5 米，目前，世界上還沒有如此大直徑的隧道掘進機。因此，對於道路選線 B, C, D 和 E，採用任何淺埋隧道施工方法建造土瓜灣路段都將很危險，費時而且昂貴。除此以外，如果選用淺埋隧道施工方法，那麼大直徑中空鑽挖隧道將需要解決抗浮的問題。

在奧雅納-莫特麥克唐納聯營公司（AMMJV）提供的三種可選施工方法中，本人認為垂直剛性圍堰配合明挖法是唯一合理和可行的方案。這是香港本地和國際上都非常常用的施工方法。香港工程師和承包商對此都非常熟悉且經驗豐富，因此可以將風險降到最低。圍堰施工分兩步修建垂直間隔牆，以最大限度減小對海灣水循環的有害影響。雖然階段一和階段二的臨時填海分別需要填土 1.8 公頃和 2.0 公頃，但和沉管法（IMT）相比，仍然可以減少 300%的清淤量。根據對現有設計難點，地質條件和土體性質的認識，將兩個回填階段工期均設為 26 個月是合理的。

考慮到擬回填施工的寬度和範圍，水下明挖法能有效的減少回填量，因為隧道將會沿著垂直間隔牆進行現場澆築，因而可以省去混凝土模板，進而減小回填寬度。本人十分確信，不存在其它更加合理的替代方法，而且採用豎直間隔牆能把損害和回填量降到最低。同時需要指出的是，在九龍灣的所有選線方案 C, D 和 E 中，方案 B 的明挖法配合圍堰施工所需的回填量是最小的。

2013 年 1 月 19 日在九龍城地區舉行的公眾論壇上，許多居民擔憂在高程建築下部開挖隧道會導致房屋傾斜以致危害安全。根據本人開展的關於隧道開挖對樁工作性能影響的研究^[6]表明，如果房屋的設計和施工嚴格按照標準進行，那麼在高質量岩體中鑽挖隧道應該不會影響上部建築的安全和正常應用。

5. 結論

根據對這些現有資料的詳細審查，同時結合本人已有的科研成果，本審核人確信選線 B，以及臨時填海結合明挖法施工是最符合以下三個標準的方案：1) 必須的，高於一切的且需要的，2) 不存在其它合理替代方案，3) 產生最小的破壞和使用最小的回填量。綜合分析，對於擬建的中九龍幹綫不存在其它替代施工方案，擬採用方案的回填量是最小。

參考文獻

1. ICE (1998). Bulkhead location blamed for DLR blast. *New Civil Engineer*, Institute of Civil Engineers, February Issue, 3-4.
2. ICE (2004). Docklands tunnel blowout down to “elementary error”, says judge. *New Civil Engineer*, Institute of Civil Engineers, January Issue, 8-9.
3. Ng, C.W.W., Rigby, D., Lei, G. & Ng, S. W.L. (1999). Observed performance of a short diaphragm wall panel. *Geotechnique*. Vol. 49, No.5, 681-694.
4. Ng, C.W.W., Rigby, D., Ng, S. W.L & Lei, G. (2000). Field studies of well-instrumented barrette in Hong Kong. *Journal of Geotechnical and Geo-environmental Engineering, ASCE*. Vol. 126, No. 1, 60-73.
5. Ng, C.W.W. (2009). *Independent Expert Review Report: Review of Construction Method for the Central Kowloon Route*. Highways Department.
6. Ng, C. W. W. & Wong, K.S. (2012). Investigation of passive failure and deformation mechanisms due to tunnelling in clay in centrifuge. *Canadian Geotechnical Journal*. Accepted.
7. Ng, C.W.W., Lu, H. & Peng, S.Y. (2012). Three-dimensional centrifuge modelling of twin tunnelling effects on an existing pile. *Tunnelling and Underground Space Technology*. In Press. <http://dx.doi.org/10.1016/j.tust.2012.07.008>.
8. Wong, K. S., Ng, C. W. W., Chen, Y.M. & Bian, X.C. (2012). Centrifuge and numerical investigation of passive failure of tunnel face in sand. *Tunnelling and Underground Space Technology*. Vol. 28, 297-303.

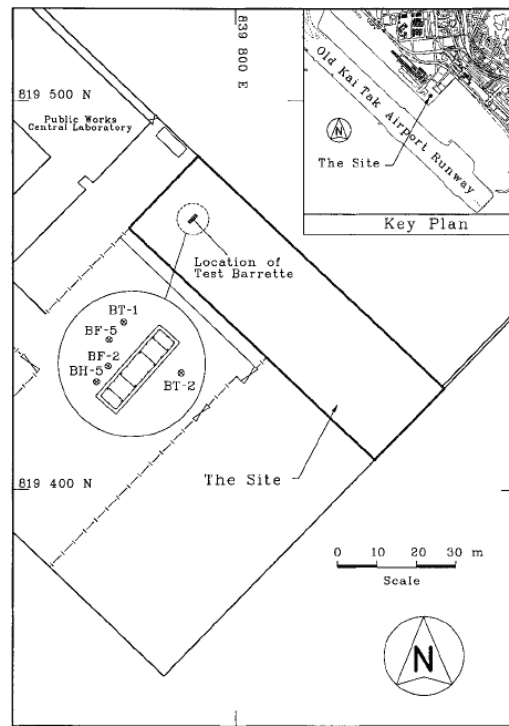
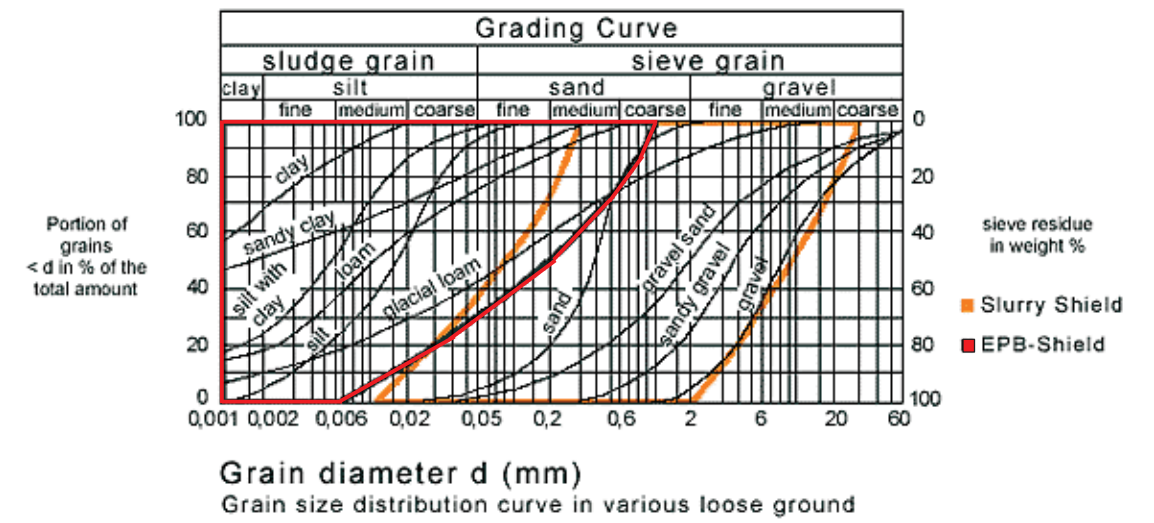


Fig. 1 Independent study -Ground conditions at Kowloon Bay (Ng et al, 2000)
(九龍灣土質)



EPB is generally applicable for clay to clayey sand where permeability is relatively low
(土壓平衡盾構法適用於低滲透性的粘土和粘性砂土)
Fig. 3 Grading curve related to the choice of EPB shield
(盾構選擇與級配曲線的關係)

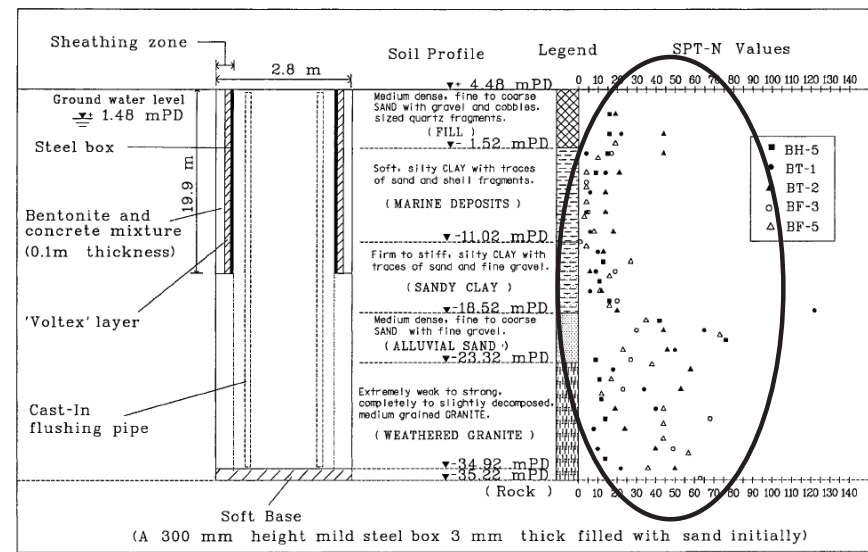
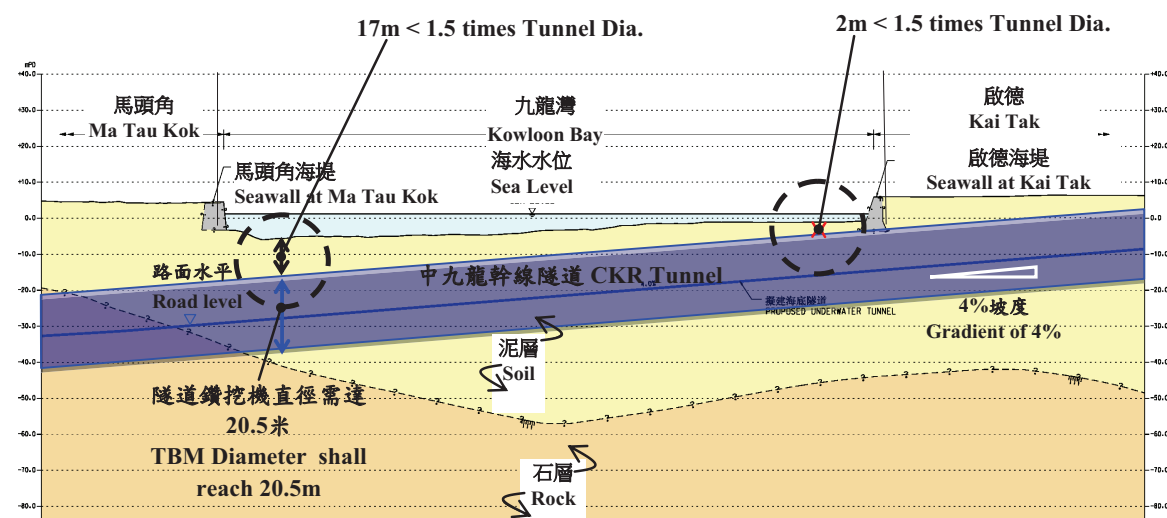


Fig. 2 Poor ground conditions at Kowloon Bay (Ng et al, 2000)
(九龍灣土質: 土質鬆軟 - 厚軟土層, 較深石層)

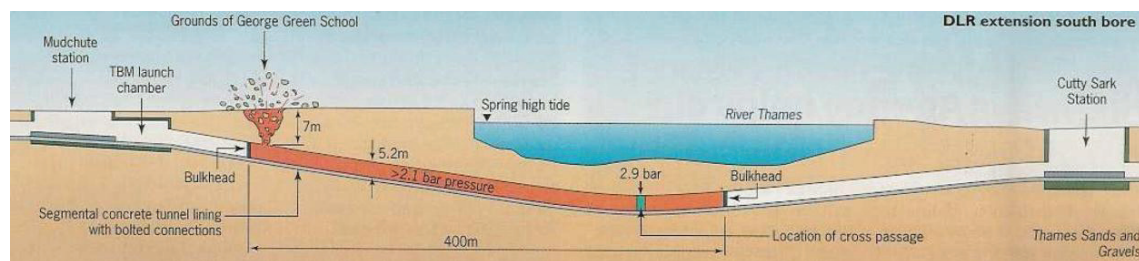


Fig. 4 Tunnel Boring Machine
(隧道挖掘機)



Bored tunnel method is not feasible 鑽挖施工是不可行的

Fig. 5 Proposed Bored Tunnel Construction Method for CKR
(鑽挖隧道施工方案)



ICE (1998)

- Diameter = 5.2 m (隧道直徑 5.2 米)
- Slurry shield boring machine using compressed air (泥水盾構施工法)

Possible causes of failure (可能的破壞因素)

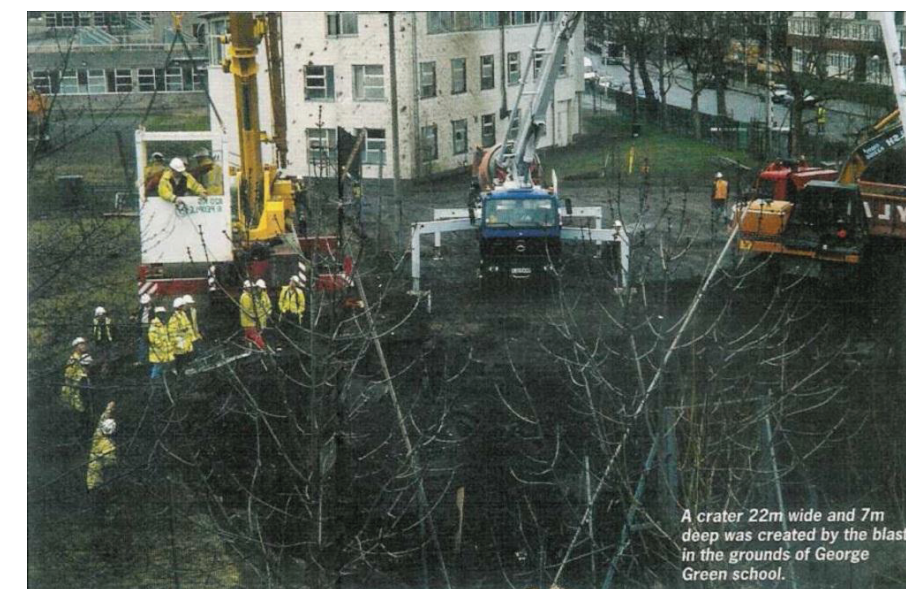
- Insufficient overburden above the tunnel (隧道上覆土自重不足)
- High compressed air pressure (2.2 bar) within tunnel causing blowout failure (隧道前方掌子面氣壓過大)

Fig. 6 Blowout Failure of Docklands Light Rail (extension) in UK on 23 Feb. 1998

(1998年2月23日英國碼頭區(Docklands)輕軌的隧道開挖面湧出破壞)

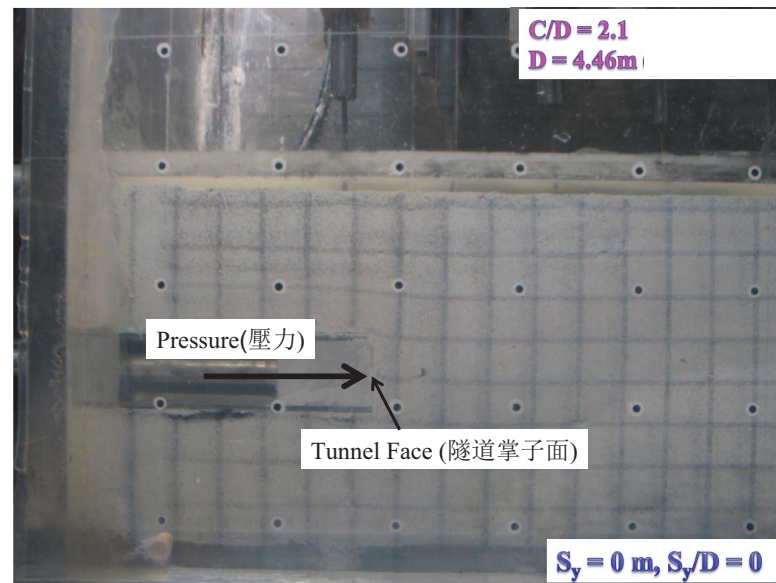


The compressed air blast left a huge crater in a Docklands school playing field.
The crater is 22 m wide and 7 m deep
(地面塌陷寬 22 米, 深 7 米)

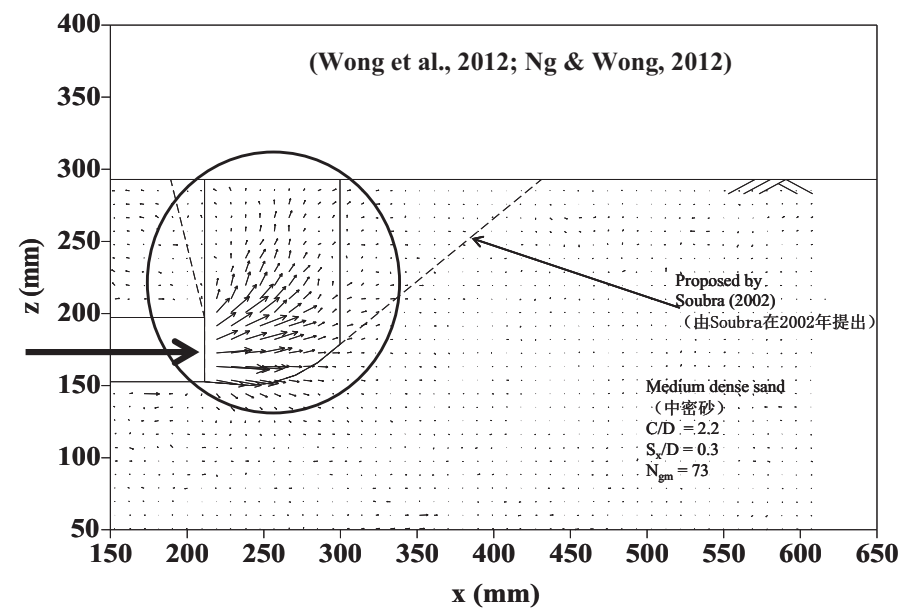


Massive crater due to compressed air blast
(因壓縮空氣引起的大面積地面塌陷)

Fig. 7 Crater formed in the ground of George Green school (ICE, 1998 & 2004)
(George Green 學校地面上形成的塌陷)



(a)



(b)

Fig. 8(a) Passive Failure (blowout) of Tunnel Face (隧道開挖面的被動(湧出)破壞的模型實驗); (b) Measured displacement vectors leading to blowout (實測湧出破壞的位移矢量)

1. Ng, C. W. W. & Wong, K.S. (2012). Investigation of passive failure and deformation mechanisms due to tunnelling in clay in centrifuge. *Canadian Geotechnical Journal*. Accepted.
2. Wong, K. S., Ng, C. W. W., Chen, Y.M. & Bian, X.C. (2012). Centrifuge and numerical investigation of passive failure of tunnel face in sand. *Tunnelling and Underground Space Technology*. Vol. 28, 297-303.

- a. Ng, C. W. W., Rigby, D., Lei, G. & Ng, S. W.L. (1999). 短地下連續牆的工作性能. 英國岩土工程學報, 1999, 49 (5): 681-694.
- b. Ng, C. W. W., Rigby, D., Ng, S. W.L & Lei, G. (2000). 香港壁板樁的現場監測研究. 美國岩土及環境岩土學報, 126 (1): 60-73.
- c. Ng, C. W. W., Lu, H. & Peng, S.Y. (2012). 雙平行隧道開挖對已有樁基影響的三維離心試驗研究. 隧道與地下空間技術, 已接收. <http://dx.doi.org/10.1016/j.tust.2012.07.008>.
- d. Wong, K. S., Ng, C. W. W., Chen, Y.M. & Bian, X.C. (2012). 隧道開挖面在砂土中被動破壞的離心模型試驗及數值模擬研究[J], 隧道與地下空間技術, 28: 297-303.

Observed performance of a short diaphragm wall panel

C. W. W. NG,* D. B. RIGBY,* G. H. LEI* and S. W. L. NG*

The construction in Hong Kong of a 40 m deep excavated, large, rectangular-section barrette (i.e. a short diaphragm wall panel, 2.8 m long by 0.8 m wide) in sedimentary and weathered soils under bentonite has been heavily instrumented and closely monitored. During excavation, the maximum measured horizontal ground movements were only a few millimetres, with similar subsurface settlements around the panel. On the basis of three-dimensional numerical simulations of the excavation of the trench, an average mobilized shear strain greater than 0.1% around the excavated trench can be deduced. At the soil–wall interface, the initial lateral earth pressures decreased to hydrostatic bentonite pressures during excavation and increased above their initial K_0 pressures after concreting. The measured lateral pressures just after concreting support a theoretical bilinear pressure envelope.

KEYWORDS: deformation; diaphragm and *in situ* walls; earth pressure; numerical modelling; pore pressures.

La construction d'une barrette à grande section rectangulaire excavée à 40 m de profondeur (c'est-à-dire d'un court panneau de mur souterrain de 2,8 m de long par 0,8 m de large) dans des sols sédimentaires et désagrégés sous de la bentonite a fait l'objet de nombreux contrôles aux instruments et a été observée de près à Hong Kong. Pendant l'excavation, les mouvements horizontaux maximum du sol qui ont été mesurés n'ont été que de quelques millimètres, avec des tassements similaires sous la surface autour du panneau. En nous basant sur des simulations numériques en trois dimensions de l'excavation de la tranchée, nous avons pu déduire une déformation de cisaillement mobilisée moyenne supérieure à 0,1% autour de la tranchée excavée. À l'interface sol-mur, les pressions terrestres latérales initiales baissent pour arriver au niveau des pressions de bentonite hydrostatiques pendant l'excavation et elles passent au-dessus de leurs pressions K_0 initiales après le bétonnage. Les pressions latérales mesurées juste après le bétonnage soutiennent la théorie d'une enveloppe de pression bilinéaire.

INTRODUCTION

The use of slurry trenches to construct diaphragm walls for underground structures has become a well-known technique in civil engineering. The construction of the diaphragm walls will inevitably cause initial stress changes and deformations in the ground (Clough & O'Rourke, 1990; Farmer & Attewell, 1973; Ng, 1992; Stroud & Sweeney, 1977; Symons & Carder, 1993). Various techniques, such as numerical modelling (Ng, 1992; Ng *et al.*, 1995) and centrifuge modelling (Powrie & Kantartzi, 1996), have been attempted to investigate stress transfer mechanisms and ground deformations due to diaphragm walling. Field monitoring of different panel sizes in different ground conditions is vital to provide essential data for verifying numerical and centrifuge results. In the Far East, well-documented case histories of

diaphragm walling are rarely reported in the literature, with one exception. Stroud & Sweeney (1977) carried out a detailed field trial of a diaphragm wall panel, 6.1 m long by 1.2 m wide and about 36 m deep, constructed at Chater Road on Hong Kong Island. Maximum horizontal subsurface movements of 28 mm and 10 mm were recorded at 1 m and 2 m, respectively, away from the face of the trench at about 16 m below ground level. A settlement trough with a maximum value of 6 mm was observed 3 m away from the face of the trench.

Recently the authors have had the opportunity to measure ground deformations and stress changes during the construction of a large, excavated, rectangular-section pile (barrette) for a University-led and industry-supported research project (Shen *et al.*, 1998). The excavation and concreting procedures used for the barrette were identical to those used in the construction of a diaphragm wall panel. The barrette was tested for its ultimate vertical load capacity three weeks after construction. However, in this paper, only the performance of the short diaphragm wall panel during construction is

documented as a case history. The observed ground deformations during the excavation of the trench of the diaphragm wall panel are compared with a three-dimensional numerical analysis. Moreover, stress and pore water changes at the soil/wall interface during concreting are reported and discussed.

SITE LOCATION AND GROUND CONDITIONS

The site is located on the Kowloon peninsula of Hong Kong, to the east of a runway of the old Kai Tak International Airport, adjacent to the Public Works Central Laboratory at Kowloon Bay (Fig. 1). Figs 2 and 3 show a cross-section of the test barrette and the location of some relevant boreholes, together with uncorrected N values from standard penetration tests (SPTs) measured in each soil stratum. The site is on marine reclaimed land and the ground level is at approximately 4.5 m above sea level or Principal Datum (PD). The groundwater level is at about 3 m below the ground surface. The ground conditions consist of, in succession, approximately 6 m of fill material, 10 m of marine deposits, 12 m of alluvium of Quaternary age and 12 m of weathered granitic saprolites overlying granitic rocks of Upper Jurassic to Lower Cretaceous age (Strange, 1990). The ground succession is similar to the site at Chater Road (Stroud & Sweeney, 1977).

It can be seen from Fig. 2 that very scattered SPT N values were obtained in both the alluvium sand and the weathered granite. It should be noted that the idealized geological strata shown in the figure may only be applicable to a local area around the trench. From borehole information, the depth to the rock head has been found to increase quite significantly from the south-east to the north-west direction at the site. The initial horizontal stresses in the ground are not known for certain at Kowloon Bay. However, it is generally believed that the initial K_0 values are less than 0.5 for soils in Hong Kong (Geotechnical Engineering Office, 1993).

DETAILS OF CONSTRUCTION

The test barrette or diaphragm wall trench was excavated using a traditional cable-operated grab. The size of the excavated trench was 2.8 m by 0.8 m in plan and 39.7 m deep (Figs 2 and 3). During construction, the trench was temporarily supported by bentonite slurry with a unit weight (γ_b) of 10.8 kN/m³. Soil spoil, suspended in the bentonite slurry, was removed after pumping to a desanding unit at the ground surface. After desanding, the bentonite was recharged into the trench. Chiselling of the base took place when the excavated depth reached about 39.6 m below ground level. This caused a small overbreak at the base which was detected by a sonic profiling system.

When the excavation reached its final level (39.7 m below ground level), three instrumented reinforcement cages were lowered and spliced together one by one into the trench, which was then concreted at an average rate of 10.32 m/h (or 23.12 m³/h) using a tremie pipe. The ordinary Portland cement (OPC) concrete used was grade C30/20 (design $f_{cu} = 30$ MPa) with a unit weight (γ_c) of 23.2 kN/m³. It had a water-to-cement ratio of 0.47 and an average slump of 180 mm. The average uniaxial compressive strength measured from a core taken from the centre of the barrette was 37.5 MPa at 28 days. During concreting, the average temperature measured inside the trench was 27.6°C. The excavation and concreting procedures of the barrette were in fact identical to those of the construction of a typical diaphragm wall panel.

At the upper reinforcement cages, a sheathing zone was formed (see Fig. 2) with the intention of minimizing the skin friction developed between the pile and the upper layers of the surrounding soil during axial load testing.

INSTRUMENTATION

The test barrette at Kowloon Bay was heavily instrumented. The prime objectives of the instrumentation were to study ground deformations due to the construction of the barrette (the diaphragm wall panel) and, more importantly, to investigate the load transfer mechanism and load–settlement characteristics of the barrette during axial load testing. In this paper, only the instrumentation related to the construction of the barrette is reported. Details of other instrumentation and the research strategy are described by Shen *et al.* (1998). Figs 3 and 4 show the locations of various instruments both in and around the trench.

Four Geokon vibrating-wire-total-earth-pressure cells, together with four vibrating-wire piezometers, were installed at the soil–wall interface at four elevations. Two total-earth-pressure cells were installed in both the alluvium and the weathered granite layers to measure total horizontal pressures at the soil–wall interface. The locations of the vibrating-wire piezometers were at about 80 mm above the corresponding pressure cells.

In addition, one pneumatic piezometer was installed inside borehole BF-4 (see Fig. 4) at 35 m below ground level in the weathered granite to monitor pore water pressure changes during the construction and testing of the barrette.

Magnetic extensometers were installed into three boreholes (see Fig. 4). The datum magnets were set into the rock, except in BF-3, owing to some construction difficulties encountered. The extensometers allowed subsurface soil movements to be measured by monitoring the location of each magnetic target with respect to the datum magnet.

Manuscript received 24 September 1998; revised manuscript accepted 16 February 1999.

Discussion on this paper closes 30 April 2000; for further details see p. ii.

* Hong Kong University of Science and Technology.

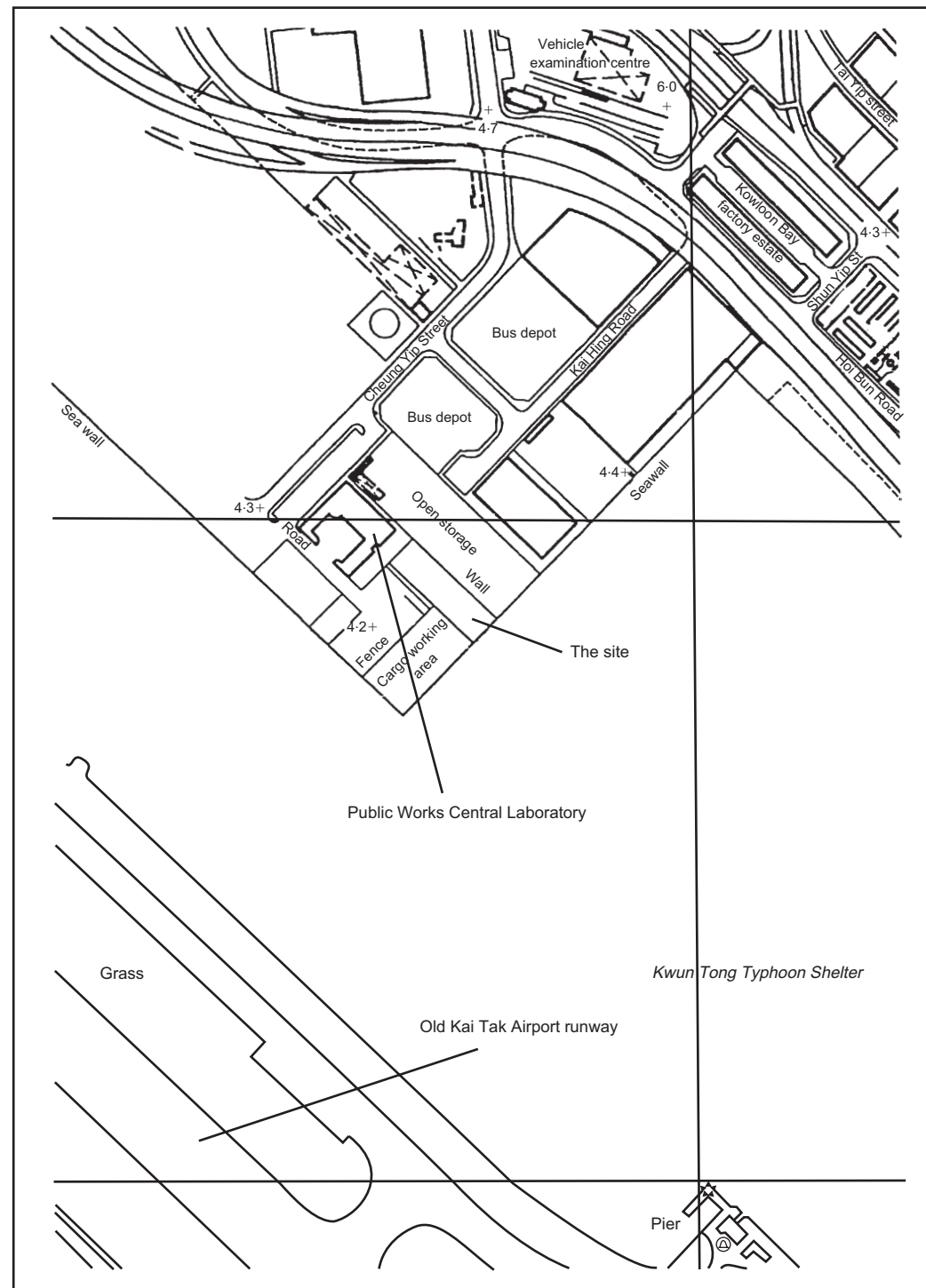


Fig. 1. Location plan of test pile site in Kowloon, Hong Kong

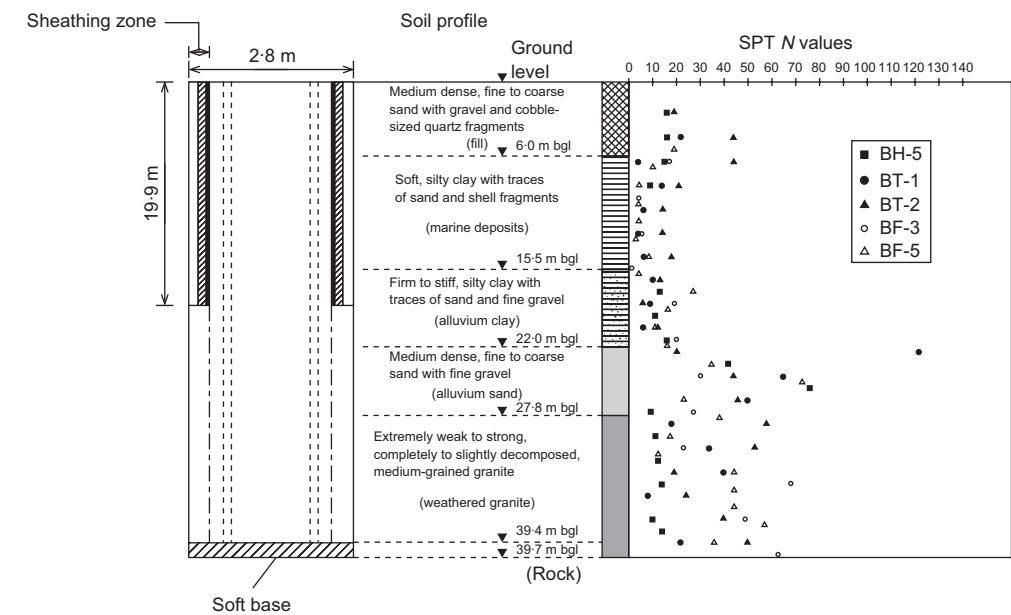


Fig. 2. Borehole logs and SPT *N* values at Kowloon Bay, Hong Kong (bgl, below ground level)

Three conventional inclinometer systems were installed in three boreholes, as shown in Figs 3 and 4. The bottoms of the inclinometers were fixed in rock. The inclinometers were used to measure rotations and hence the lateral movement of the soil around the trial barrette. In addition, settlement markers were installed around the trench, as shown in Fig. 3. The settlement monitoring system consisted of a steel rod. The bottom of the rod was concreted in a hole of 1.5 m depth below ground level. The settlement markers were used to measure surface settlements of the ground due to the construction of the diaphragm wall panel.

GROUND DEFORMATIONS DURING CONSTRUCTION OF THE BARRETTE

The excavation of the trench started on the morning of 5 December 1997 and was completed at midnight 7 December 1997. During excavation, the level of bentonite was kept at about 1.5 m above the ground water table (i.e. at about 3 m PD). The trench was then concreted in the afternoon of 9 December 1997. The horizontal deformation profiles measured are illustrated in Fig. 5. The measurements from the conventional inclinometers are of poor quality. This was probably because the actual movements were too small, only about 2.5 mm maximum horizontal ground movement towards the trench was observed at the ground surface in BF-5 (4 m away from the trench). The resolution of the inclinometers (0.1 mm deviation per metre or a maximum deviation of 4 mm over

the 40 m trench) was simply not good enough to differentiate any small movements induced on site.

The measured horizontal displacements generally decrease with depth, except for the localized large displacements appearing at about 32 m below ground level. This localized large ground deformation could be due to overbreak and loss of ground during chiselling at the base of the trench. Generally, small lateral deformations were observed and these may be attributed to limited stress relief during excavation (i.e. the initial horizontal stresses in the ground were not very different from the bentonite pressure) and the significant effect of soil arching (Ng, 1992; Ng *et al.*, 1995) around the relatively short panel length. Owing to the limited accuracy of the conventional inclinometers, no clear trend can be identified among the measured values from the three boreholes.

In the measured profiles at Charter Road (Stroud & Sweeney, 1977) and at Kowloon Bay, more significant deep-seated deformation was observed at the former than at the latter site. This was probably due to substantial soil yielding at deeper levels (large deviatoric shear stress) for the longer panel (6.1 m) at Charter Road. Deviatoric shear stress due to the difference between the vertical and horizontal effective stresses would be induced in the soil around trenches during excavation. On the other hand, soil arching around the shorter panel (2.8 m) seems to minimize the ground deformation at Kowloon Bay. Details of soil arching and stress transfer mechanisms due to the construction of a diaphragm wall panel are discussed by Ng *et al.* (1995).

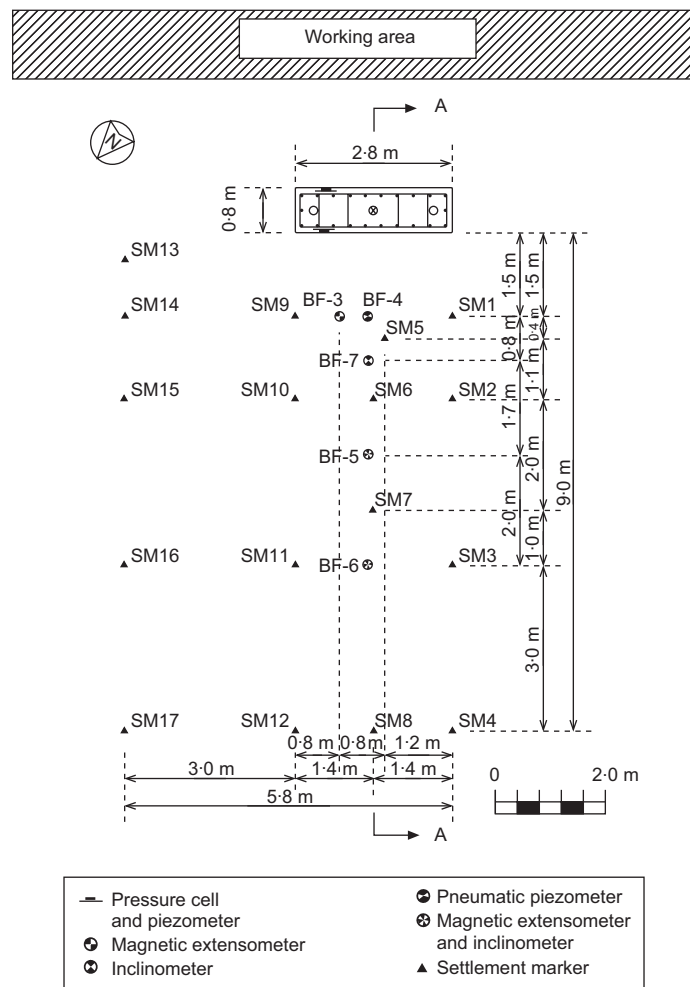


Fig. 3. Plan view of locations for instrumentation

During concreting, the ground surface was pushed, on average, about 1 mm outward laterally away at 4 m and 6 m from the trench by the wet-concrete pressure (see Fig. 5). It should be noted that the theoretical concrete pressure acting on the soil face was higher than the initial horizontal stresses in the ground. At 2.3 m from the trench (BF-7), the observed ground deformation is somewhat unexpected as the measurements indicate that there was a significant lateral movement (about 11 mm) away from the trench at 11 m below ground level (-6.5 m PD). Confirmation of the reliability of this substantial lateral movement can be obtained by considering the subsurface vertical movements measured by the extensometer installed in BF-3 (1.5 m away from the trench).

Figure 6 shows the subsurface vertical movements recorded by the extensometer in BF-3. During the

excavation, the measurements showed an increase in settlement at all levels as excavation continued, with a maximum settlement of 2 mm at ME3-5. After concreting, a small recovery of ground settlements was recorded by the uppermost two spider magnets, except at ME3-5, which recorded a substantial upward movement (heave) of 7.5 mm in the soft marine deposit. ME3-5 is 9 m below ground level, just above the spike of ground movement measured by the inclinometer in BF-7. The consistency between the inclinometer and magnetic extensometer readings suggests that these large local deformations in the two orthogonal directions adjacent to the trench might be due to the presence of a weak soil layer or an overbreak and loss of ground during excavation. All other spider magnets in the same borehole show an increase in settlement during concreting and that the settlement ceased after concreting.

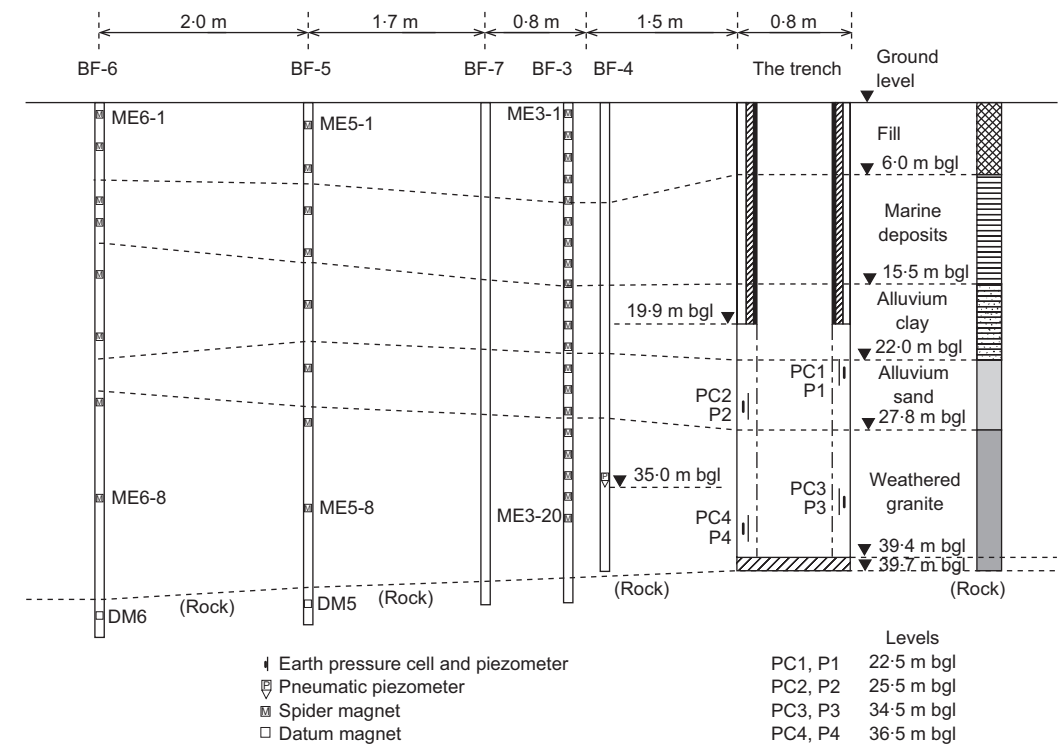


Fig. 4. Typical schematic cross-section A-A showing layout of instrumentation (not to scale)

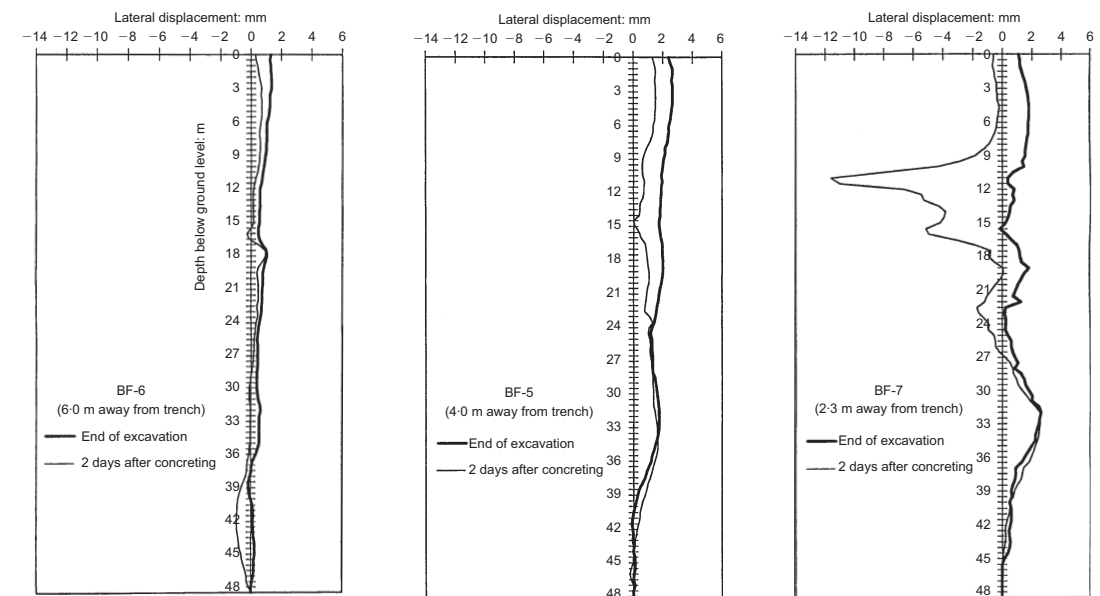


Fig. 5. Ground deformation profiles at different stages of barrette construction (positive lateral displacement: towards the trench; best resolution 0.1 mm deviation/1 m depth)

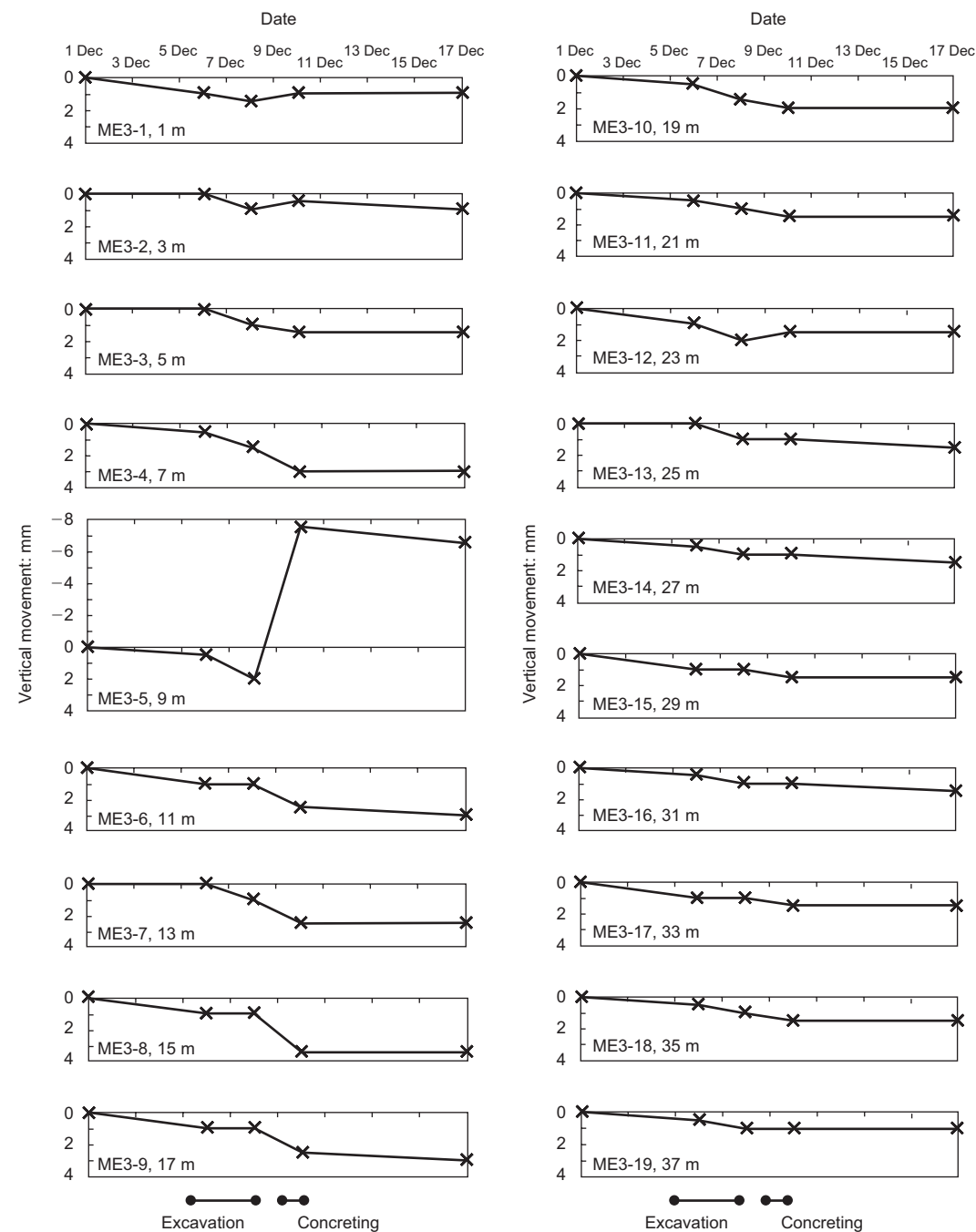


Fig. 6. Variations of subsurface vertical movement with time at BF-3 (1.5 m away from trench) (measured by magnetic extensometer: positive, settlement; negative, heave)

Figure 7 summarizes the subsurface vertical movements measured by the upper magnets installed in both BF-5 and BF-6. The excavation of the trench caused maximum downward movements

of 1.5 mm and 2.5 mm, at 2 m depth in BF-5 and at 1 m depth BF-6, respectively. Generally, the deeper the magnet, the smaller the settlement recorded. Recovery of ground loss due to concret-

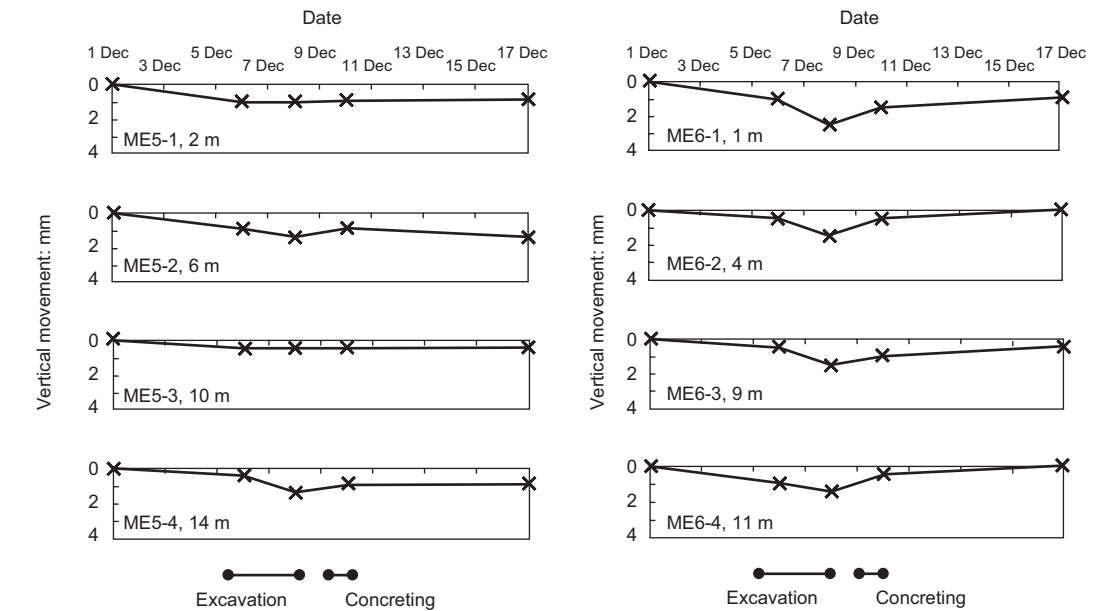


Fig. 7. Variations of subsurface vertical movement with time at BF-5 and BF-6 (measured by magnetic extensometer)

ing resulted in a substantial reversal of settlement in each borehole. This recovery of ground loss indicates that the lateral stress in the ground could not possibly be larger than the concrete pressure during construction. Low initial lateral stress in the ground can thus be deduced.

Surface ground settlements were monitored using ordinary levelling techniques. Even allowing for the typical accuracy of ± 1.0 mm of the levelling instrument, the observed settlements at various distances from the trench are unexpectedly very small. The maximum settlement measured was 1 mm during the excavation of the trench. During concreting, no recovery of ground loss can be identified.

CONTACT PRESSURES AT THE SOIL-WALL INTERFACE

Four vibrating-wire-total-earth-pressure cells and piezometers were attached to appropriate locations of the reinforcement cage during the construction of the barrette. Once in position, the instruments were jacked horizontally from the ground surface to ensure contact with the surrounding soil. The prime objective of installing the piezometers was to record changes of pore water pressures during the proposed vertical-load test of the barrette a few weeks after construction. In order to prevent the ceramic tips of the piezometers from clogging with bentonite, the ceramic tips were plugged with solid soap. This was expected to take a few days to

dissolve before allowing the piezometers to function properly after concreting.

Initial readings of the piezometers and earth pressure cells were taken before the instruments were jacked into position. This allowed a comparison to be made with the calculated bentonite pressures, using a measured unit weight (γ_b) of 10.8 kN/m^3 . There was very good agreement between the calculated bentonite pressures and the readings recorded by the vibrating-wire earth pressure cells (Fig. 8). The maximum difference between the calculated and measured pressures was less than 10 kPa. Some minor adjustments were made to the calibration factors.

Some piezometers showed higher pressures than the calculated values (Fig. 9). This was possible because the solid soap used to plug the ceramic tips of the piezometers had little time to dissolve. After taking initial readings, the earth pressure cells and piezometers were bedded in by jacking them out horizontally against the excavated soil surface until cell readings equal to the assumed initial $K_0 (=0.5)$ earth pressure were achieved. The jacking pressure was reduced once the concrete level went a few metres above the location of each pressure cell.

Since the initial horizontal stresses in the ground are not known for certain at Kowloon Bay, an initial K_0 value, equal to $(1 - \sin \phi')$, was assumed for each soil layer at Kowloon Bay, and the calculated lateral earth pressures are shown in Fig. 8. Low initial K_0 values in fill and decom-

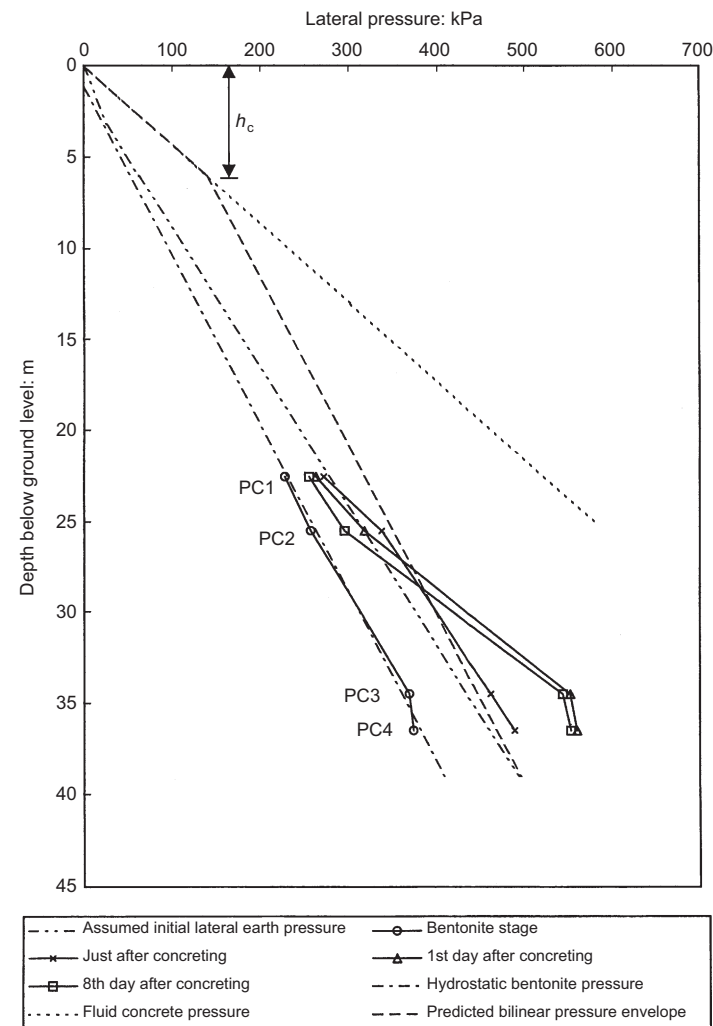


Fig. 8. Variations of lateral pressure distribution with depth

posed granite have recently been verified by back-analysing a deep excavation using the non-linear Simpson's brick model (Malone *et al.*, 1997). It was thus expected that there could be a stress reduction during the excavation of the barrette. For equilibrium, the initial total earth pressure had to reduce to the bentonite pressure. The reduction of the total initial stress in the ground due to excavation resulted in mainly horizontal ground movements. Swelling and softening of the soils followed and hence led to a decrease in shear strength and stiffness.

On the basis of field observations and theoretical considerations, Ng (1992) and Lings *et al.* (1994) proposed a theoretical bilinear pressure envelope for predicting lateral pressures developed at the soil-wall interface during concreting in a dia-

phragm wall panel. The theoretical bilinear equation derived is as follows:

$$\sigma_h = \begin{cases} \gamma_c z & z \leq h_c \\ (\gamma_c - \gamma_b)h_c + \gamma_b z & z > h_c \end{cases} \quad (1)$$

where σ_h , z and h_c are the total lateral pressure, the depth below the top of the panel and the critical depth, respectively. According to the guidelines given in CIRIA Report 108 (Clear & Harrison, 1985), the value of the critical depth is mainly governed by the type of cement used, the rate of concreting, the temperature and the size and shape of the trench. The critical depth calculated for the panel at Kowloon Bay is 6.03 m and the predicted bilinear envelope is shown in Fig. 8. The measured values just after concreting agree well with the

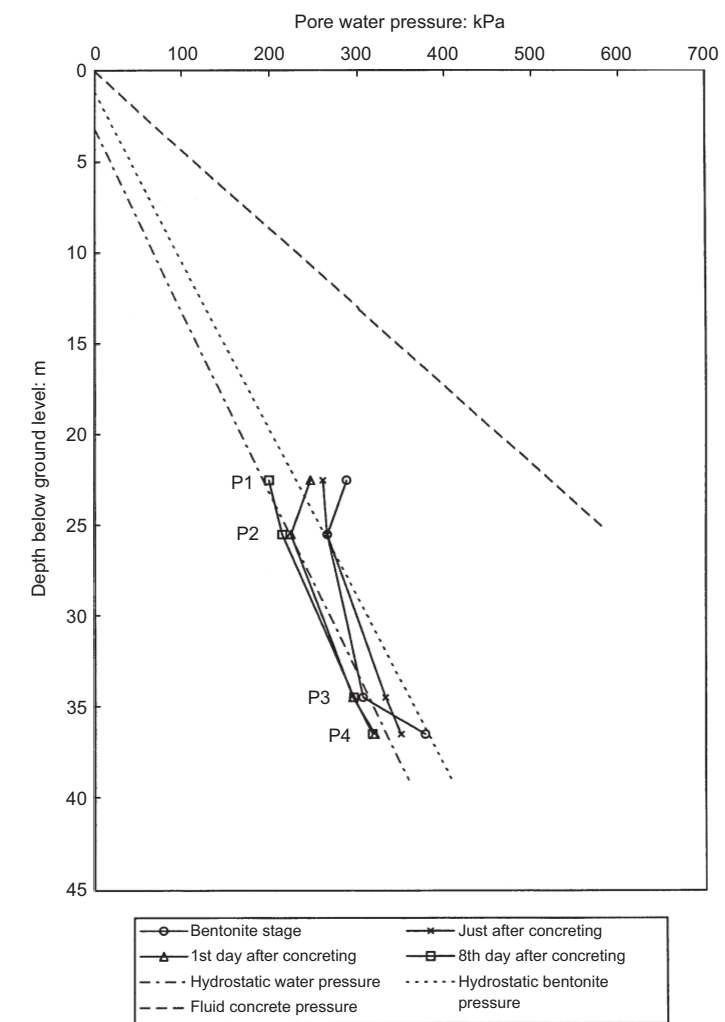


Fig. 9. Variations of pore water pressure distribution with depth

theoretical line predicted by the equation, except at PC1. It is clear that the full fluid concrete pressure did not develop over the full depth of the wall during concreting. The horizontal total pressures increased to some values higher than the assumed initial K_0 pressures, except at PC1, and they pushed the surrounding soil away from the trench, as shown in Fig. 5.

Measurements of lateral earth pressures 1 and 8 days after concreting are also shown in Fig. 8. There were substantial increases in lateral pressure at PC3 and PC4 in the weathered granite, but slight decreases at PC1 and PC2 in the alluvium sand. The increase of pressure in the weathered granite is somewhat unusual and might be due to swelling of the soil and stress redistribution.

Figure 9 shows the observed pore water pres-

sures at the soil-wall interface. As discussed previously, the measured values at the bentonite stage do not fall on the hydrostatic bentonite pressure line, probably because the ceramic tips were plugged with soap initially. Readings taken during and one day after concreting show that excess pore water pressures were generated because of concreting. Dissipation of the excess pore water pressure seemed to be complete 8 days after concreting. The pore water pressures at the soil-wall interface resemble hydrostatic conditions.

Figure 10 shows the measured pore water pressures 1.5 m away from the face of the trench in BF-4 (at 35 m below ground level). The piezometer recorded an increase of 7 kPa above an average pore water pressure of 311 kPa during concreting. The excess pore water pressure largely dissipated

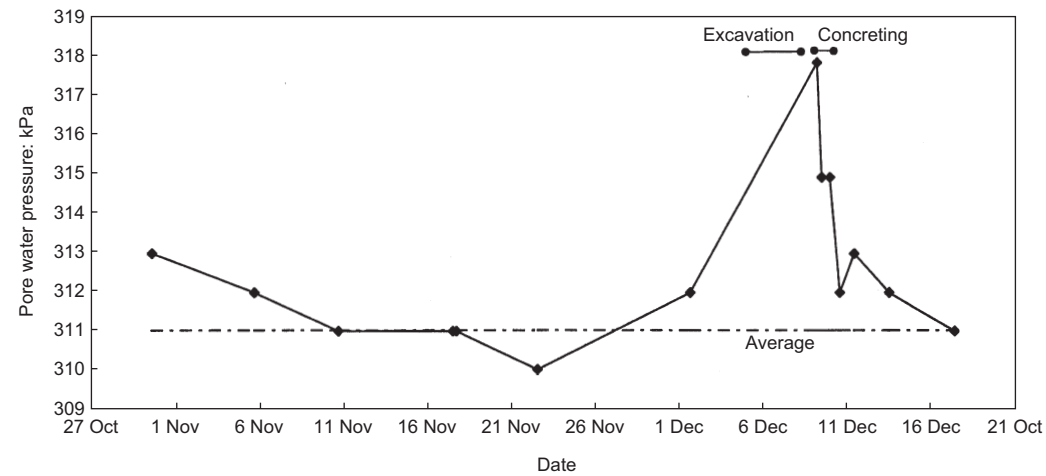


Fig. 10. Variations of pore water pressure with time at BF-4 (1.5 m away from trench) (measured by pneumatic piezometer at -35 mbgl)

within 2 days after concreting, indicating a high permeability of the weathered granite. The rate of pore pressure dissipation is consistent with the case history reported by Stroud & Sweeney (1977).

THREE-DIMENSIONAL MODELLING OF THE TRENCH EXCAVATION

Soil model, parameters and modelling procedures

To model the three-dimensional installation processes of the diaphragm wall panel construction, the finite-difference program FLAC3D (Itasca, 1996) was adopted. Since the three-dimensional soil-structure interaction of diaphragm walling is rather complex, it was decided to choose a relatively simple soil model for ease of interpretation of the computed results. All the soils at Kowloon Bay have been modelled as simple linear elastic and perfectly plastic isotropic materials with a Mohr-Coulomb yield surface. The elastic shear modulus adopted for each soil layer was based on the measured velocity of shear waves (geophysical method) at the same site, from which the maximum shear stiffness at very small strains was determined (Ng *et al.*, 1999). The model parameters are summarized in Fig. 11.

To estimate the shear stiffness at moderate shear strains (0.1%) for each soil layer, field-measured shear moduli of the weathered granite obtained from a self-boring pressuremeter (SBPM) were compared with the measured values obtained by the geophysical method. It was found that the elastic moduli of the weathered granite at very small strains obtained by the geophysical method were approximately three times higher than the stiffness at moderate strains measured by the

SBPM (Ng *et al.*, 1999). An assumption was thus made that the shear moduli at moderate shear strains in other soil strata would also be three times smaller than the elastic moduli obtained using the geophysical method. In this paper, two three-dimensional analyses are described: one uses the small-strain elastic moduli obtained by the geophysical method; the other adopts the deduced shear moduli at moderate strains. The shear strength parameters are taken from published data available in the literature (Cowland & Thorley, 1984).

For comparing the maximum observed ground deformations, only the excavation of the diaphragm wall trench was simulated. This was done by removing model soil elements inside the trench and applying a normal hydrostatic bentonite pressure on the trench faces simultaneously.

Comparisons between measurements and computed results

Figures 12 and 13 compare the measured and computed horizontal deformation profiles and vertical subsurface movements, respectively at various distances from the trench. It can be seen that the accuracy of the magnetic extensometers was generally better than that of the inclinometers. If the elastic moduli obtained from the geophysical method are used, the numerical simulation significantly underpredicts the actual ground deformations, especially for the vertical subsurface movements. This implies that the actual ground response substantially deviated from the elastic behaviour assumed in the three-dimensional analysis. Substantial plastic strains seem to have been induced during the excavation of the trench.

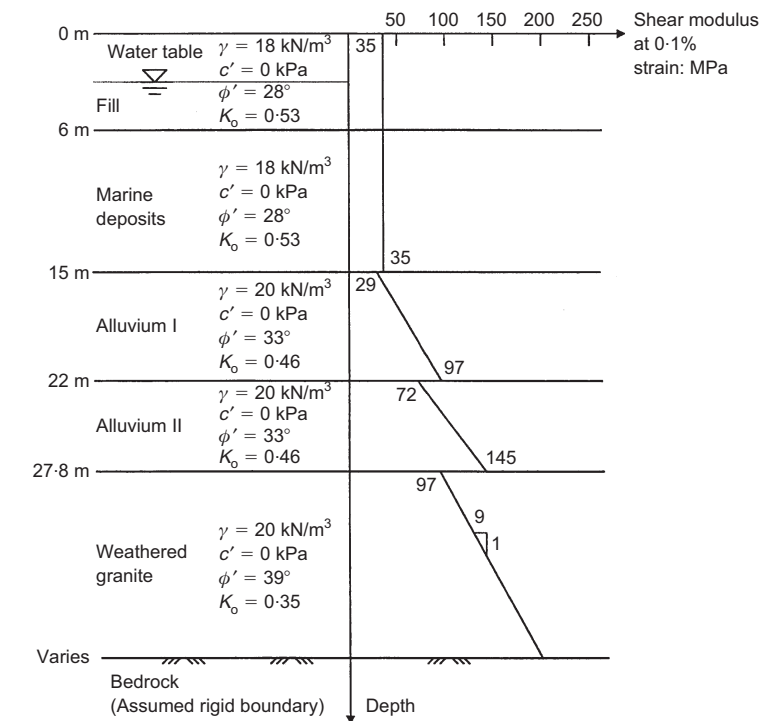


Fig. 11. Summary of soil parameters

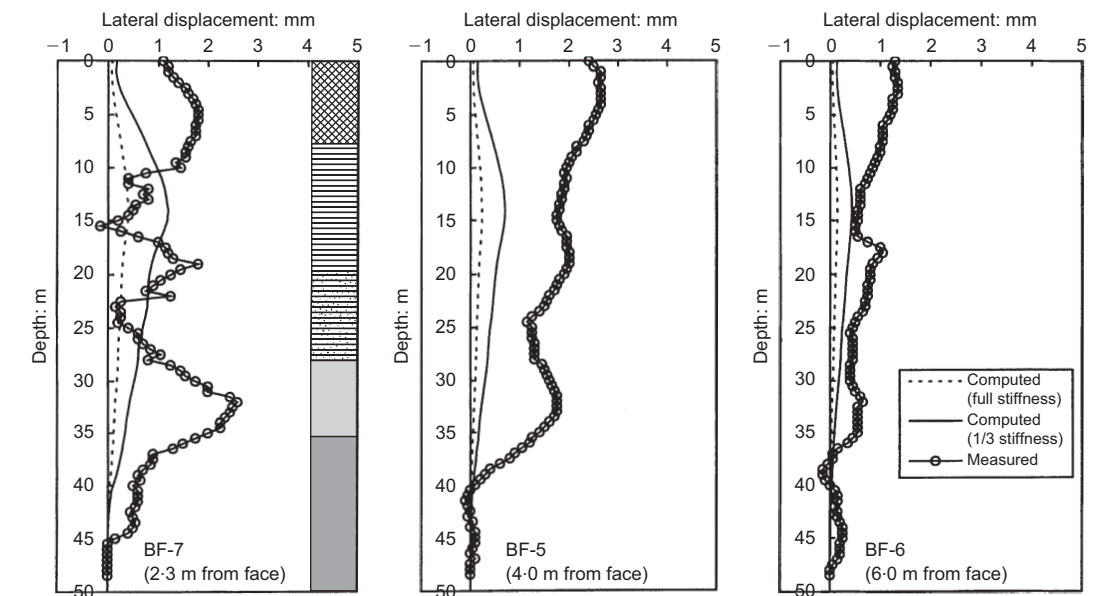


Fig. 12. Comparison between measured and computed horizontal deformation profiles after excavation (positive lateral displacements towards the trench)

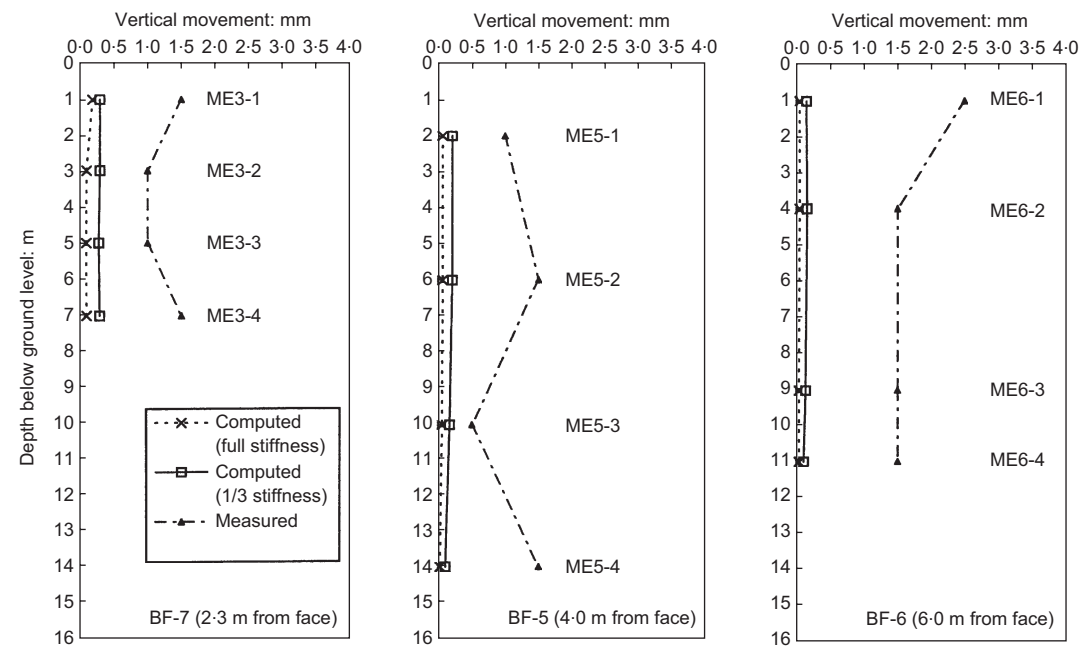


Fig. 13. Comparison between measured upper four magnets and computed subsurface vertical deformations after excavation

On the other hand, if all the soils are assumed to have operated at moderate shear strains (0.1%) during the excavation, the discrepancies between the computed and measured horizontal deformations generally become smaller. However, the discrepancy between the measured and computed vertical movements is still substantial. This discrepancy may be attributed to inappropriate soil parameters or the model used, or both. As an isotropic model was adopted in the analysis, the different responses in the two orthogonal directions seem to suggest that the soils exhibited a certain degree of anisotropy.

The large discrepancies between the measured and computed deformations using the shear moduli at moderate shear strains (0.1%) may be attributed to the presence of the 30 m thick soft, layered strata (i.e. fill, marine deposit, alluvium clay and sand) above the decomposed granite. The stiffness of these soft strata is likely to be considerably less than the assumed moduli adopted in the analysis, possibly owing to the onset of substantial plastic yielding. This would result in a significant reduction of soil stiffness and lead to larger ground movements during excavation. Of course, larger ground deformations would have been computed if a degradation of soil stiffness with increasing strain was allowed in the analysis. According to the comparisons between the measured and computed results, an average shear strain well in excess of

0.1% was mobilized around the trench during the excavation.

No further analyses have been attempted, owing to the limited accuracy of the inclinometers and the unavailability of good-quality soil stiffness parameters (small-strain shear moduli) for any of the soils except the weathered granites.

CONCLUSIONS

The construction in Hong Kong of an excavated large, rectangular-section barrette (i.e. a short diaphragm wall panel) in weathered and sedimentary soils under bentonite has been heavily instrumented and closely monitored. The size of the panel was 2.8 m long by 0.8 m wide by 40 m deep. During excavation, the maximum horizontal ground movements recorded were of the order of a few millimetres, with negligible surface settlements around the panel. A small amount of recovery of the horizontal ground movement was measured during concreting. The observed ground deformations are substantially smaller than the measured values obtained during the construction of a longer panel (6.1 m long by 1.23 m wide in plan) excavated on a site with similar ground conditions.

On the basis of three-dimensional numerical simulations of the excavation of the trench, an average mobilized shear strain greater than 0.1% around the excavated trench can be deduced.

At the soil-wall interface, the initial lateral earth pressures decreased to the hydrostatic bentonite pressures during excavation and then increased above the assumed initial K_0 pressures after concreting. The measured lateral pressures just after concreting show some agreement with a pressure distribution based on a theoretical bilinear pressure envelope.

Excess pore water pressures at the soil-wall interface and around the panel were recorded during construction. Dissipation of the excess pore water pressures seems to have been rapid and to have been completed within a few days.

ACKNOWLEDGEMENTS

This research project is supported by a research grant (HIA96/97.EG03) from the Hong Kong University of Science and Technology and a research grant (CRC96/99.EG04) from the Research Grant Council of Hong Kong. The authors would like to acknowledge the contribution provided by Paul Y. Foundation Ltd, who constructed and tested the heavily instrumented barrette. Other sponsors of this test barrette include the Geotechnical Engineering Office of the Hong Kong Government, Fong On Construction Ltd, Mass Transit Railway Corporation and Geotechnical Instruments Ltd. Technical input and support from Professors C. K. Shen and Wilson Tang of the Hong Kong University of Science and Technology and Messrs Martin Pratt and David Ng of Bachy Soletanche Group are highly appreciated.

REFERENCES

- Clear, C. A. & Harrison, T. A. (1985). *Concrete pressure on formwork*. Report 108. London: CIRIA.
- Clough, G. W. & O'Rourke, T. D. (1990). Construction induced movements of *in-situ* walls. In *Design and performance of an earth retaining structure*, Geotechnical Special Publication 25, pp. 439-470. New York: American Society of Civil Engineers.
- Cowland, J. W. & Thorley, C. B. B. (1984). Ground and building settlement associated with adjacent slurry trench excavation. *Proceedings of the international*

conference on ground movements and structures, pp. 723-738.

- Farmer, I. W. & Attewell, P. B. (1973). Ground movements caused by a bentonite-supported excavation in London Clay. *Geotechnique*, **23**, No. 4, 577-581.
- Geotechnical Engineering Office (1993). *Guide to retaining wall design*. 2nd edn. Hong Kong: Geotechnical Engineering Office, Civil Engineering Department.
- Itasca (1996). *Fast Lagrangian Analysis of Continua (FLAC-3D)*, version 1.1, user's manuals. Itasca Consulting Group, Inc., Minnesota.
- Lings, M. L., Ng, C. W. W. & Nash, D. F. T. (1994). The pressure of wet concrete in diaphragm wall panels cast under bentonite. *Proc. Instn Civ. Engrs, Geotech. Engng*, **107**, 163-172.
- Malone, A., Ng, C. W. W. & Pappin, J. (1997). Country report (invited): collapses and displacements of deep excavations in Hong Kong. *30th year Anniversary Symposium of the Southeast Asian Geotechnical Society*, Bangkok, pp. 5-124-5-129.
- Ng, C. W. W. (1992). *An evaluation of soil-structure interaction associated with a multi-propped excavation*. PhD thesis, University of Bristol.
- Ng, C. W. W., Ling, M. L., Simpson, B. & Nash, D. F. T. (1995). An approximate analysis of the three-dimensional effects of diaphragm wall installation. *Geotechnique*, **45**, No. 3, 497-507.
- Ng, C. W. W., Pun, W. K. & Pang, P. L. R. Small strain stiffness of natural granitic saprolites in Hong Kong. *J. Geotech. Geoenv. Engng. ASCE* (in press).
- Powrie, W. & Kantartzi, C. (1996). Ground response during diaphragm wall installation in clay: centrifuge model tests. *Geotechnique*, **46**, No. 4, 725-739.
- Shen, C. K., Ng, C. W. W., Tang, W. H. & Rigby, D. (1998). Invited discussion paper: testing a friction barrette in decomposed granite in Hong Kong. *Proc. 14th Int. Conf. Soil Mech. Found. Engng, Hamburg*, vol. 4, 2325-2328.
- Strange, P. J. (1990). The classification of granitic rocks in Hong Kong and their sequence of emplacement in Sha Tin, Kowloon and Hong Kong Island. *Geo. Soc. Hong Kong Newslett.*, **8**, Part 1, 18-27.
- Stroud, M. A. & Sweeney, D. J. (1977). Discussion appendix. In *A review of diaphragm walls*, pp. 142-148. London: Institution of Civil Engineers.
- Symons, I. F. & Carder, D. R. (1993). Stress changes in stiff clay caused by the installation of embedded retaining walls. In *Retaining structures*, (ed. C. Clayton), pp. 227-236. London: Thomas Telford.

FIELD STUDIES OF WELL-INSTRUMENTED BARRETTE IN HONG KONG

By Charles W. W. Ng,¹ Member, ASCE, Douglas B. Rigby,² Member, ASCE, Sean W. L. Ng,³ and G. H. Lei⁴

ABSTRACT: A large excavated rectangular pile (barrette) with lateral earth pressure and pore-water pressure cells was successfully constructed and tested in a sequence of marine, alluvial, and weathered granite soils. A "soft" base formed beneath the bottom of the barrette permitted over 100 mm of vertical settlement, completely mobilizing the shaft friction at the barrette-soil interface. During the vertical load tests, an unusual and complex response of pore-water pressures and earth pressures at the barrette-soil interface was measured. During each vertical loading cycle (except the last one) and before interface slippage of the barrette occurred, excess positive pore-water pressures were recorded in all soil layers. Upon the initiation of slip at the barrette-soil interface, a sudden drop in the measured pore pressures as well as a substantial drop in lateral earth pressures generally resulted. Subsequent loading or unloading slippage events did not show the same dramatic behavior unless a period of consolidation/recovery was allowed first. This implies that caution must be used in design of barrettes relying heavily on skin friction when shearing induces contractive soil behavior. The current test results indicated that the empirical uncorrected SPT-N value approach and the effective stress β -method were inconsistent.

INTRODUCTION

Limited space and high demand have made land in Hong Kong extremely expensive. Tall buildings are built to optimize the floor area to land area ratio. Many of the tall buildings located along the Victoria Harbor on the Hong Kong Island and the Kowloon peninsula are commonly founded on reclaimed land. Thus deep foundations are required to resist both vertical and horizontal loads due to the weight of the building and wind, respectively. The prevailing deep foundation types for tall buildings on these reclaimed lands are large bored and excavated piles, which are very long, normally in excess of 50 m. These piles can be circular (bored piles/drilled shafts) or rectangular (barrette) in shape and must extend through the fill, underlying soft marine clay, sandy clay, and alluvial sand deposit down into the deep weathered granite soil (saprolite), which is typically less weathered with an increase in depth. The thickness of the weathered granite can be up to 80 m in some places, and its depth can extend to more than 100 m from the ground surface.

Over the last 15 years, barrette foundations have become increasingly popular in parts of Asia such as Hong Kong and Malaysia for many civil engineering structures and tall buildings. The construction method for barrettes is very similar to that adopted for diaphragm walls, where a rectangular trench is excavated under bentonite by heavy grabs or hydrofraise and filled with tremie concrete. In Hong Kong, single barrettes up to a size of 1.5 m wide \times 6.6 m long (on plan) have been constructed (Pratt and Sims 1990). Due to their rectangular shape, barrette foundations are particularly suitable to resist large vertical and significant horizontal loads in a chosen direction.

For deep rectangular piles, the current design procedures adopted in Hong Kong are relatively conservative, and they

assume a heavy reliance on end-bearing resistance of bedrock in many instances. Without performing at least one full-scale pile load test on site, skin friction in excess of 10 kPa is not permitted normally by the regulations. In some areas, however, bedrock is found at depths of over 100 m. Under such circumstances, excavation of deep foundations to bedrock becomes difficult, time consuming, and expensive. Exceeding the nominal permitted skin friction requires costly and time-consuming full-scale pile tests to verify design values of skin friction. Many Hong Kong engineers would welcome improved design guidelines based on more rational design approaches that would allow for higher default values of skin friction along a pile to be used, or a reduction in the number of verification piles in similar site conditions.

The problem is that estimation of skin friction development along a long barrette (between 40 and 100 m) is a very difficult task. The method of construction, workmanship, rheological properties of the slurry, and concrete placement affect its behavior. Any attempt to increase the design skin friction value must be done with caution. A task force has recently been formed, with participants from the government, some contractors and consultants, and the Hong Kong University of Science and Technology, to carefully study this problem aiming at the development of a more reasonable design guideline for deep pile foundations in Hong Kong. Currently a university-led and industry-supported three-year research project is under way to study skin friction on barrettes founded in weathered granites in Hong Kong by full-scale pile testing, laboratory tests, numerical and centrifuge modeling, and reliability analysis (Shen et al. 1997). Initially, two piling test sites are investigated: one at Kowloon Bay and the other in the Central district. In this paper, the construction of a 2.8 m long by 0.8 m wide and 39.7 m deep barrette at Kowloon Bay, its vertical load-deflection characteristics, and its pore-water pressure and lateral stress changes at the soil/barrette interface are reported and discussed. In addition, the measured skin friction is compared with other test results in Hong Kong.

SITE LOCATION AND GROUND CONDITIONS

The test site is located on the Kowloon peninsula of Hong Kong, to the east of a runway of the old Kai Tak international airport, at the Kowloon Bay area (Fig. 1). Fig. 2 shows the geology and some relevant borehole information obtained at Kowloon Bay. The site is on marine reclaimed land and the ground level is at approximately 4.48 m above Principal Datum (PD). The ground-water level is about 3 m below ground surface. The ground conditions consist of about 6.0 m fill ma-

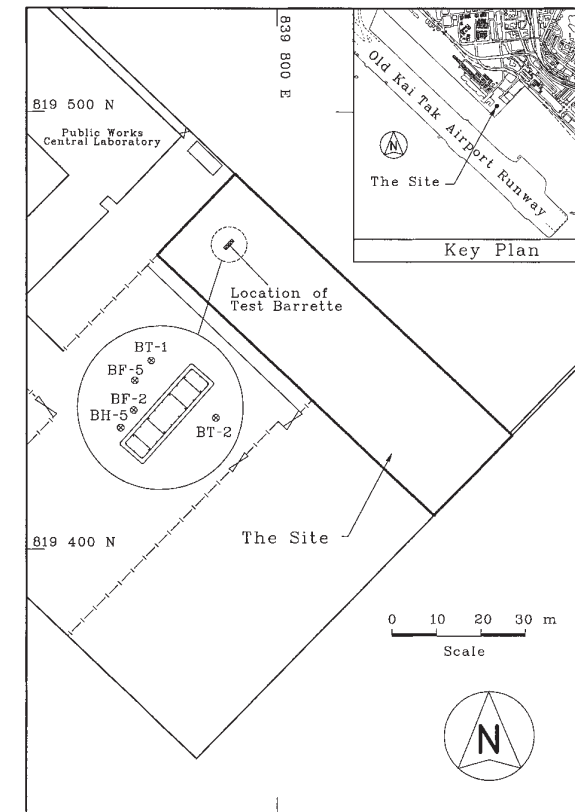


FIG. 1. Location of Test Barrette at Kowloon Bay, Hong Kong

terial overlying a succession of approximately 9.5 m marine clay deposits, 7.5 m of sandy clay (probably alluvial), 4.8 m alluvial sand of Quaternary age, and about 12 m of weathered granitic saprolites that overlie granitic rocks of Upper Jurassic to Lower Cretaceous age (Strange 1990). Detailed descriptions and measured N-values by Standard Penetration Tests (SPT) for each type of materials are given in Fig. 2. It can be seen that scattered SPT-N values were obtained in both alluvial sand and weathered granite. The former shows a decreasing N-values with depth, whereas the latter illustrates an opposite trend. Based on results of drained triaxial compression tests on weathered granites, effective cohesion and angle of friction were found to be 0 kPa and 39°, respectively. Typical Atterberg limits for the sandy clay are 40, 20, and 20 for the LL, PL, and PI, respectively (GEO 1996a).

Strictly speaking, the site is not ideal for studying skin friction of excavated piles in weathered granite as the thickness of the granite is relatively thin and the measured SPT-N values are relatively low. However, due to the limited availability of land in Hong Kong for purely research purposes and the time restraints, this existing government test site was chosen. A distinct advantage is that the site investigation records are very comprehensive as this site has been a test site for the Geotechnical Engineering Office of the Hong Kong Special Administrative Region over the years. Various in situ and laboratory tests (Ng et al., unpublished paper, 1999) have been carried out on this site, resulting in ground conditions that are well known.

DETAILS OF CONSTRUCTION

The test barrette or the diaphragm wall trench was excavated using a traditional cable-operated grab. The size of the excavated trench was 2.8 by 0.8 m on plane and 39.7 m deep (Figs. 2 and 3). During construction, a concrete guide wall was first placed, and at deeper levels the trench was supported

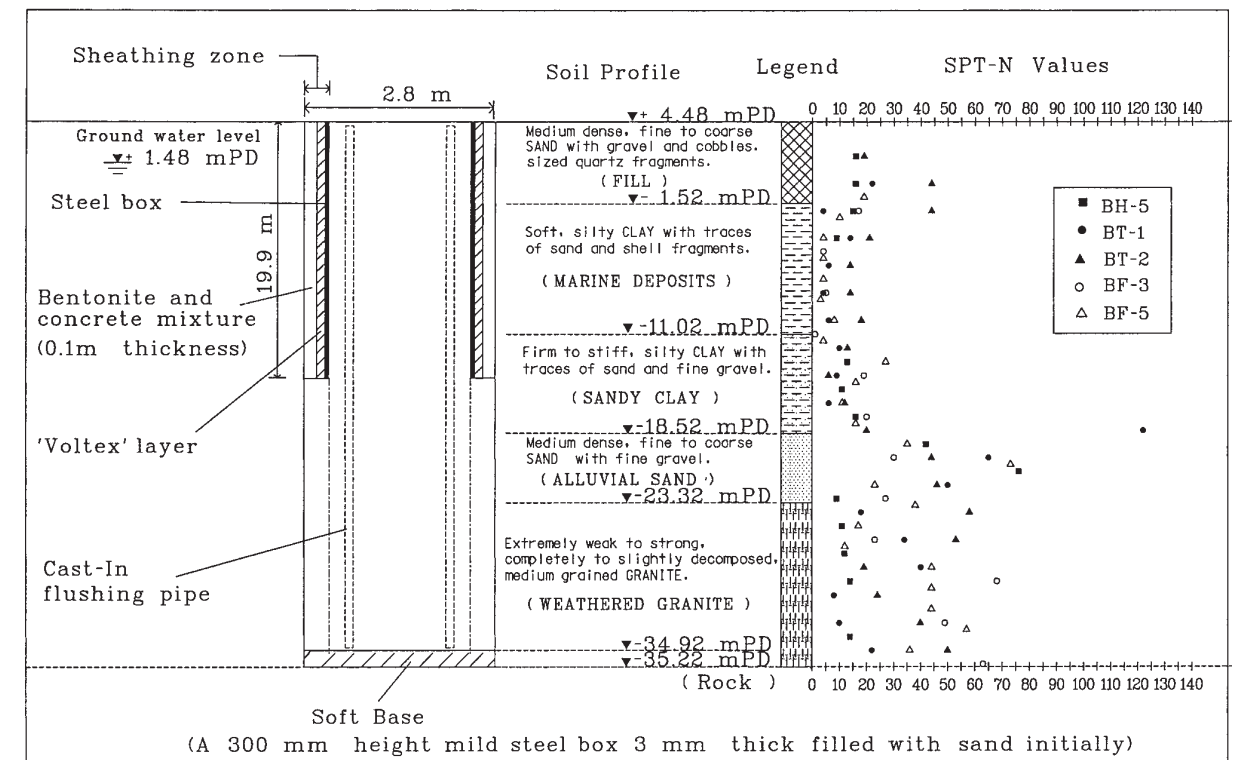


FIG. 2. Borehole Logs and SPT-N Values at Kowloon Bay, Hong Kong

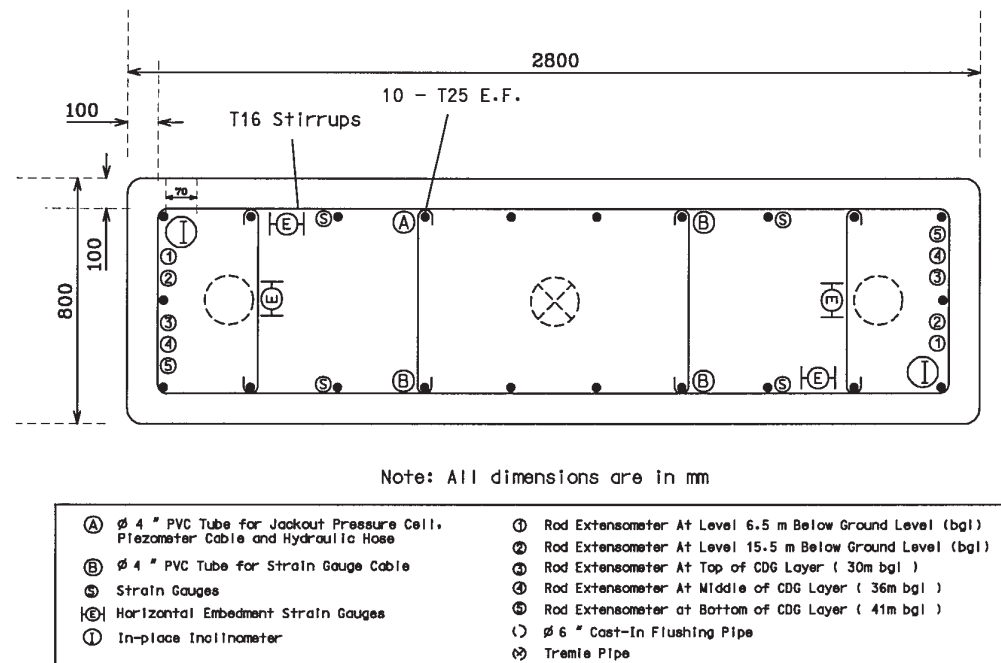


FIG. 3. Layout of Instrumentation (Plan View)

by bentonite with unit weight (γ_b) of about 10.8 kN/m³. Soil spoil, suspended in the bentonite slurry, was pumped to a desanding unit at the ground surface. After desanding, the bentonite was recharged into the trench. Chiseling of the base was carried out when rock was encountered at a more shallow depth than expected, about 39.6 m below ground. This caused a small overbreak at the base, which was detected by a sonic profiling system. The entire excavation took 62 h to complete and the final excavated depth was 39.7 m below ground. The rate of excavation could have been improved if a 24-h nonstop excavation schedule were followed, as is the normal practice for commercial test barrettes in Hong Kong.

After completion of the excavation, three instrumented reinforcement cages were lowered one-by-one into the trench. Concreting was carried out 43 h after completion of the excavation. The average rate of concreting was 10.32 m/h by using a tremie pipe. The whole barrette trench was filled with concrete in 4.5 h. The Ordinary Portland Cement (OPC) concrete used was grade C30/20 with unit weight (γ_c) of 23.2 kN/m³. It had a water-to-cement ratio of 0.45 and an average slump of 180 mm. During concreting, the average temperature measured inside the trench was 27.6°C inside the slurry. The excavation and concreting procedures of the barrette, in fact, were identical to the construction of a typical diaphragm wall panel.

The top 20 m of the barrette consisted of a reduced-section sheathing zone (Fig. 2) built with the intention of minimizing the interface skin friction developed between the barrette and the upper soil layers. This sheathing layer consisted of four layers: a 3 mm steel plate welded onto the reinforcement cage, a coating of bitumen, a flexible and weak "voltex" layer (geotextile infilled with sodium bentonite), and a thin sheet of plywood. However, the final result was that the plywood was unfortunately attached to the steel plate with a dense matrix of high-strength screws, precluding the possibility of shear between the intermediate "soft" layers. As a consequence, the theoretical gap of about 80 mm between the plywood and the surrounding soil was not back-filled with gravel as planned, so that a "weak" friction zone would hopefully exist. However, steel rods inserted into this suspected bentonite-filled gap about 2 weeks after concreting were unable to probe beyond

a meter or two all round the barrette. Either concrete overflow had partially filled the gap, construction activities failed the soil infilling the gap, or surface materials mixed with solidified bentonite. Thus, in the end, the sheathing zone was not expected to function to effectively reduce skin friction over the top half of the barrette.

At the bottom of the barrette, a "soft" base was formed to minimize the effects of end-bearing for mobilizing full skin friction at the soil-wall interface. This was done by placing a 2.8 × 0.8 × 0.3 m in height steel box to the bottom of the trench, before the lowering of the main reinforcement cages. The box was made of 3 mm thick steel plate, and it was initially filled with fine round sand. Seven days after concreting, the sand-filled steel box was drilled through and flushed with pressurized water via two cast-in flushing pipes and one concrete core hole in the middle of the barrette (Fig. 3). Great care was taken to ensure that most of the sand was flushed out to form a "soft base" (i.e., void) underneath the barrette.

INSTRUMENTATION

To study the load transfer mechanism and load-settlement characteristics of the barrette constructed at Kowloon Bay, a substantial amount of instrumentation was installed. A summary of the instruments installed inside the barrette is given in Table 1. In addition, four sets of standard dial gauges together with surveying were used to monitor the vertical settlement of the top of the barrette and reference beams during testing.

Strain gauges were placed at 27 levels on the reinforcement cages (Figs. 3 and 4). Four surface mounted and four embedded strain gauges were placed alternatively at different levels

TABLE 1. Summary of Instrumentation at Kowloon Bay

Instrument (1)	Quantity (2)
Strain gauges	132
Rod extensometers	10
In-place inclinometers	2
Vibrating wire piezometers	4
Earth pressure cells	4

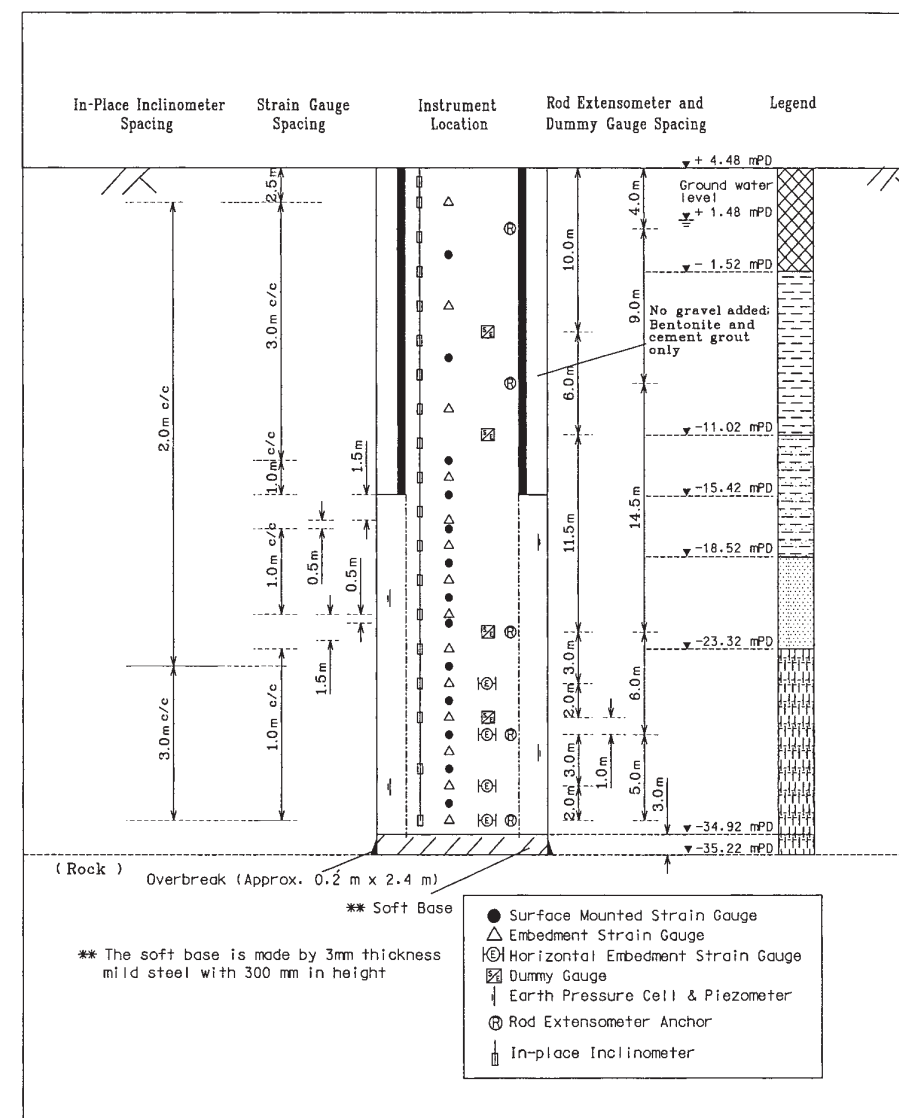


FIG. 4. Layout of Instrumentation (Elevation)

to measure vertical strains induced in the reinforcing bars and in concrete, respectively. Moreover, four levels of horizontally embedded strain gauges, with four gauges in each level, and four levels of dummy gauges (eight in total) were installed in the cage. The horizontally embedded strain gauges were used to determine any Poisson's ratio effects (results are not relevant to this paper). A total of 132 gauges, typically at 3 m and 1 m intervals in the sheathed and unshathed zones, respectively, were installed to determine the strain distributions along the entire depth. It was found that similar results were recorded by both the surface mounted and embedded strain gauges. Thus, no further distinctions between the two types of gauges are made in this paper.

Ten aluminum rod extensometers were sleeved individually in PVC tubes and installed to five depths at two different locations inside the barrette to monitor displacements between each depth and reference steel plate at the top of the barrette (Figs. 3 and 4). After the pile test it was found that although the extensometers reflected a reasonable pattern of elastic pile shortening and rebound during loading and unloading cycles, some of the relative magnitudes measured were clearly unreliable. This was likely caused by friction developed between the metal rods and the PVC tubes having a 12.5 mm outer

diameter and 12.6 mm inner diameter, respectively. Recently, extensometers consisting of 15 mm steel rods placed in 50 mm steel tubes filled with oil have given reliable results in Hong Kong.

A total of 38 biaxial servoaccelerometer sensors were installed at 19 levels (most of them at 2 m interval) in two cast-in pipes inside the barrette. The locations of the in-place inclinometers and the levels of sensors were indicated in Figs. 3 and 4, respectively. The bottoms of the inclinometers were socketed in rock. These two in-place inclinometers were designed to measure rotations and hence horizontal movements of the barrette during loading. From the measurements, it was concluded that no significant bending deflection of the barrette was induced during the vertical load tests.

A total of four vibrating wire total earth pressure cells, together with four vibrating wire piezometers, were installed at the barrette-soil interface at four levels within the layers of sandy clay, alluvial sand, and weathered granite. The depths of the earth pressure cells and piezometers are shown in Fig. 4. These total earth pressure cells and piezometers were attached to appropriate locations of the reinforcement cage during the construction of the barrette. Once in position, the instruments were jacked out horizontally to ensure contact at

reasonable pressures with the surrounding soil. Each vibrating wire piezometer was located about 80 mm above the corresponding pressure cell.

LOAD AND DISPLACEMENT BEHAVIOR OF PILE

The loading system for the test barrette consisted of two 1,000 ton hydraulic jacks pushing against kentledge formed from steel billets. The kentledge rested on two parallel sets of concrete blocks spaced 6 m apart, center to center. A pile cap at the top of the barrette and a steel spreader beam above the jacks were used to transfer the manually applied loads. The pile head displacement was measured by using four dial gauges symmetrically resting on two reference beams. Settlement of these reference beams was monitored by the conventional surveying technique.

The test program originally comprised four loading and unloading cycles (Fig. 5). However, after the applied load reached 7,455 kN at the second cycle, substantial settlement was recorded and the applied load could not be held constant within the prescribed maximum settlement tolerance of 0.05 mm/10 min. It was therefore decided to unload the barrette to 4,555 kN and to hold it for 80 h (about 3 days). After the holding period, the testing program resumed and two more loading cycles were performed. The barrette-soil interface appeared to gain strength as a result of consolidation, which is discussed later. Due to the presence of the "soft base" (i.e., void) underneath the barrette, the barrette ultimately settled about 100 mm, enabling the skin friction to be fully mobilized along the shaft.

Prior to calculating the distribution of axial load and shear stress along the length of the barrette, it is necessary to adopt appropriate values of Young's modulus for the barrette. Since the conditions of concrete curing inside the trench are very different from those in a standard curing tank in the laboratory, continuous concrete cores were taken from at the center along the depth of the barrette to determine the Young's modulus of the in situ concrete. The measured secant Young's modulus varying with depth (at about 1 m spacing) is shown in Fig. 6.

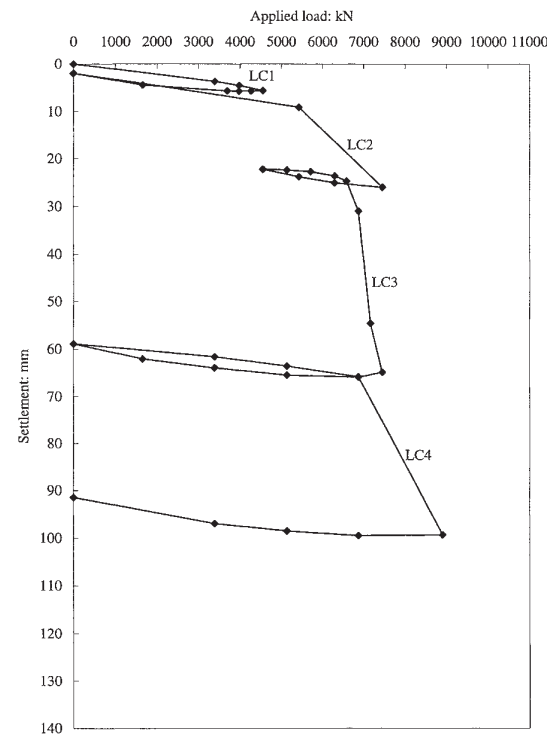


FIG. 5. Load-Settlement Response of Test Barrette

Although there is a general increase of Young's modulus with depth due to the natural compaction process of the concrete under its own weight, the measured data are fairly scattered. For accurately converting the measured strains in the barrette to stresses, the actual measured modulus at each tested depth and corrected for steel present was adopted in the calculations. Fig. 7 shows the deduced axial load versus depth for the

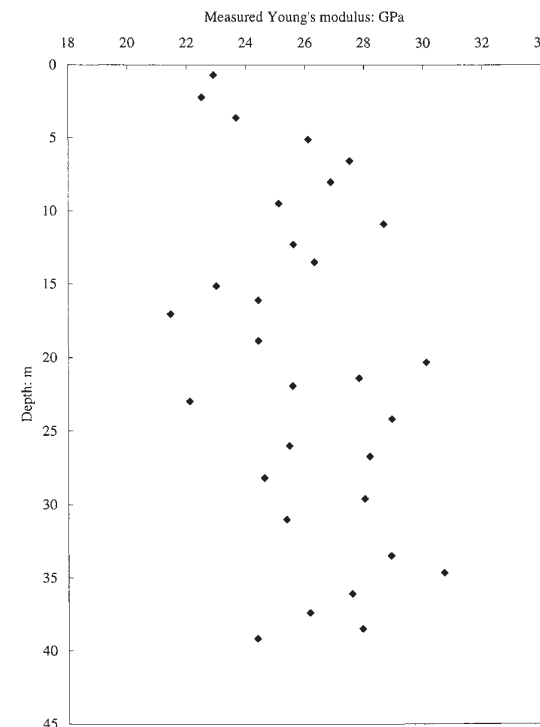


FIG. 6. Variation of Measured Young's Modulus of Concrete with Depth

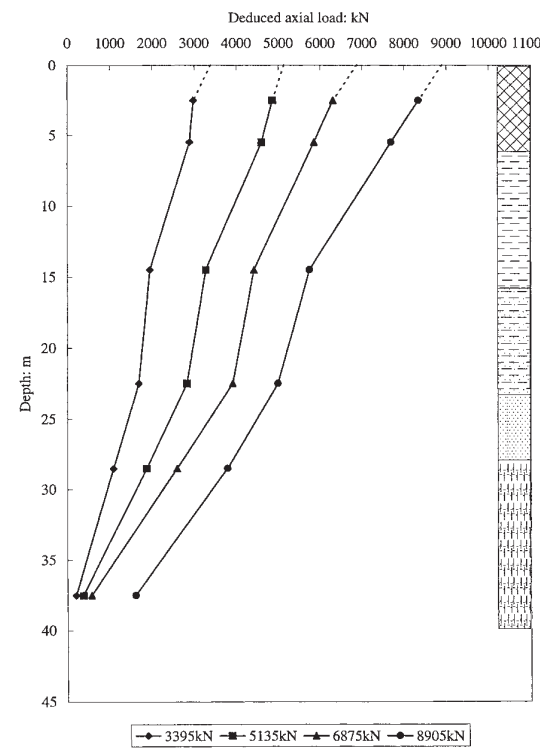


FIG. 7. Deduced Axial Load Distribution at Load Test Cycle 4

last loading cycle. An axial stress was calculated from the average measured strains at each level and the corresponding measured Young's moduli (Fig. 6) from concrete cores taken from the center of the barrette. From the calculated axial stress, the axial load with depth was then determined considering the local barrette cross-sectional area. It can be seen that the deduced axial load at the top of the barrette is consistent with the applied load recorded by the hydraulic jacks (shown as dotted lines). The load distribution along the depth shows features common to a typical friction barrette. Due to the presence of the "soft base," minimal base resistance was mobilized, except at the maximum load of 8,905 kN, where the base resistance increased substantially from 560 to 1,600 kN. This substantial increase was likely caused by the mobilization of some end bearing resistance due to the crushing of the 300 mm steel box underneath the barrette (possibly not all of the sand was flushed out from the box).

BARRETTE SKIN FRICTION

From the gradient of the barrette normal stresses with depth, mobilized skin friction (interface shear stress, τ) is calculated and plotted against deduced local displacement of the barrette in each soil stratum as shown in Fig. 8. Shear stress was fully mobilized in all soil strata when the displacement reached approximately 40 mm (or at 2.4% of the 1.7 m equivalent diameter of the barrette), after which the magnitude of shear stress remained essentially constant. Some peak strength behavior with softening at the interface was observed in the fill, sandy clay, and alluvial sand. The large skin friction mobilized in the fill material may possibly be attributed to the surcharge effects resulting from the dead weight of the concrete blocks supporting the kentledge load. On the other hand, no peak strength behavior could be identified at the barrette-weathered granite interface. Fig. 9 shows the distribution of mobilized skin friction with depth. Within the sheathed zone, a constant and substantial amount of shear stress was mobilized, apparently indicating that no "weak" zone existed around the sheathed barrette (except at depth below 15 m; see Fig. 7). The mobilized shear stress in the sandy clay was smallest, whereas the mobilized shear stresses in the fill, marine deposits, and weathered granite are in the same order of magnitude at the maximum applied load. Below the sheathed zone, the distribution of maximum mobilized shear stress follows the trend of the measured SPT-N values (Fig. 2). At the maximum applied load (8,905 kN), the mobilized skin friction of about 30 kPa was found for the fill, marine clay, alluvial sand, and weathered granite, and about 15 kPa for the sandy clay.

For comparing shear stress mobilized in similar soils at different construction sites, it is a common practice to normalize

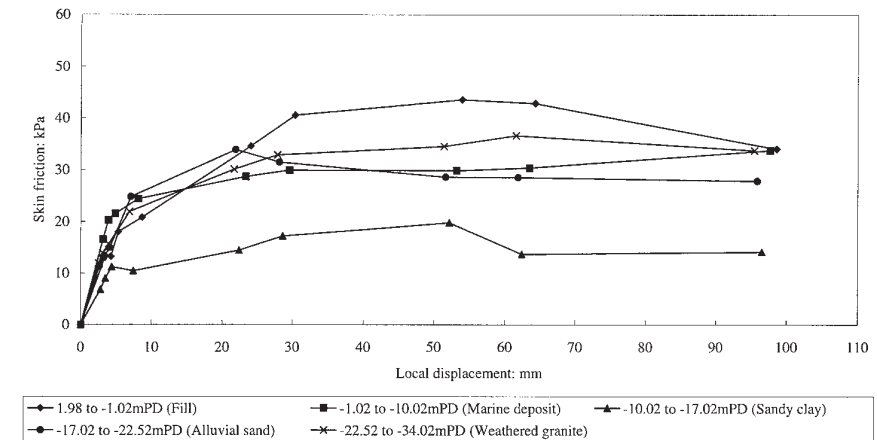


FIG. 8. Mobilization of Skin Friction with Local Displacement

the measured shear stress with an average uncorrected SPT-N value, i.e., τ/\bar{N} , (before construction) in Hong Kong. Fig. 10 shows the comparison between the normalized maximum shear stress measured at the current test site and at the International Trademart, which is about 1.4 km away in Kowloon Bay (Ho 1994). At the latter site, a 2.2 m by 0.8 m by 56.8 m deep barrette was also excavated by cable-operated grabs and founded in about 20 m thick layer of weathered granite, which has an average higher value of SPT-N value (typically ranging from 15 to 110) than the former site. For SPT-N values smaller than 35, the magnitude of measured skin friction is consistent between two sites. No comparison can be made between the measurements from the two sites for higher SPT-N values. However, the ranges of the values τ/\bar{N} obtained from the former and the latter sites are 0.9 to 2.9 and 1.3 to 2.3, respectively.

PORE PRESSURE RESPONSE AT SOIL/BARRETTE INTERFACE

After installation of the piezometers, readings were taken continuously to compare them with the initial hydrostatic pore-water pressures in the ground (the initial ground-water table was located at about 1.3 mPD). It was found that the measured pore-water pressure at gauge P1 at the sandy clay layer (Fig. 11) was slightly higher than the corresponding hydrostatic value (1.3 mPD) before the loading test. Piezometric level (head) is defined as the sum of the pore-water pressure head and the elevation head at each location. The measured piezometric heads recorded at P3 and P4 were a little lower than the hydrostatic conditions in the weathered granite before the commencement of the first to the fourth load cycles, respectively. Similarly, labels UC1–UC4 represent the start of the first to the fourth unloading cycles.

When the first loading cycle (LC1) was carried out, all piezometers responded positively to each increment of applied load [Fig. 11(b)], recording an ultimate increase of head of almost 3 m in the sandy clay (P1) and about 1 m in both the alluvial sand (P2) and weathered granite (P3 and P4). During the first unloading cycle (UC1), the pore pressure in the sandy clay and alluvial sand remained steady while a slight and gradual reduction of pore pressure was recorded at P3 and P4 in the weathered granite. Each loading and unloading increment is clearly confirmed by the pile shortening and rebound measurements from the rod extensometer data.

During loading cycle 2 (LC2), again increments of applied load resulted in increments of positive pore pressure until failure occurred. A further increase of approximately 6 m head of water was measured in the sandy clay, 2 m in the alluvial sand

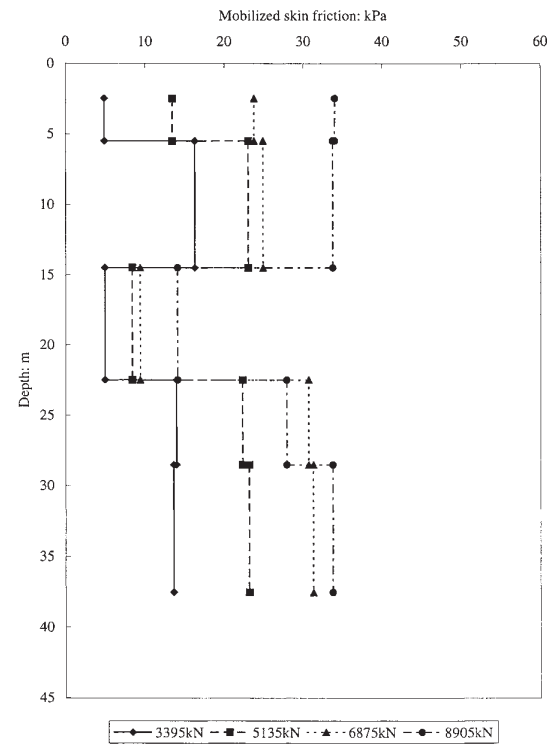


FIG. 9. Distribution of Mobilized Skin Friction (LC4)

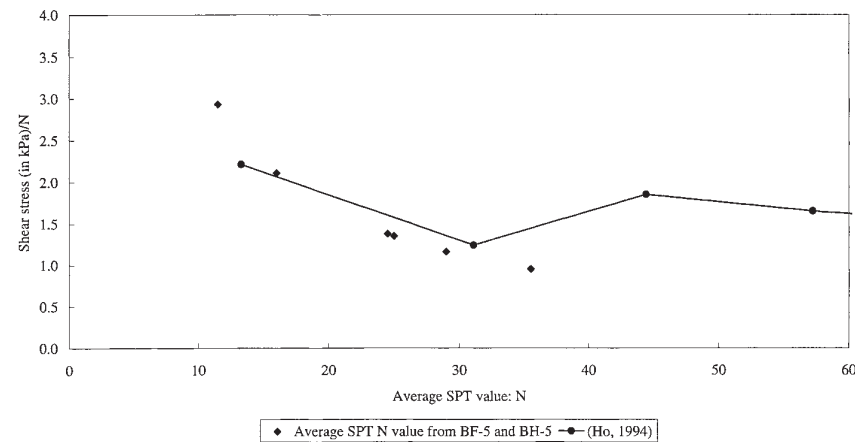


FIG. 10. Relationship between Normalized Maximum Shear Stress in Weathered Granite and Average SPT Value, N

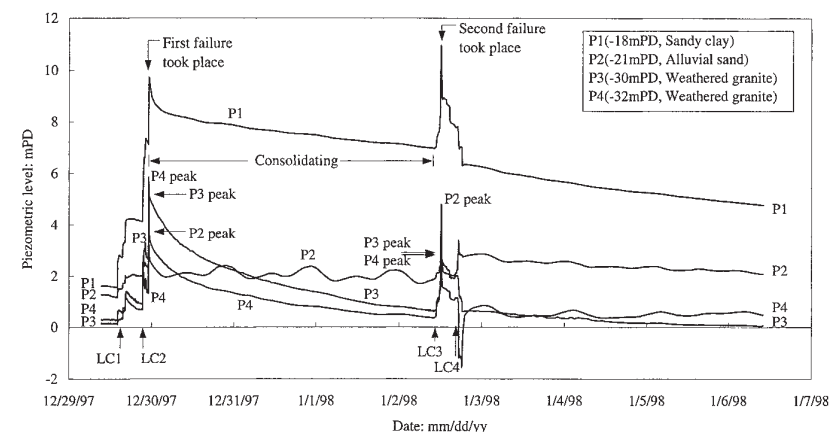


FIG. 11(a). Variations of Piezometric Level During Load Testing

and 4–5 m in the weathered granite, respectively. The minor drops in water pressure occur together with reduction in applied loading due to continued settlement of the pile. At failure the settlement rate of the barrette increased significantly and the settlement increased to about 25 mm (Fig. 5) and the pore pressures began to suddenly drop at the same time in all soil layers [after the loading slip shown in Fig. 11(b)]. Slip at the barrette-soil interface is inferred at failure since all rod extensometer data held constant, indicating that the entire barrette was moving downward as a rigid body (about 20 mm). After about 5 min of slippage, the load was reduced and then subsequently maintained for a holding period of 80 h. During this time the excess pore pressures dissipated almost completely in the weathered granite but only slightly in the sandy clay and, surprisingly, in the alluvial sand [Fig. 11(a)]. Also visible in this figure at P2 in the alluvial sand are measurements of tidal action. The shifted frequency and the attenuated relative magnitudes of the high and low tides correspond to actual tidal values from 12/30/97 to 1/2/98 (“Quarry” 1997, 1998) almost perfectly, indicating proper functioning of the P2 pore-water pressure gauge.

Pore pressure behavior during the third loading cycle (LC3) was very similar to cycle 2. Loading increments resulted in corresponding increases in all four piezometers; overall, the increase of excess pore water pressure amounted to about 4 m head in the sandy clay, 3 m in the alluvial sand, and 2.5 m head in the weathered granite [Fig. 11(c)]. Failure and slippage of about 40 mm occurred at approximately the same load (7,455 kN) as cycle 2, again accompanied by significant and sudden drops of pore pressure at all the piezometers (due to

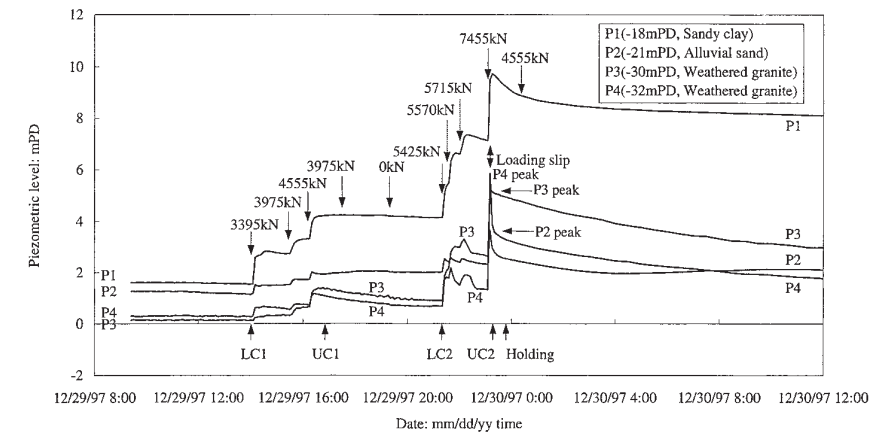


FIG. 11(b). Variations of Piezometric Level during First Two Load Test Cycles

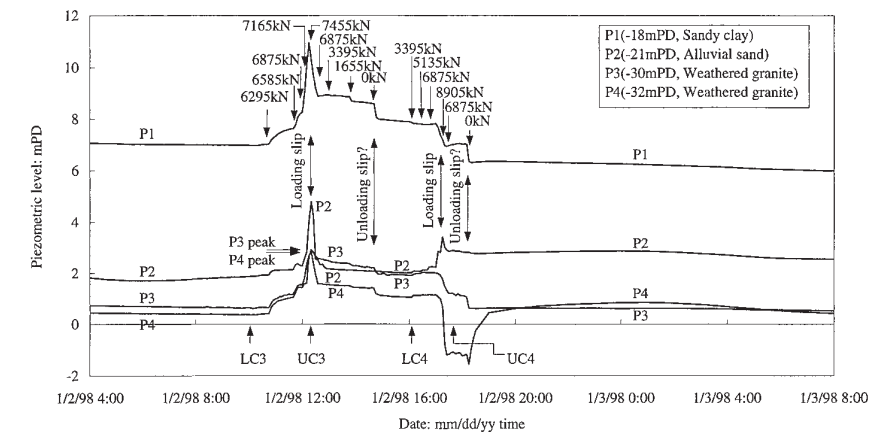


FIG. 11(c). Variations of Piezometric Level during Last Two Load Test Cycles

loading slip). During unloading (UC3) the measured pore pressures continued to drop slightly until another sudden drop of pore pressures was observed at the last unloading stage to 0 kN (except P2) which was most significant in the sandy clay.

Loading cycle 4 (LC4) varied from previous loading cycles since it occurred shortly after a barrette-soil interface failure. Increments of applied load in LC4 caused only slight increases of pore-water pressure in the alluvial sand and weathered granite while pore pressures remained essentially steady in the sandy clay [Fig. 11(c)]. As the load reached its maximum value of 8,905 kN (Fig. 5), failure occurred (about 30 mm of downward slippage), again resulting in substantial drops of pore-water pressures in all soil layers but the alluvial sand where an increase of water pressure followed by a drop was measured [Fig. 11(c)]. One piezometer in the weathered granite recorded a significant drop in pore pressure to a “negative” value, lower than the original in situ water pressure. Like UC3, water pressure values were steady until the last unloading step, when sudden changes in pore-water pressure resulted in all layers except the alluvial sand. Two of the piezometers recorded the standard drop in pore pressure, while the third “negative” reading piezometer showed a sharp increase back to a more reasonable value.

After the load test, dissipation of excess pore-water pressures continued [Fig. 11(a)]. As expected, the rate of dissipation was much slower in the sandy clay soil (P1) than in the weathered granite (P3 and P4). Dissipation at the alluvial sand interface was slow during loading, but generally the excess pore pressures generated returned near their equilibrium value (around 2 m of head) fairly quickly after slip. Nearly all the excess pore-water pressure was dissipated in the weathered

granite by January 6, 1998, i.e., 80 h after the load test. On the other hand, about 3 m and 1 m excess pore-water head still remained in the sandy clay and alluvial sand layers, respectively, at this same time. What appeared to be tidal behavior was picked up at P2 and P4, but it is difficult to see since actual peak tide magnitudes dropped by 50% and the scan frequency of instruments was reduced substantially after the pile test.

CHANGES OF LATERAL STRESS AT SOIL/BARRETTE INTERFACE

After the vibrating wire earth pressure cells had been lowered into the excavated trench filled with bentonite, initial readings were taken before the instruments were jacked into position. This allowed an in situ calibration of the pressure cells to be made between the measured values and the theoretical bentonite pressures, using a measured unit weight of bentonite ($\gamma_b = 10.8 \text{ kN/m}^3$). It was found that there was good agreement between the calculated bentonite pressures and the readings recorded by the earth pressure cells; the maximum difference between the calculated and measured pressure was less than 10 kPa. At this point the cells were jacked out laterally to engage the soil.

Just after concreting, the lateral earth pressures increased to values close to the assumed in situ earth pressures before excavation. The measured total earth pressures at the soil/concrete interface also corresponded well with the theoretical bilinear concrete pressure envelope proposed by Ng (1993) and Lings et al. (1994) for concrete case under bentonite during diaphragm wall construction. Over the next two days lateral

pressures remained essentially unchanged in the sandy clay and alluvial sand soils, but increased about 100 kPa in the weathered granite. Further details of the earth pressure measurements and interpretations during the construction of the barrette are reported by Ng et al. (1999).

During the subsequent three-week curing period before the vertical load test, a gradual continuous decrease of lateral earth pressure was measured at all lateral earth pressure cells (about 30 kPa in the sandy clay and alluvial sand and about 60 kPa in the weathered granite). The observed reduction in the contact earth pressure may in large part be due to soil consolidation as indicated by the dissipation of excess positive porewater pressures generated during the construction of the barrette. In addition, the reduction in earth pressure might be caused by small shrinkage of the pressure cell units as a result of a fall in temperature after hydration of cement in the concrete. Lings et al. (1994) also reported reductions in earth pressure at the soil/diaphragm wall interface of a heavily overconsolidated stiff clay.

After the three-week curing period, the final result was an overall decrease of about 20–30 kPa below the assumed initial lateral earth pressures in the sandy clay and alluvial sand, and an increase of about 60 kPa above the original pressures in the weathered granite. This observed net increase in lateral earth pressure could be attributed to the swelling of weathered granite as result of stress relief during the excavation of the trench for constructing the barrette. Davies and Henkel (1981) have reported swelling behavior in weathered granite during the construction of diaphragm wall panels.

The measured earth pressures during the four cycles of load

testing are shown in Fig. 12. The earth pressure cells all remained virtually constant during the first load and unload cycles (LC1 and UC1) when the barrette displacement was small [Fig. 5; Figs. 12(a and b)]. With the beginning of load cycle 2, some small drops of lateral earth pressure were seen in the weathered granite soil layer until the onset of pile failure (interface slip). Upon application of the maximum vertical load of 7,455 kN, a sudden and large reduction of about 100 kPa was measured at cells PC3 and PC4 in the weathered granite. At the same time there were noticeable falls in the other earth pressure cells also (about 20 kPa at PC1 in sandy clay and 45 kPa at PC2 in the alluvial sand). During the partial unloading and early holding period, there was a small recovery in earth pressure at all cells. Over the rest of the holding period, a slow but steady 25 kPa increase of pressure was measured in the weathered granite, while pressures in the sandy clay and alluvial sand remained almost constant [Figs. 12(a and b)]. Twice-a-day uniform fluctuations in lateral pressure were visible at all cells due to tidal pressures.

After the period of maintained load, further loading (LC3) did not cause a significant variation in earth pressures until a vertical load of 7,455 kN was applied and slip at the barrette-soil interface occurred. At this time a significant reduction in earth pressures (75 to 100 kPa) was again recorded by PC3 and PC4 [Fig. 12(c)] in the weathered granite. Small drops in the other earth pressure cells were also recorded at this time. During unloading of cycle 3 (UC3), pressure at PC1 and PC2 basically held constant while a slight recovery was again observed for the cells in the weathered granite.

Application of loading and unloading cycle 4 resulted in an

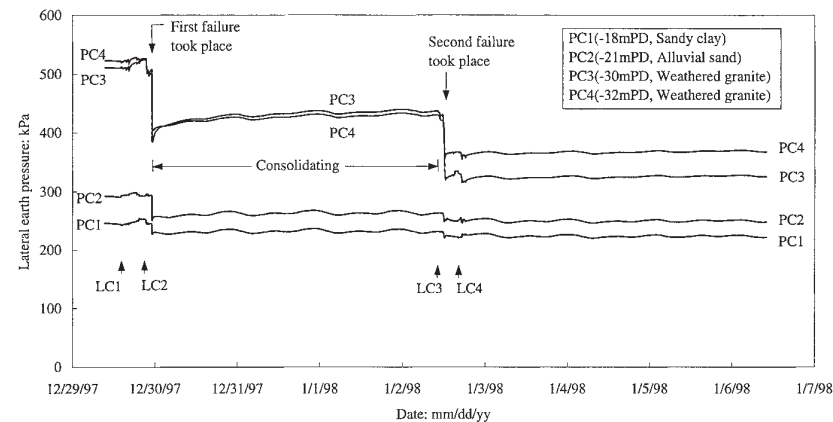


FIG. 12(a). Variations of Lateral Earth Pressure during Load Testing

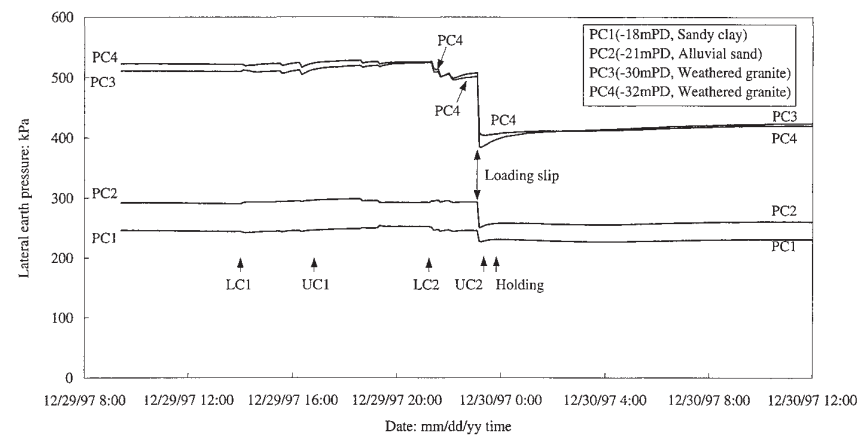


FIG. 12(b). Variations of Lateral Earth Pressure during First Two Load Test Cycles

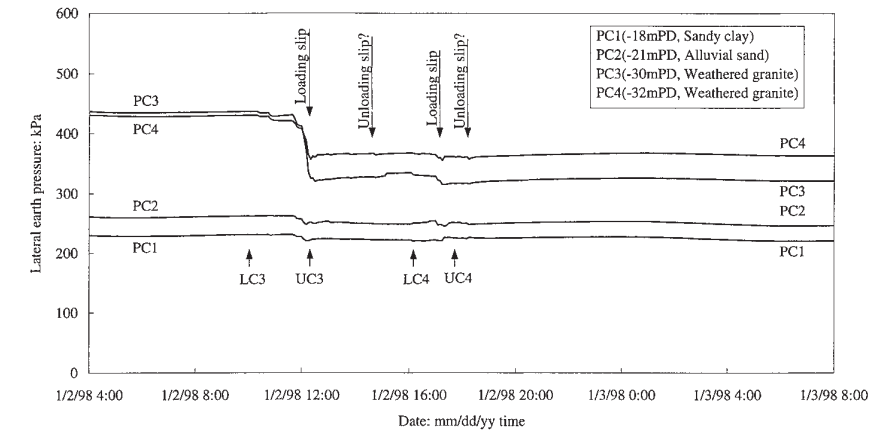
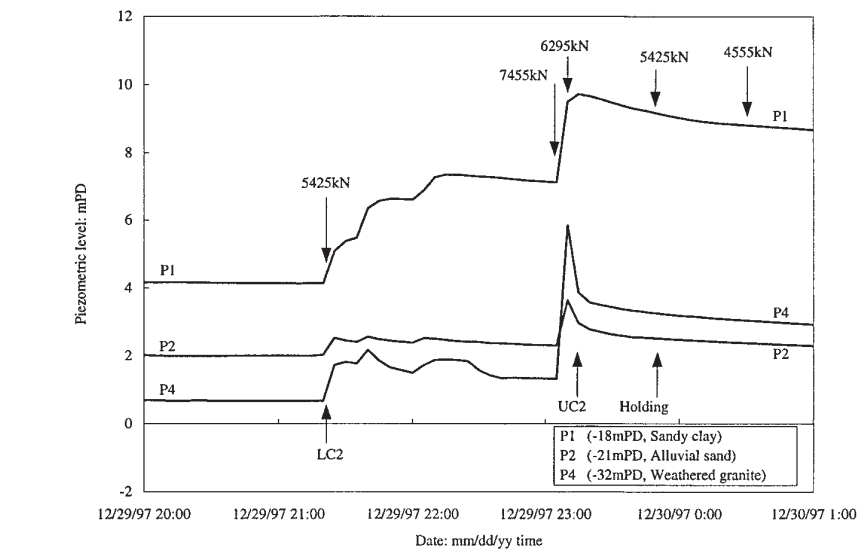
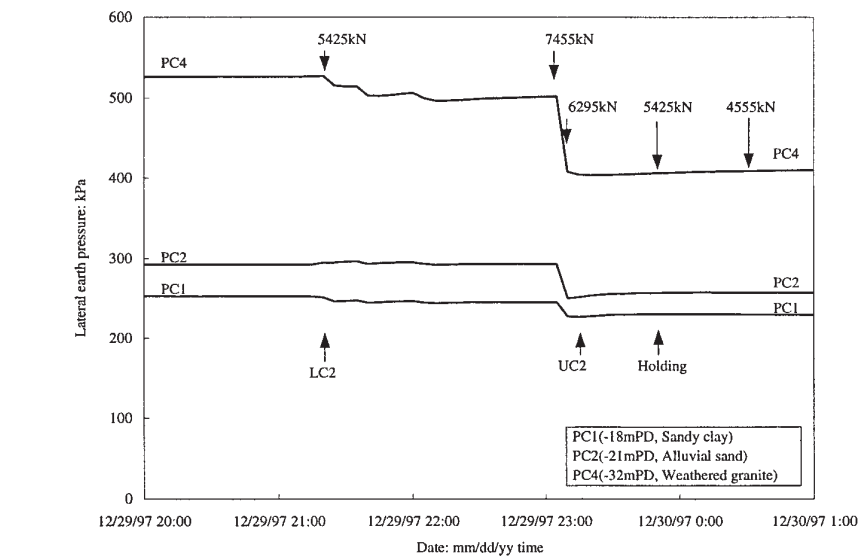


FIG. 12(c). Variations of Lateral Earth Pressure during Last Two Load Test Cycles



(a)



(b)

FIG. 13. Details of Pressure Changes at Interface during Load Cycle 2

overall constant lateral stress readings at all cells except for minor drops in pressure in three of the four cells at the onset of slip at about 7,000 kN. The lateral earth pressure over the next week remained constant in all soil layers.

SUMMARY AND POSSIBLE EXPLANATION OF BARRETTE-SOIL INTERFACE BEHAVIOR

The barrette-soil interface behavior consisting of shear strains, relative movements, pore pressure changes, and lateral earth pressure changes are clearly related. To more easily examine the relationships involved, pore pressure and lateral earth pressure measurements are combined on the same figure for two load cycles. Fig. 13 presents cycle 2 data illustrating virgin loading, slip, and partial unloading behavior (see also cycle 1 and 3 data). Fig. 14 gives details of cycle 4, which shows nonvirgin loading, slip, and unloading behavior soon after pile failure (cycle 3). In general, the behavior can be summarized as follows:

- Vertical pile loading produces shear strains in the soil near the barrette, inducing increased pore-water pressure and no significant changes in lateral earth pressures (highest in the sandy clay, lowest in the alluvial sand).
- Vertical pile unloading leaves pore pressures and lateral earth pressures essentially unchanged.
- At relatively large loading increments near pile failure, virgin slippage (shear failure) along the barrette-soil interface results in a reduction of pore pressures (usually highest in the sandy clay) and significant drops in lateral earth pressures (highest in the weathered granite).
- Finally, subsequent reloading of the pile soon after a failure does not result in pore pressure increases (except in alluvial sand), but when slip initiates, pore pressures again drop while lateral earth pressures maintain their values.

The mainly elastic simple shear of the interface soils apparently produces a “loose” or contractive volumetric response at the soil layers. Since the sandy clay and weathered granite soils have significant clay content, their shearing oc-

curs under undrained conditions, producing increases in the pore-water pressure. Induced excess pore pressures may be higher in the normally consolidated sandy clay layer because of the higher clay content and since more simple shear occurs higher up the barrette (due to increased shortening of the pile). The increases in pore pressure in the alluvial sand layer are somewhat difficult to understand, but the excavation under bentonite would produce a normally consolidated bentonite cake layer at the barrette-sand boundary.

With its high clay content, the sandy clay may act in an undrained manner with no reductions in lateral earth pressure, while the small drops of earth pressure in the weathered granite are likely the result of higher permeability, allowing some consolidation to occur. The very slow dissipation of pore pressures in the sandy clay and relatively rapid dissipation in the weathered granite soil provide further confirmation [Figs. 11(a and b)].

Barrette-soil interface slip triggers consequential new behavior with the general sudden drop in both pore pressure and lateral earth pressure. The mechanisms involved in this basically consistent and repeated behavior are complex. It is possible that the soil behaves or tends to behave in a contractive manner when it is subjected to shearing. The pore pressure may drop because slip occurs during stress reversal, and this allows relaxation of the shear strains leading to a reduction of previous undrained pore-water pressure buildup. On the contrary, this slip also apparently permits some localized drainage and hence contraction of the soil to occur (possibly due to the sudden stress/strain reversal or reorganization of stresses in the local soil matrix). This would cause a release of the large confining stresses induced during previous shearing because the concrete wall of the barrette is rigid and does not act as a constant pressure interface. Any contraction of the soil away from the wall will lead to a reduction in total contact pressure. This might explain the sudden and large reductions of lateral earth pressure compared to the much smaller reductions in pore-water pressure. It should be noted that the concrete wall has a much higher stiffness relative to that of the adjacent soils. The observed complex pattern of interface pore pressure behavior described in the present barrette field test has been observed both in the field (Earth 1986; Matlock 1992) and the laboratory where pile/normally consolidated clay interface tests have been carried out measuring excess pore pressures during two-way cyclic loading as reported by Rigby and Desai (1996) and Rigby (1997). One observation of these authors is that the two-way cyclic shear of a pile-clay interface results in a continuous increase in excess pore pressure unless interface slip failure occurs, causing a sudden drop in excess pore-water pressure.

After cycle 2, at the Kowloon Bay test, when the soil was

allowed to consolidate and strengthen, subsequent shearing of the soil during load cycle three resulted in the type of virgin loading behavior described previously for cycle 2 [Figs. 11(b and c)]. In contrast, load cycle 4 immediately followed cycle 3 so the behavior was more consistent with continued slip behavior since the interface was still weak.

A further interesting point is the occurrence of the same “slip” pattern of behavior at a small scale [Figs. 11(c) and 12(c)], during the last pile unloading step for cycles 3 and 4. In cycle 1 failure had not occurred yet, and in cycle 2 the barrette was not fully unloaded, so the sudden drops of pore pressure observed in both cycles 3 and 4 seem to be indicative of possible additional slip occurring.

STANDARD PRACTICE FOR DESIGN OF BARRETTES IN HONG KONG

Barrette design in weathered granite in Hong Kong has been essentially based on empirical approaches (Pratt and Sims 1990). An empirical relationship between an uncorrected SPT-N value before construction and allowable skin friction of 0.5N kPa with a limit of 100 kPa and an allowable end bearing pressure of 5N with a limit of 1,200 kPa are commonly used in Hong Kong. With this allowable load approach, the overall factor of safety (FOS) is not explicitly defined. However, a FOS greater than 2 is anticipated according to experience gained in Hong Kong.

To compare the current measured skin friction at Kowloon Bay with other tested barrettes in weathered granite in Hong Kong, the two most common approaches are adopted. Figs. 15 and 16 show the interpreted field test results from seven relatively well-documented case histories for barrette construction in weathered granite. Details of B1–B5 tests and test B6 are given by GEO (1996b) and Lo (1997), respectively. The test at the International Trademark in Kowloon Bay (Ho 1994) is identified as B5, and the current test is marked as B7 in the figures. The shaft friction coefficient β (GEO 1996b) is defined as the ratio between the ultimate skin friction and the mean vertical effective stress, assuming that the effective cohesion is zero. It can be seen that there is a large scatter in the deduced skin frictions; β varies from 0.1 to 0.46 whereas τ/N falls between 0.77 and 2.3. The variability may be a result of different methods of construction, quality of workmanship, quality and consistency of SPT testing, natural variations of ground conditions, and methods of interpretation.

By plotting the current test result (B7) in Fig. 15, the mobilized shear stress over SPT-N ratio is close to 1.5. This suggests an implicit FOS greater than 2. On the other hand, the deduced β value based on the effective stress principle is only 0.1 (Fig. 16), which is only half of the value obtained from a

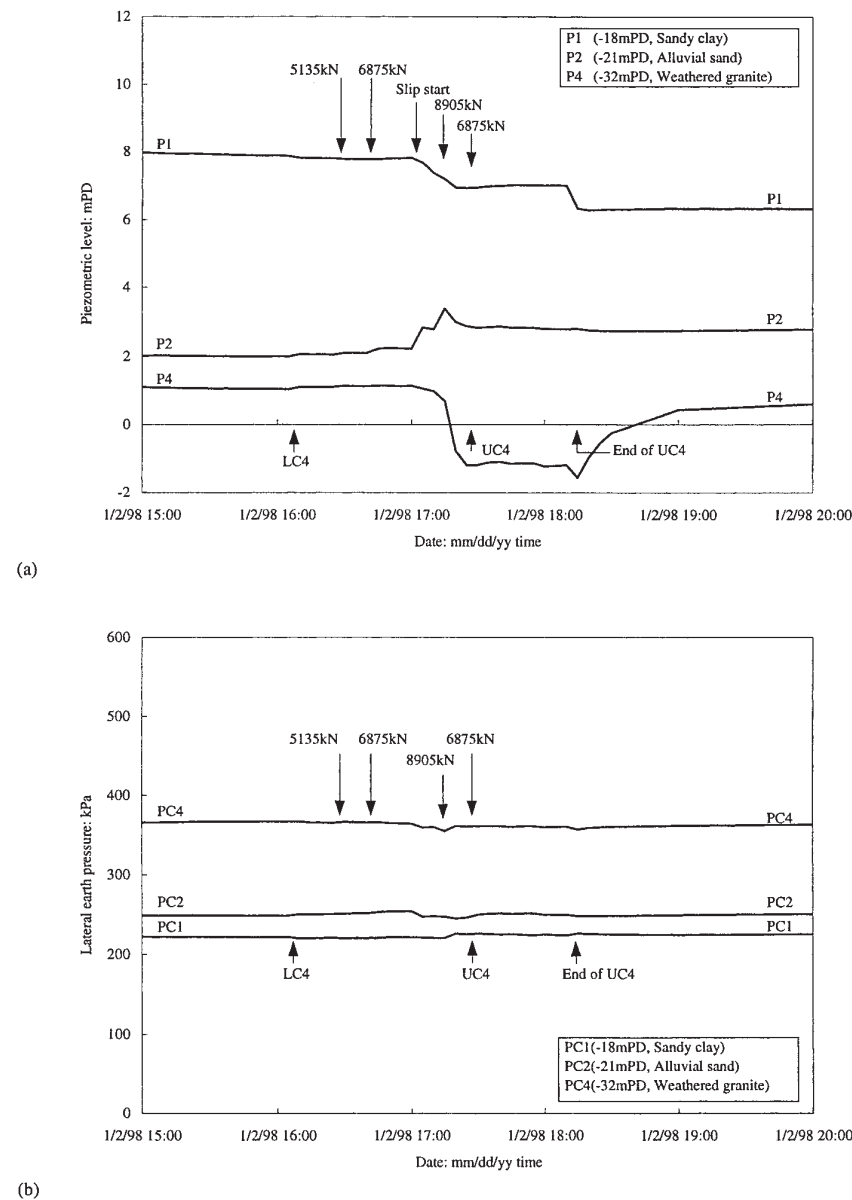


FIG. 14. Details of Pressure Changes at Interface during Load Cycle 4

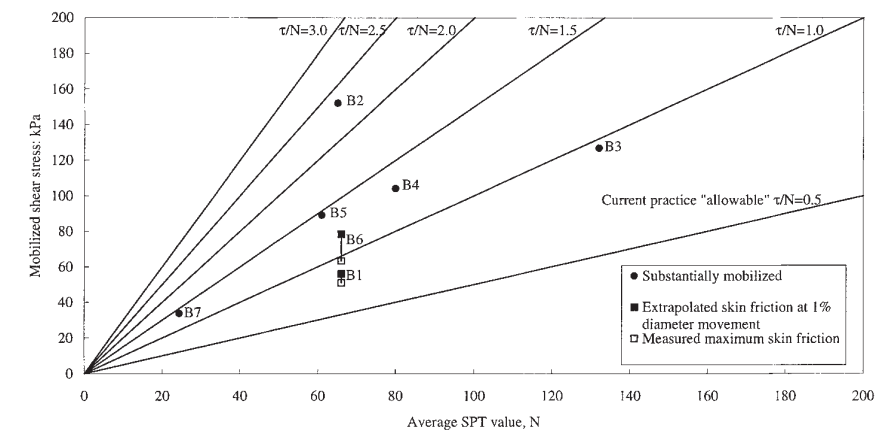


FIG. 15. Relationship between Skin Friction and Mean SPT Value, N for Barrettes

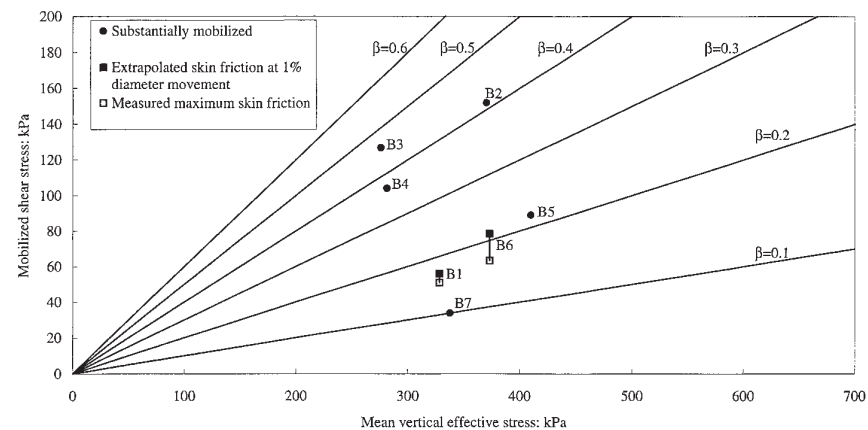


FIG. 16. Relationship between Skin Friction and Mean Vertical Effective Stress for Barrettes

similar site (i.e., B5). This low β value may be attributed to the unintended long delay in concreting after completion of the excavation (43 h). A thicker bentonite cake may have formed at the granite/barrette interface leading to a lower skin friction mobilized at the granite/barrette interface. The test results shown in Figs. 15 and 16 clearly indicated that the current empirical uncorrected SPT-N value approach and the effective stress β -method were inconsistent.

CONCLUSIONS

1. A well-instrumented 2.8 m by 0.8 m by 39.7 m deep excavated concrete pile (barrette) was successfully constructed and tested purely for research purposes in Hong Kong. This test pile was a joint effort and collaboration between the university, government agencies, and the industry. Due to the formation of a "soft" base at the bottom of the barrette, vertical displacement of more than 100 mm (6% of equivalent diameter) was permitted. This large vertical displacement of the barrette enabled skin friction at the barrette/soil interface to be fully mobilized.
2. The shear stress in all soil layers was fully mobilized at about 2.4% of the equivalent pile diameter with no or little softening behavior observed. At the maximum applied load (8,905 kN), the mobilized skin friction of about 30 kPa was found for the fill, marine clay, alluvial sand, and weathered granite, and about 15 kPa for the sandy clay. Normalized shear stress (τ/N) of the weathered granite ranged from 0.9 to 2.9 were obtained.
3. During the vertical load tests, specially installed instrumentation allowed the measurement of an unusual and complex response of pore-water pressures and earth pressures at several points along the barrette/soil interface. During each load cycle (except LC4), a buildup of excess positive pore-water pressure was recorded in the sandy clay and weathered granite as the vertical applied load on the barrette increased. The increase in pore-water pressure was likely caused by the undrained contractive behavior of the soils. There was no significant change in lateral earth pressure during each load and unload cycle, except at the occurrence of a large vertical displacement of the barrette. When loading caused significant slippage of the barrette within the soil, a consistent and substantial reduction in lateral total earth pressures resulted together with a drop of excess pore-water pressures. The earth pressure drop was most significant in the weathered granite soils, the changes in pore-water pressure more significant in the sandy clay.
4. The increases of pore-water pressure during pile loading

- and the sudden significant drop of lateral earth pressure at the onset of pile failure for some soil layers illustrate that the complex barrette-soil interaction will likely be best understood using a soil mechanics perspective. A possible mechanism to explain the behavior is that slip occurring during stress reversal permits some localized drainage and contraction of the soils. Since the concrete wall of the barrette is rigid and does not act as a constant pressure interface, any contraction of the soils away from the wall will lead to a reduction in total contact pressure.
5. The current test results indicated that the empirical SPT-N value approach and the β -method were inconsistent.

ACKNOWLEDGMENTS

The writers are grateful for the contribution provided by Paul Y. Foundation Ltd., who constructed the heavily instrumented research pile. Other sponsors of this test barrette include the Geotechnical Engineering Office of the Hong Kong Government, Fong On Construction Ltd., MTRC, Geotechnical Instruments Ltd., and the Hong Kong Institution of Engineers. In addition, the writers would like to acknowledge the financial support from the two research grants, HIA and CRC, awarded by the Hong Kong University of Science and Technology and the Research Grant Council of Hong Kong, respectively. Technical input and support from Professors C. K. Shen and Wilson Tang of the Hong Kong University of Science and Technology, and Martin Pratt and David Ng of Bachy Soletanche Group, are highly appreciated.

APPENDIX. REFERENCES

- Davies, R. V., and Henkel, D. J. (1981). "Geotechnical problems associated with the construction of Chater Station, Hong Kong." *Geotech. Seminar, Session No. 5*, HKIE.
- Earth Technology Corporation. (1986). "Pile segment tests—Sabine Pass: Some aspects of the fundamental behavior of axially loaded piles in clay soils." *ETC Rep. No. 85-007*, Houston/Long Beach.
- Geotechnical Engineering Office (GEO). (1996a). "R&D project PIL10a research on large-section excavated piles—trial piles, TNK959, Kowloon Bay." *Soil Testing Rep. No. 631*, Department of Civil Engineering of the Hong Kong Government of the Special Administrative Region, China.
- GEO. (1996b). "Pile design and construction." *GEO Publ. No. 1/96*, Department of Civil Engineering of the Hong Kong Government of the Special Administrative Region, China.
- Ho, K. K. S. (1994). "Behaviour of the instrumented trial barrette for the Trademart Development at N.K.I.L. 6032, Kowloon Bay." *Spec. Proj. Rep. SPR8/94*, Geotechnical Engineering Office, Department of Civil Engineering of the Hong Kong Government of the Special Administrative Region, China.
- Lings, M. L., Ng, C. W. W., and Nash, D. F. T. (1994). "The pressure of wet concrete in diaphragm wall panels cast under bentonite." *Geotech. Engrg. Proc. Instn. of Civ. Engrs., U.K.*, London, 107(July), 163–172.
- Lo, D. O. K. (1997). "Behavior of the instrumented test barrette for the west Kowloon corridor stage IV project." *Spec. Proj. Rep. SPR 2/97*, Geotechnical Engineering Office, Civil Engineering Department of the Hong Kong Special Administrative Region, China.

- Matlock, H. (1992). "Field and laboratory testing." *Proc., U.S.-Canada NSF Workshop on Recent Accomplishments and Future Trends in Geomech. in the 21st Century*, M. Zaman, C. S. Desai, and A. P. S. Selvadurai, eds., 58–64.
- Ng, C. W. W. (1993). "Lateral stress development in diaphragm walls during concreting." *Proc. Int. Conf. on Retaining Struct.*, Thomas Telford, London, 77–80.
- Ng, C. W. W., Rigby, D., Lei, G. H., and Ng, S. W. L. (1999). "Observed performance of a short diaphragm wall panel." *Geotechnique*, London, 49(5), 681–694.
- Pratt, M. and Sims, M. J. (1990). "The application of new techniques to solve deep basement and foundation problems." *Proc. Int. Conf. on Deep Foundation Practice*, 189–195.
- "Quarry bay times and heights of high and low waters 1997." (1997). *Tide Tables for Hong Kong 1997*, Royal Observatory, Hong Kong, 25.

- "Quarry bay times and heights of high and low waters 1998." (1998). *Tide Tables for Hong Kong 1998*, Royal Observatory, Hong Kong, 20.
- Rigby, D. B. (1997). "Pore pressure behavior of clay-steel interfaces." *Proc., 2nd Int. Symp. on Struct. and Found. in Civ. Engrg.*, HKUST, Hong Kong, 251–256.
- Rigby, D. B., and Desai, C. S. (1996). "Testing and constitutive modeling of saturated interfaces in dynamic soil-structure interaction." *Rep. to Nat. Sci. Found.*, Dept. of Civ. Engrg. and Engrg. Mech., University of Arizona, Tucson, Ariz.
- Shen, C. K., Ng, C. W. W., Tang, W. H., and Rigby, D. (1997). "Testing a friction barrette in decomposed granite in Hong Kong." *Proc., 14th Int. Conf. Soil Mech. and Found. Engrg.*, Vol. 4, 2423–2426.
- Strange, P. J. (1990). "The classification of granite rocks in Hong Kong and their sequence of emplacement in Sha Tin, Kowloon and Hong Kong Island." *Geotech. Soc. of Hong Kong Newsletter*, Hong Kong, 8(1), 18–27.



Contents lists available at SciVerse ScienceDirect

Tunnelling and Underground Space Technology

journal homepage: www.elsevier.com/locate/tust

Three-dimensional centrifuge modelling of the effects of twin tunnelling on an existing pile

C.W.W. Ng, H. Lu*, S.Y. Peng

Department of Civil and Environmental Engineering, Hong Kong University of Science and Technology, Clear Water Bay, Kowloon, Hong Kong

ARTICLE INFO

Article history:

Received 6 March 2012
 Received in revised form 11 July 2012
 Accepted 23 July 2012
 Available online xxx

Keywords:

Twin tunnelling
 Piles
 Three-dimensional
 Soil–structure interaction
 Centrifuge modelling
 Dry sand

ABSTRACT

Tunnelling activity inevitably induces soil stress changes and ground deformation, which may affect nearby existing pile foundations. Although a number of studies have been carried out to investigate the effects of tunnelling on existing piles, the excavation of only one tunnel is often considered. The fundamental interaction between twin tunnel construction and an existing pile foundation has not been thoroughly studied. In this study, a series of three-dimensional centrifuge model tests investigating the effects of twin tunnel construction on an existing single pile in dry sand were conducted. The influence of the depth of each tunnel relative to the pile was investigated by constructing the twin tunnels either close to the mid-depth of the pile shaft or near the pile toe. The pile settlement induced by the excavation of the twin tunnels is found to be closely related to the depth of each tunnel relative to the pile. The measured cumulative pile settlement due to tunnelling near the toe is about 2.2 times of that due to tunnelling near the mid-depth of the pile shaft. Apparent losses of pile capacity of 36% and 20% are identified due to the construction of twin tunnels near the pile toe and at the mid-depth of the pile, respectively. Although there is an increase in the axial force induced in the pile when a tunnel is constructed at the mid-depth of the pile, significant increases in bending moment is not observed in any of the tests.

© 2012 Elsevier Ltd. All rights reserved.

1. Introduction

Tunnel construction inevitably causes soil stress changes in the ground and hence induces ground movements. Uncontrolled ground movements induced by tunnelling may cause cracking in buildings and gas mains, or induce additional loads on piles of nearby structures. In urban cities, it is not uncommon to encounter existing piles during tunnel constructions. Estimation of the effects of tunnelling on existing pile foundations of buildings poses a major challenge to designers. It is particularly vital to estimate the tunnelling effects when two new tunnels are to be built near an existing pile.

Bezuijzen and Schrier (1994) studied the influence of bored tunnels on pile foundations. They pointed out that the pile settlement can be quite significant if the distance between pile and tunnel is less than the tunnel diameter. Loganathan et al. (2000) assessed tunnelling-induced ground deformations and their adverse effects on pile foundations in clay. Tunnelling-induced bending moment and axial force in the piles of a pile group were investigated by modelling volume loss of a tunnel in a single stage. They concluded that the tunnelling-induced bending moment may be critical when

the centerline of the tunnel is located near the pile toe. Jacobsz et al. (2004) investigated the adverse effects of tunnelling beneath a pile in dry sand. An influence zone was identified above and around the tunnel in which the pile could suffer significant settlement, depending on the volume loss induced by the tunnelling. Lee and Chiang (2007) studied the tunnelling-induced bending moment and axial force in a single pile in saturated sand. Tunnels were embedded at various cover-to-diameter ratios. The authors concluded that the depth of the tunnel relative to the pile has a significant influence on the distribution of the bending moment along the pile. As far as the authors are aware, the three-dimensional centrifuge modelling of the effects of twin tunnelling on a single pile has not been reported.

Mroueh and Shahrour (2002) carried out three-dimensional elastoplastic finite element analyses to study the influence of a tunnel construction on a single pile as well as on pile groups. The numerical results showed that there is a significant reduction in the tunnelling-induced axial force and bending moment in the piles furthest away from the tunnel due to the group effect. Lee and Ng (2005) carried out a three-dimensional, elasto-plastic, coupled-consolidation numerical analysis to investigate the effects of an open face tunnel excavation on an existing loaded pile. It is shown that the factor of safety (FOS) of a pile can be reduced from 3.0 to 1.5 due to the additional settlement of a pile induced by tunnelling when a settlement-based failure criterion (Ng et al., 2001a) is used.

* Corresponding author. Tel.: +852 5104 8252; fax: +852 2243 0040.
 E-mail addresses: cecwwng@ust.hk (C.W.W. Ng), luhu@ust.hk (H. Lu), muffinpp@ust.hk (S.Y. Peng).

The effects of tunnel construction on the nearby pile foundations are obviously three dimensional. A fundamental understanding of the three-dimensional tunnel-soil-pile interaction is needed. In addition, few researchers have investigated the effects of twin tunnelling on piles, except Pang (2007), who reported the field monitoring and numerical study of the effects of twin tunnelling on an adjacent pile foundation in Singapore. A northbound tunnel and a southbound tunnel were constructed near piles one after the other. The smallest clear distance between the tunnels and piles was 1.6 m. Results of the field study showed that the piles were subjected to a large dragload due to an induced soil settlement in residual soil. However, strain gauges are only instrumented along pile portion near tunnels. The pile settlement due to tunnelling is not reported.

In this study, a series of three-dimensional centrifuge model tests were performed to investigate the behavior of a single pile due to the construction of twin tunnels one after the other. The effects of the three-dimensional tunnel excavation process were simulated in-flight by controlling the volume loss at 1.0% in each stage of the three-dimensional excavation of each tunnel. The twin tunnels in each test are located at either mid-depth of the pile or the pile toe. In addition to measurements of ground surface settlement and pile settlement, the bending moment and axial force induced in the pile by the tunnelling in different stages of construction were captured. The objective of this study is to investigate the response of an existing pile when a new tunnel excavation is to be carried out nearby. It is intended that results from this study can assist engineers and designers to choose and design the location (i.e., the depth) of the new tunnel.

2. Centrifuge modelling

2.1. Experimental program and setup

The fundamental principle of centrifuge modelling is to recreate the stress conditions, which would exist in a full-scale problem, in a model of a greatly reduced scale. This is done by subjecting model components to an enhanced body force, which is provided by centripetal acceleration ($r\omega^2$) when a centrifuge rotates at a constant angular velocity (ω) about the center of the centrifuge arm with radius, r . For instance, an 100 m prototype stress conditions can be replicated in a centrifuge by an 1 m height model when the Earth's gravity (g) is enhanced by 100 times (i.e., $r\omega^2 = Ng = 100g$). Thus, centrifuge is suitable for simulating stress-dependent materials such as soils. More details, scaling laws and centrifuge applications are given by Schofield (1980), Taylor (1995) and Ng et al. (2006). Table 1 summarizes all the relevant scale laws in this study.

In total, four centrifuge model tests were carried out at the Geotechnical Centrifuge Facility of the Hong Kong University of Science

and Technology (Ng et al., 2001b, 2002). The 400g ton centrifuge has an arm radius of 4.2 m and is equipped with a two-dimensional hydraulic shaking table and a four-axis robotic manipulator. All of the centrifuge tests were carried out at an acceleration of 40g.

Fig. 1a shows the schematic elevation view of Test T. A single pile is located at the center of each model container. Test T is designed to investigate the behavior of a pile due to a single tunnel constructed near pile toe in dry sand. The model pile had a diameter of 20 mm (0.8 m in prototype) and was 600 mm long (24.0 m in prototype). The pile cap was elevated by 110 mm and therefore the embedded depth of each pile was 490 mm (19.6 m in prototype). The tunnel diameter (D) was 152 mm (6.08 m in prototype). The C/D ratio (cover-to-diameter ratio) of the tunnel is 2.7. The horizontal distance from the centerline of the tunnel to the pile was $0.75D$. In addition, a separate test (Test L) is carried out to obtain the load settlement curve of the single pile without tunnelling effects. This test has the same configuration of Test T but only without the model tunnel.

As shown in Fig. 1b, Test TT was designed to study the effects on the pile induced by the construction of twin tunnels, one after the other, near the pile toe. The C/D ratio of each tunnel is 2.7, same as that in Test T. Fig. 1c shows the schematic elevation view of Test SS. This test was designed to investigate pile responses induced by the construction of twin tunnels near the mid-depth of pile shaft. The C/D ratio of each tunnel is 1.5. A summary of the test program is given in Table 2.

Fig. 2a and b shows the plan views for Test T and Tests TT and SS, respectively. In Test T, the model tunnel had a length of 228 mm, which was equal to $1.5D$. The three-dimensional tunnel construction was simulated in three stages, with the tunnel face advancing by a distance of $0.5D$ in each stage. In Tests TT and SS, the longitudinal length of each tunnel was 380 mm, which was equivalent to $2.5D$. The tunnel excavation was simulated in five stages, again with the tunnel face advancing by a distance of $0.5D$ in each stage. A photograph of the model package is shown in Fig. 3a.

2.2. Simulation of tunnel construction

In simulating of tunnel advancement, it is common to model overall volume loss resulting from tunnelling effects in practice (Taylor, 1995; Mair, 2008), rather than trying to simulate different construction steps in centrifuge. Obviously, this implies that some construction details like erection and deformation of tunnel liners, stiffness of liners and workmanship are not simulated separately. Only the overall result like volume loss due to actual tunnelling is simulated. Obviously, this type of modelling is not ideal. However, it does capture the essential effects (i.e., volume loss) of tunnelling and can meet the comparative objective of different simulated cases in this paper.

In the single tunnel test, the model tunnel consisted of three cylindrical rubber bags. In the twin tunnel tests, each model tunnel consisted of five cylindrical rubber bags (see Fig. 3b). Between two rubber bags was a rigid aluminum divider to control and separate the volumes of water inside so that volume change in each rubber (i.e., the tunnel volume loss) can be controlled independently. Each rubber bag was filled with de-aired water. Three-dimensional tunnel construction was simulated in-flight by draining away a controlled amount of water from each rubber bag one by one. The amount of water drained away was controlled as 1.0% of the total volume of the cylindrical rubber bag. This is to simulate an equivalent volume loss of 1.0% of excavated cross section area of the tunnel face during each stage of tunnel construction. Since the effects of tunnel excavation were modelled by inducing an equivalent volume loss resulting from various construction factors and tunnel

Table 1
Centrifuge scaling factor.

Physical quantity	Scaling factor (model/prototype)
Gravitational acceleration	n
Length	$1/n$
Area	$1/n^2$
Volume	$1/n^3$
Settlement	n
Stress	1
Strain	1
Force	$1/n^2$
Density	1
Mass	$1/n^3$
Flexural stiffness	$1/n^4$
Bending moment	$1/n^3$

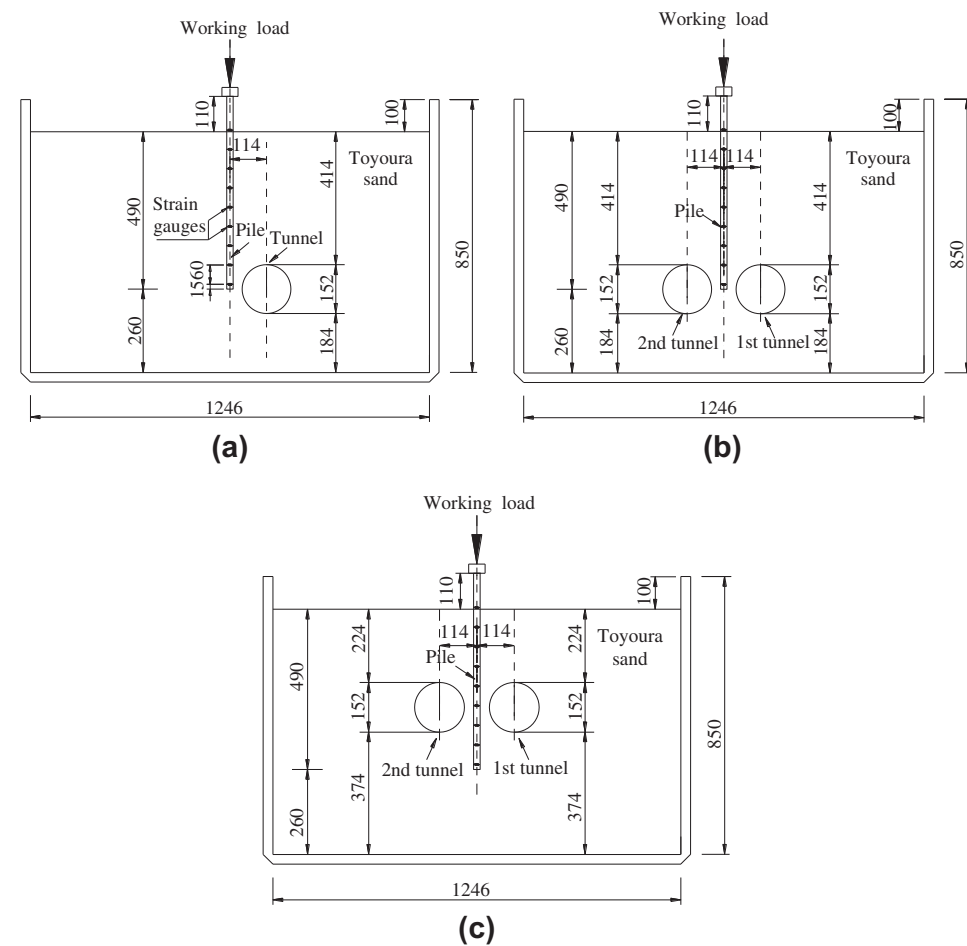


Fig. 1. Elevation view of centrifuge model: (a) Test T; (b) Test TT; (c) Test SS. All dimensions are in mm in model scale.

Table 2
Test program.

Test ID	C/D	Remark	Relative density of sand (%)
L	N/A	Pile load test	60
T	2.7	Single tunnelling near pile toe	60
TT	2.7	Twin tunnelling near pile toe	65
SS	1.5	Twin tunnelling near pile shaft	62

N/A denotes not applicable.

liner in the field, model tunnel liner is not needed to be simulated in the centrifuge tests.

2.3. Model piles and instrumentation

The instrumented model pile was fabricated from an aluminum tube (see Fig. 1a). Nine levels of full Wheatstone bridge of strain gauges were installed to record bending moment and axial force along the entire pile length. The strain gauges were protected by a thin layer of epoxy. Prior to a centrifuge test, calibration was carried out to obtain a relationship between an applied bending moment to the pile and the corresponding reading of each full Wheatstone bridge. For structural elements, the bending stiffness (EI) of pile was chosen as the vital governing property to be satisfied. It can be derived that the scaling requirement for a model pile

(EI)_m is equal to $N^{-4}(EI)$ _p (refer to Table 1), where N is the number of times of gravity enhanced in a centrifuge test, E is Young's modulus, I is the second moment of area for a cross-section, and subscripts m and p refer to the model and prototype scale, respectively. The model pile had an axial rigidity ($E_m A_m$) of 7473 kN and a bending rigidity ($E_m I_m$) of 273 N m², which are corresponding to prototype $E_p A_p$ of 11,957 MN and $E_p I_p$ of 701 MN m² of a real concrete pile, respectively. The pile is "wished-in-place" in the sand bed. Thus, pile installation effects are not simulated.

In each test, the pile was loaded in-flight (i.e., while the centrifuge is spinning) using a hydraulic jack. A load cell was installed at the piston of the jack to control applied load. Settlement of the pile was measured by a linear variable differential transformer (LVDT) located at the pile head.

2.4. Model preparation

Dry Toyoura sand ($G_s = 2.65$, $e_{max} = 0.977$, $e_{min} = 0.597$, $\phi'_{cv} = 31^\circ$) (Ishihara, 1993) was used in each test. Each centrifuge model was prepared by the pluvial deposition method. Sand was "rained" from a hopper, which was kept 500 mm above the surface. The measured average relative density of each test is also given in Table 1. Since the scaling factor for soil density is one (see Table 1), soil with a relative density of 60–65% (refer to Table 2) in prototype was modelled in each centrifuge test. It is well understood that the stiffness of a soil (i.e., shear modulus, G or Young's modulus, E_s) is

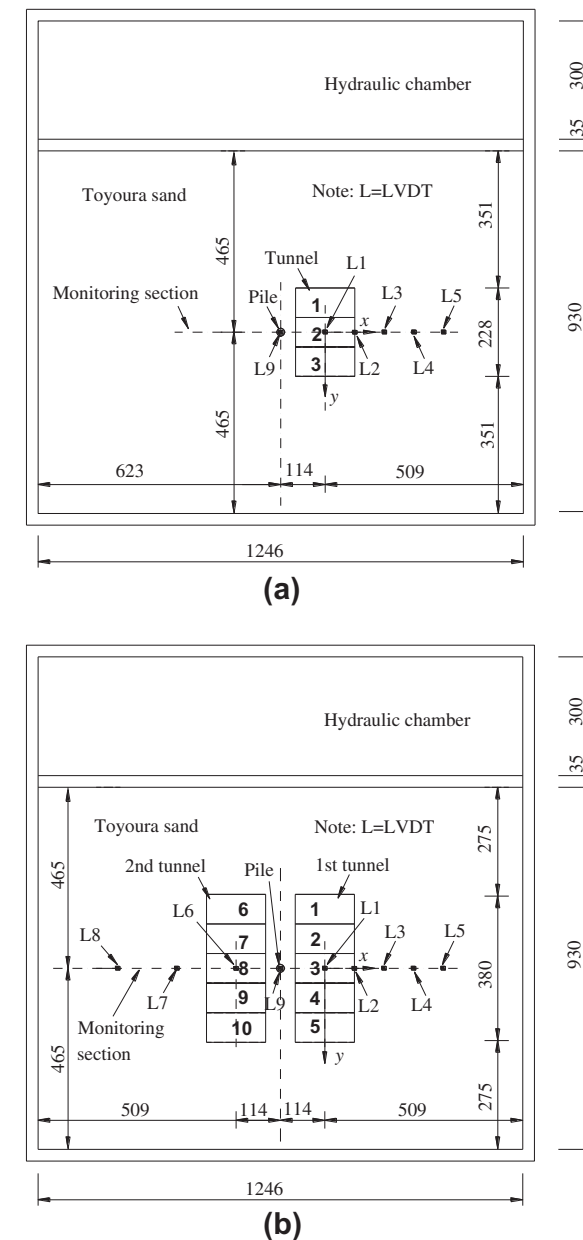
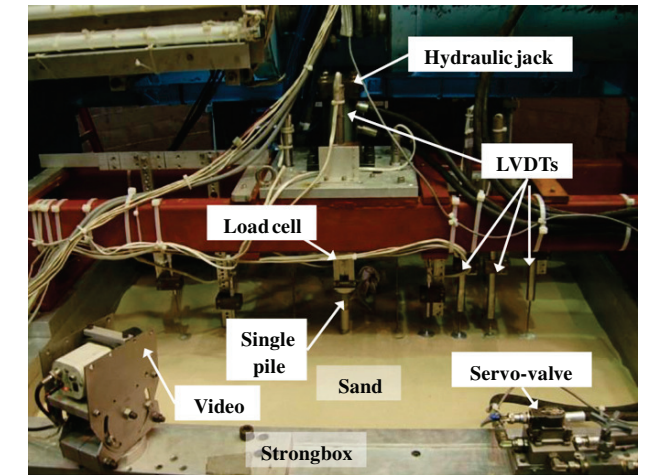


Fig. 2. Plan view of centrifuge model: (a) Test T; (b) Test TT and Test SS. All dimensions are in mm in model scale.

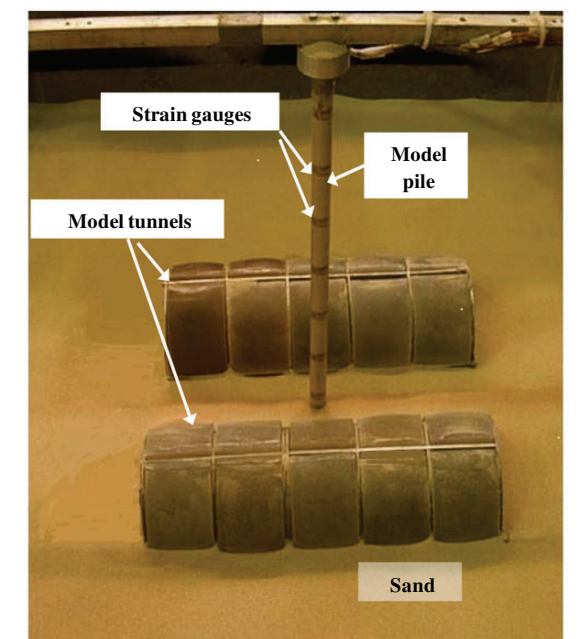
dependent on its density and stress level. The stress level is simulated correctly and prototype soil density is prepared in a centrifuge. Therefore, the stiffness of the ground should be comparable to that of full scale in prototype.

2.5. Test procedure

After model preparation, the acceleration of the centrifuge was increased to 40g. The model pile was loaded in-flight at 40g in a number of steps. In each step, an incremental vertical load of 100 N (160 kN in prototype) was applied. Each load increment was maintained for 3 min. Once the load had reached the working load (1200 N), tunnel construction with the designed volume loss of 1.0% was carried out. Three construction stages were simulated



(a)



(b)

Fig. 3. (a) A typical model setup; (b) model tunnels and model pile.

in-flight by draining away water from each of the rubber bags one after the other in Test T, as shown in Fig. 2a. A similar procedure was adopted in Tests TT and SS, except five tunnel construction stages were simulated. Throughout each test, ground surface settlement, settlement of the pile, induced bending moment and axial force along the pile were recorded.

3. Test results

All test results presented in this paper are in prototype scale, unless stated otherwise.

3.1. Determination of the axial load carrying capacity of the pile

Prior to tunnelling, it is necessary to obtain the capacity of the pile so that the working load can be deduced. A pile load test

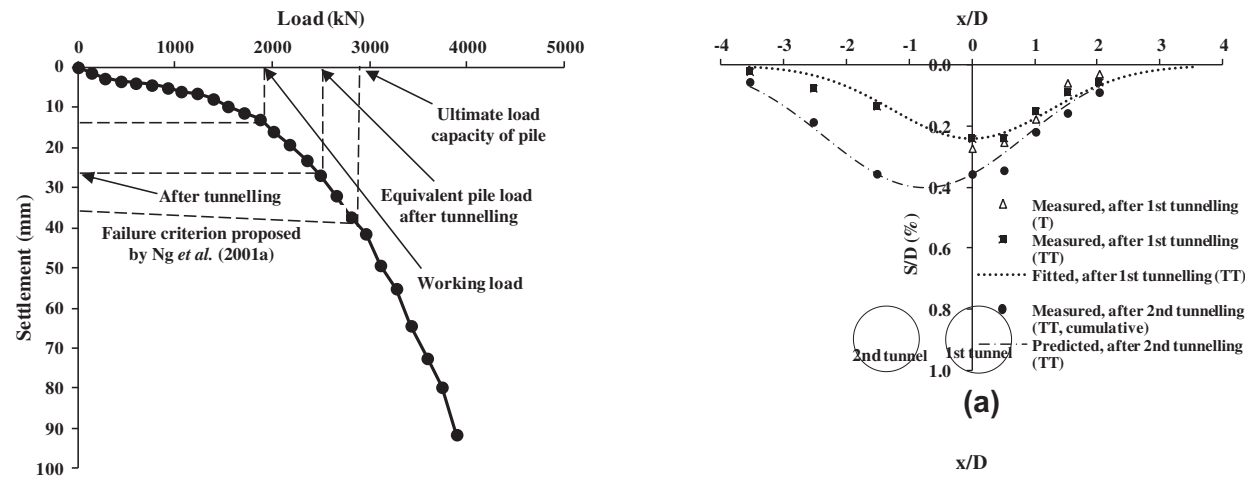


Fig. 4. Load settlement relationship obtained from load test without tunnelling (Test L).

(i.e., Test L) was carried out. Fig. 4 shows the measured load settlement relationship. The load applied to the pile cap was gradually increased to 4 MN at increments of 100 kN in each step. The ultimate axial load capacity was determined based on a displacement-based failure criterion proposed by Ng et al. (2001a). This failure criterion is expressed as follows:

$$\delta_{ph,max} \cong 0.045d_p + \frac{1}{2} \frac{P_h L_p}{A_p E_p} \quad (1)$$

where $\delta_{ph,max}$ is the maximum pile head movement which defines the ultimate load, P_h is the pile head load, L_p is the pile length, E_p is the elastic modulus of pile shaft, A_p is the cross-sectional area of the pile, and d_p is the pile diameter. The failure criterion proposed by Ng et al. (2001a) is a semi-empirical method for estimating an approximate interpreted failure load for pile. The method is based on a moderately conservative estimation of the movement required to mobilize toe resistance and incorporates observations of shaft shortening from actual pile loading tests. Both the 5% D criterion proposed by O'Neill and Reese (1999) and 10% D criterion proposed by Weltman (1980) do not include shortening of pile shaft and thus they may not be appropriate for long piles. Both criteria are displacement-based failure criteria. The 5% D and 10% D criterion defines the failure load of pile as the load causing a settlement of 5% and 10% of the pile diameter, respectively.

As shown in the figure, the ultimate load capacity of the pile was 2.88 MN. A working load of 1.92 MN was adopted with a factor of safety of 1.5. A pile settlement of 1.6% d_p was observed due to the applied working load.

3.2. Ground surface settlement

Fig. 5a shows the extents of ground surface settlement (S) measured by LVDTs 1–8 (as shown in Fig. 2) in Tests T and TT. Both the measured surface settlement and the transverse distance from the centerline of the first tunnel in Test TT and the only tunnel in Test T (x) were normalized by the diameter of tunnel (D).

In Test T, only half of the ground surface settlement trough was measured. At the end of the three stages of tunnel excavation, the measured maximum settlement was 0.27% D above the centerline of the tunnel. At a distance of 2 D from the centerline of the tunnel, a surface settlement of 0.03% D was also measured. In Test TT, a maximum settlement of 0.24% D occurred at the centerline of the first tunnel after its completion. The consistency between the

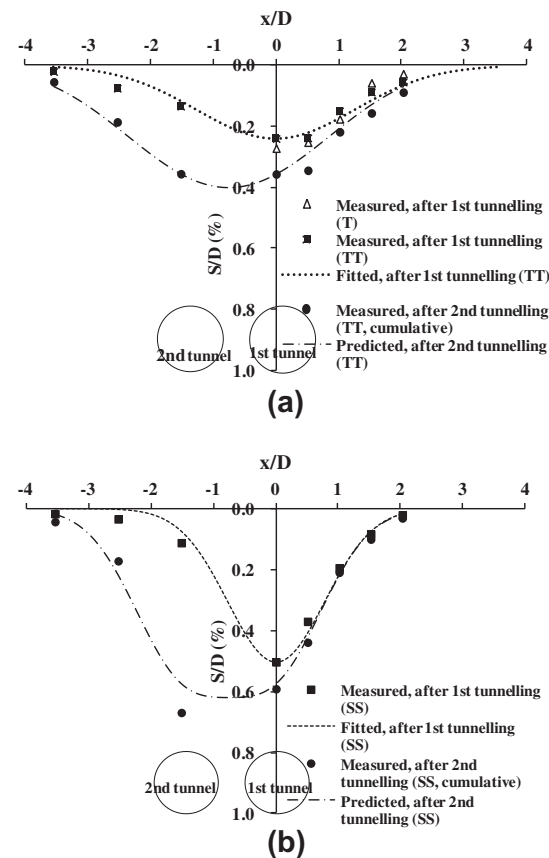


Fig. 5. Ground surface settlement induced by tunnel excavation: (a) Test T and Test TT; (b) Test SS.

two measured maximum settlement values illustrates the repeatability of the tests. After the excavation of the second tunnel in Test TT, the measured maximum surface settlement above the second tunnel was almost the same as that due to the construction of the first tunnel. The measured maximum accumulated settlement was 0.35% D after the excavation of the twin tunnels. Since no LVDT was installed between the centerlines of the two tunnels, the location where the maximum settlement occurred could not be identified. However, the maximum settlement was unlikely to have occurred above the centerline of the second tunnel.

The ground surface settlement profile due to tunnel construction may be represented by a Gaussian distribution (Peck, 1969). Ground surface settlement S is defined as

$$S = S_{max} \exp(-x^2/2i^2) \quad (2)$$

$$S_{max} = \frac{V_s}{\sqrt{2\pi}i} \quad (3)$$

where S_{max} is the maximum settlement at the tunnel centerline, i and x are the lateral distances from the tunnel centerline to the point of inflection and any other points on the settlement trough, respectively. V_s is the volume of settlement trough.

Eq. (2) was adopted to fit the measured values of ground surface settlement induced by excavation of the first tunnel in Test TT. As expected, the measured S_{max} was located above the centerline of the first tunnel. The best-fitted curve using an i of 7.5 m is shown in Fig. 5a. As proposed by O'reilly and New (1982), i can be represented by KZ , where Z is the vertical distance from ground surface to the center of tunnel. Following the above equation, the deduced

K value for the best-fitted curve is 0.39, which lies between the values 0.25 and 0.45 suggested by Mair and Taylor (1997) for tunnelling in sand.

Based on the design chart proposed by Peck (1969), the maximum settlement calculated using Eq. (3) is 38 mm (0.63% D), which is more than twice the measured data. This is consistent with the findings by Attewell and Farmer (1974), who also observed that the method proposed by Peck (1969) overestimates the maximum settlement for tunnelling in sand.

To predict the surface settlement above twin tunnels, Attewell et al. (1986) suggested summing the Gaussian curves induced by two tunnels. In this study, the best-fitted Gaussian curve is deduced from excavation of the first tunnel, as shown in Fig. 5a. Incremental settlement due to the second tunnelling is assumed the same as that during the first tunnel excavation. Superimposed curve based on the two Gaussian curves are also shown in the figure. It can be seen that the combined settlement curve fits quite well with the measured values at the end of the second excavation, except that settlement above the shoulder of the first tunnel.

Fig. 5b shows the measured surface settlement profiles in Test SS. After excavation of the first tunnel, a maximum settlement of 0.50% D occurred above the centerline of the first tunnel. After excavation of the second tunnel, the location of maximum surface settlement shifted to above the centerline of the second tunnel and the measured maximum value was 0.67% D . By fitting a Gaussian curve to the measured surface settlement profile after the construction of the first tunnel in Test SS, the fitted K value was found to be 0.39, consistent with that in Test TT. Similarly, by summing the two best-fitted Gaussian curves, the resulting settlement distribution is also included for comparison in Fig. 5b. The maximum settlement obtained from the summation of the two fitted curves was located above the centerline of the twin tunnels. Moreover, the measured settlement was 16% larger than the combined maximum value. It is evident that the incremental maximum settlement induced by the excavation of the second tunnel was larger than that induced by the first tunnel. Addenbrooke (1996) and Chapman et al. (2007) also found that the incremental surface settlement induced by the second tunnel is larger than that induced by the first tunnel when C/D of twin tunnels is larger than 3.0, which is higher than Test TT in this study. However, it should be noted that volume loss in each individual tunnel was not controlled in their studies. On the contrary, this study simulates tunnelling by controlling the volume loss to be 1% in all tests. This might be the reason why the magnitudes of incremental settlements induced by the twin tunnelling are close in Test TT.

Comparing the measured surface settlements in Tests TT and SS, it can be observed that the maximum surface settlement in Test TT (i.e., 0.35% D) was substantially smaller than that in Test SS (i.e., 0.67% D). This was because C/D (=1.5) the twin tunnels in Test SS was smaller than that in Test TT (C/D = 2.7). Mair et al. (1993) reported that the maximum surface settlement above one tunnel is inversely proportion to the depth of the tunnel for a given volume loss, tunnel diameter and constant value of K . Based on this study, it is evident that the surface settlement induced by twin tunnelling also decreases with increasing C/D ratio.

3.3. Pile settlement and apparent loss of pile capacity due to tunnelling

Fig. 6 shows the development of the normalized pile settlement (S_p) during each tunnel construction stage. Location of the tunnel at any stage is indicated by the distance between tunnel face to the centerline of the pile (y). Both the measured S_p and the distance from the tunnel face to the centerline of the pile (y) were normalized by the tunnel diameter (D).

In Test T, as the tunnel face advanced at a depth of C/D = 2.7 from y/D = -0.75 to -0.25, a pile settlement of 0.04% D was

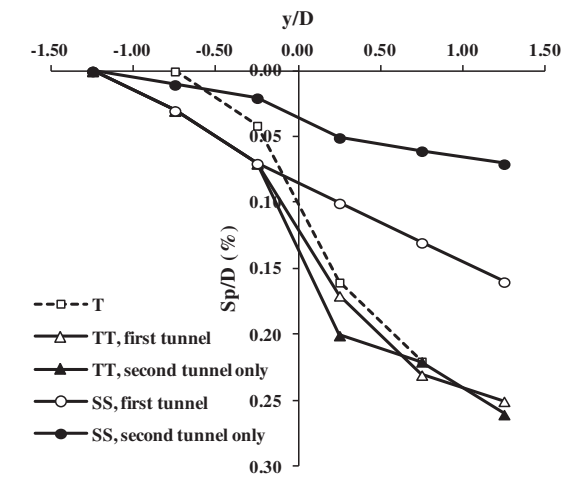


Fig. 6. Pile settlement induced by excavations of twin tunnels.

induced. A significant increase in pile settlement (0.12% D) occurred when the tunnel face advanced from y/D = -0.25 to 0.25. When the tunnel face reached y/D = 0.75, the pile settlement increased to 0.22% D (1.7% of the pile diameter). About 55% of the pile settlement was induced when the tunnel face was between y/D = -0.25 and 0.25.

In Test TT, it can be seen that the development of the pile settlement during each tunnel construction stage was very similar, in terms of the pile settlement profile and magnitude, to that observed in Test T. Significant increases in pile settlement also occurred when the tunnel face was between y/D = -0.25 and 0.25. When the face of either tunnel advanced from y/D = 0.75–1.25, the pile settlement only increased from 0.22% D to 0.25% D (1.9% of the pile diameter). About 90% of the pile settlement induced by each tunnel occurred when the face of each tunnel was between y/D = -0.75 and 0.75. Thus, the tunnelling influence zone of pile settlement was identified to be between y/D = -0.75 and 0.75. At C/D = 2.7, surprisingly the excavation of the first tunnel had almost the same effects on the pile settlement as the excavation of the second tunnel. It may suggest that each individual tunnel construction induced limited plastic strains around the pile toe. This implies that soil around the pile toe remains almost "elastic". Hence, the influence of the second tunnelling on pile settlement is almost the same as that resulted from the first tunnel.

In Test SS, the induced settlement increased almost linearly as the excavation of the first tunnel progressed at C/D = 1.5. After the excavation of the first tunnel, a pile settlement of 0.15% D (1.1% of the pile diameter) was measured. The induced pile settlement due to the first tunnel in this test was 40% less than that due to the first tunnel in Test TT. Based on their centrifuge tests, Lee and Chiang (2007) also reported that pile settlement induced by tunnelling near the mid-depth of pile shaft is smaller than that induced by tunnelling near the pile toe. This is because the load transfer mechanisms of the two cases are different (to be discussed in detail later). The pile settlement due to the excavation of the second tunnel in this study was 0.07% D (0.5% of the pile diameter), which was only about 47% of that due to the first tunnel. This may be because a significant amount of the vertical load applied to the pile was transferred downwards to the pile toe after the excavation of the first tunnel. Therefore, the effects of the construction of the second tunnel on pile settlement were smaller than those of the construction of the first tunnel. By comparing the measured results between Tests TT and SS, it is evident that the pile settlement induced by twin tunnelling is closely related to the relative location of a tunnel to the pile.

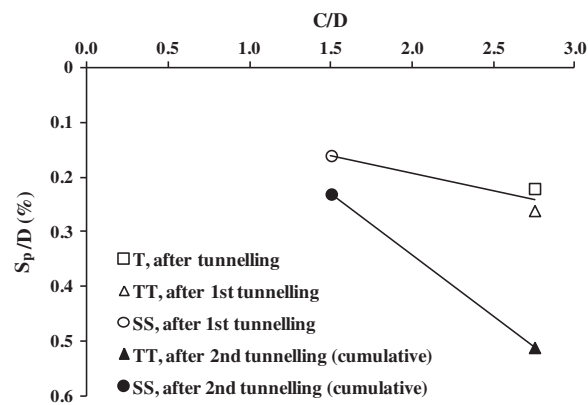


Fig. 7. Pile settlement induced by tunnelling at different C/D ratios.

Fig. 7 shows the normalized pile settlement induced by tunnelling at different C/D ratios. Open symbols denote pile settlements induced by the first tunnel, whereas solid symbols are cumulative pile settlements induced by both tunnels. After excavating the first tunnel, the pile settlement was about $0.15\%D$ for $C/D = 1.5$ in Test SS, whereas the pile settlements were about $0.23\%D$ for $C/D = 2.7$ in Test T and Test TT. It is clear that tunnelling near the pile toe induced 1.5 times of the pile settlement than tunnelling at the mid-depth of the pile shaft. After the excavation of the twin tunnels in Tests TT and SS, the cumulative pile settlement increased to $0.23\%D$ for $C/D = 1.5$ in Test SS and to $0.50\%D$ for $C/D = 2.7$ in Test TT. It is evident that twin tunnelling near the pile toe induced about 2.2 times of pile settlement than tunnelling at the mid-depth of pile shaft.

Since pile capacity is often interpreted using settlement criteria, the induced pile settlement due to tunnelling can be considered as an apparent loss of pile capacity (ALPC). Before tunnel excavation, pile settles 12 mm due to the initial applied working load (1.92 MN). An additional pile head settlement of 15 mm ($0.24\%D$) is induced due to tunnelling in Test T (see Fig. 6). By using the load-settlement relationship shown in Fig. 4, a total pile settlement of 27 mm may be regarded as an equivalent load of 2.49 MN applied to the pile. Thus, the increase in equivalent pile load can be calculated to be 0.57 MN (i.e., 2.49–1.92 MN) due to the tunnel excavation. Since the ultimate load capacity of the pile was 2.88 MN as obtained from the load settlement curve using the displacement-based failure criterion proposed by Ng et al. (2001a), it can be considered that an ALPC of 20% occurred due to the tunnel excavation. The ALPC was about 21% after excavating the first tunnel in Test TT, but it increased to about 36% after the second tunnel was constructed. In Test SS, the ALPCs were about 14% and 20% after the first and second tunnels were constructed, respectively. The ALPCs suggest that the serviceability limit state of the pile after tunnelling should be considered.

3.4. Axial forces along the pile

Fig. 8a shows the measured axial force along the pile in Test T. The depth (z) was normalized by the tunnel diameter. Before the tunnel face reached the pile (i.e., $y/D = -0.25$), no significant change in axial force was recorded. As the tunnel face reached the pile toe (i.e., $y/D = 0.25$), the axial force along the pile decreased. This may imply that the shaft resistance of the pile was further mobilized when the pile settled more than the surrounding soil. This is consistent with the significant pile settlement in Fig. 6. The maximum reduction in axial force occurred at $z/D = 2.0$ and the magnitude of maximum reduction was 119.8 kN (i.e., 6.2% of the working load). Although the end bearing resistance was not mea-

sured at the pile toe directly in this study, the measured axial force at $z/D = 3.1$ (0.6 m above the toe of the 19.6 m pile, as shown in Fig. 1) may be used to deduce the variation of end bearing resistance due to tunnelling. The measured axial force at $z/D = 3.1$ decreased as the tunnel face reached the pile toe. This revealed that there was a reduction in toe resistance due to stress relief which resulted from the 1% volume loss during tunnelling.

As the tunnel face passed the pile (i.e., $y/D = 0.75$), the axial force along the pile increased. It can be observed that the maximum reduction in axial force occurred when tunnel face finally reached the piles. The magnitude of maximum reduction in axial force cannot be captured in plane strain model tests. This illustrates the importance of carrying out three-dimensional model tests.

Fig. 8b shows the measured axial forces along the pile in Test TT. The development of axial force due to the first tunnelling was consistent with that in Test T. As expected, the maximum reduction in axial force also occurred when the first tunnel finally reached the pile (i.e., $y/D = 0.25$). As the excavation of the first tunnel continued to a distance of $y/D = 1.25$ away from the pile, the axial force almost reduced to the value before tunnel excavation.

When the second tunnel was being excavated, the maximum reduction in axial force was 353.1 kN at $z/D = 1.9$. The reduction was more than 197% larger than that caused by the excavation of the first tunnel (118.6 kN). After the excavation of the second tunnel, the final reduction in axial force decreased to 75% of its maximum value. This illustrates the complex load transfer among the soil, the pile and the tunnels during tunnelling which could only be captured in three-dimensional simulations.

Fig. 8c shows the axial forces along the pile in Test SS. In contrast to the reduction in axial forces measured in Tests T and TT, the axial force in the pile increased during the first tunnelling at the mid-depth of the pile (i.e., $z/D = 2.0$). The maximum increase in axial force recorded occurred at $z/D = 1.55$ above the first tunnel when its face reached $y/D = 1.25$. When the second tunnel was being constructed, the measured axial force continued to increase but at a reduced rate until the end of tunnel construction. The final maximum recorded increase in axial force was 423.2 kN (22% of the working load), which was 32% larger than that measured at the end of the first tunnel (320.0 kN or 16.7% of the working load).

By inspecting the distributions of axial force closely, it can be seen that the axial force increased at depths above the tunnels. This suggests that there was a decrease in shaft resistance caused by downward soil movement and also by the reduction in confining stress due to the 1% volume loss from each tunnel excavation. In contrast to the induced axial force above $z/D = 1.5$, the induced axial force below $z/D = 1.5$ decreased with depth. This implies that there was an increase in shaft resistance below $z/D = 1.5$ when the pile settled during tunnel construction as shown in Fig. 6. The measured axial force at $z/D = 3.1$ (near the toe) increased by 125.7 kN (i.e., 6.5% of the working load) at the end of the construction of the first tunnel.

3.5. Shaft resistance and load transfer mechanisms

Fig. 9a shows the average shaft resistance along the pile in Test T and Test TT. Each pile shaft is divided into two parts: the upper portion of pile shaft above the depth of tunnel crown and the lower portion below tunnel crown. Based on the axial force measured using strain gauges, the average unit skin friction (f) may be calculated as follows:

$$f = \frac{\Delta Q}{pl} \quad (4)$$

where ΔQ is the difference between measured axial loads from any two consecutive strain gauges, l is the length of each portion, and p

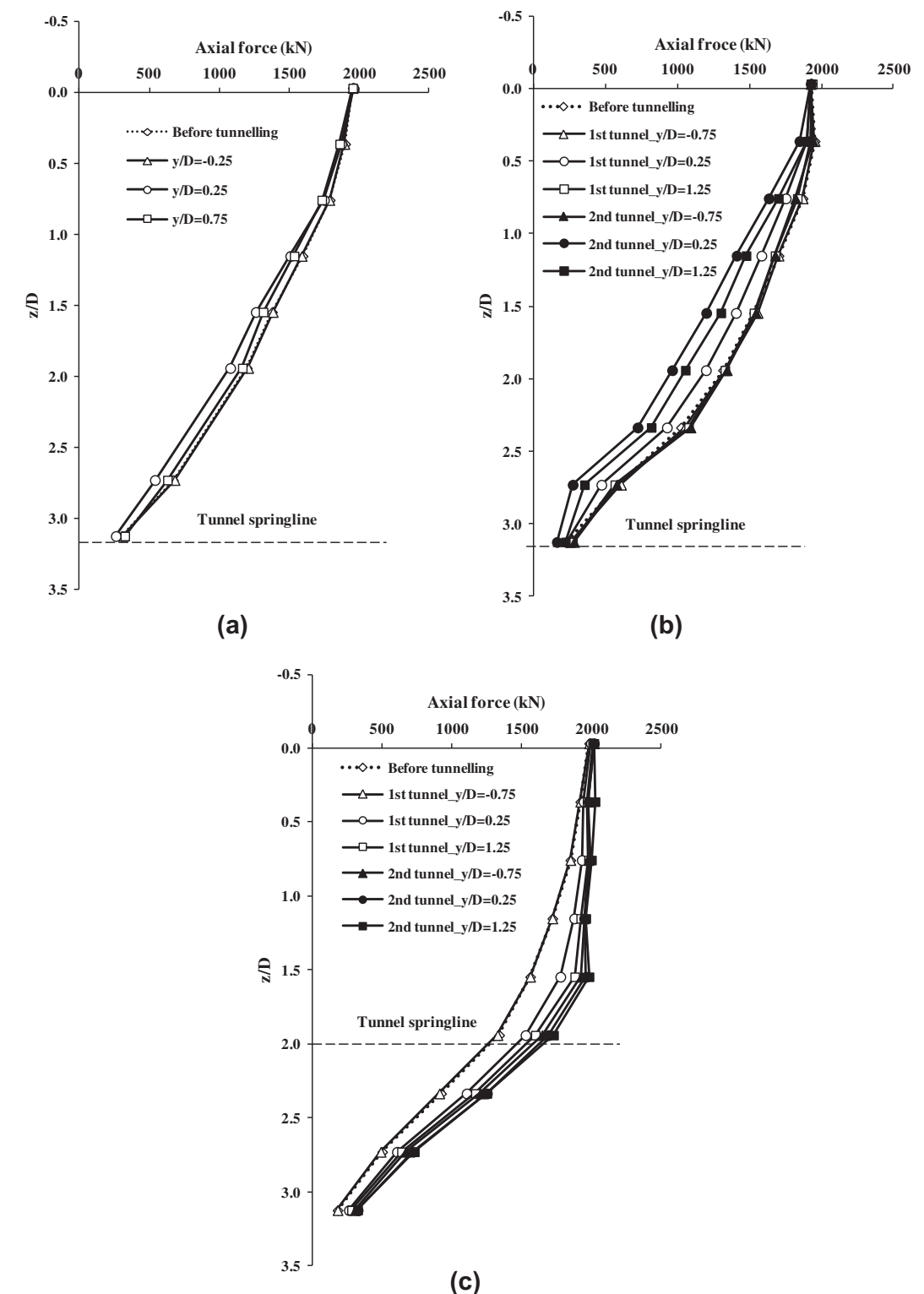


Fig. 8. Axial forces of pile at various tunnelling stages: (a) Test T; (b) Test TT; (c) Test SS.

is the perimeter of the pile. In this way, load transfer mechanism of the pile can be clearly illustrated. In Test T, as the tunnel face advanced from $y/D = -0.75$ to -0.25 , no significant change in shaft resistance was observed. However, as the tunnel face further

advanced from $y/D = -0.25$ to 0.25 , the average shaft resistance of the pile below the tunnel crown (i.e., $z/D > 2.7$) decreased significantly and that above the tunnel crown (i.e., $z/D < 2.7$) increased significantly. Due to reduction in confining stress induced by tunnel

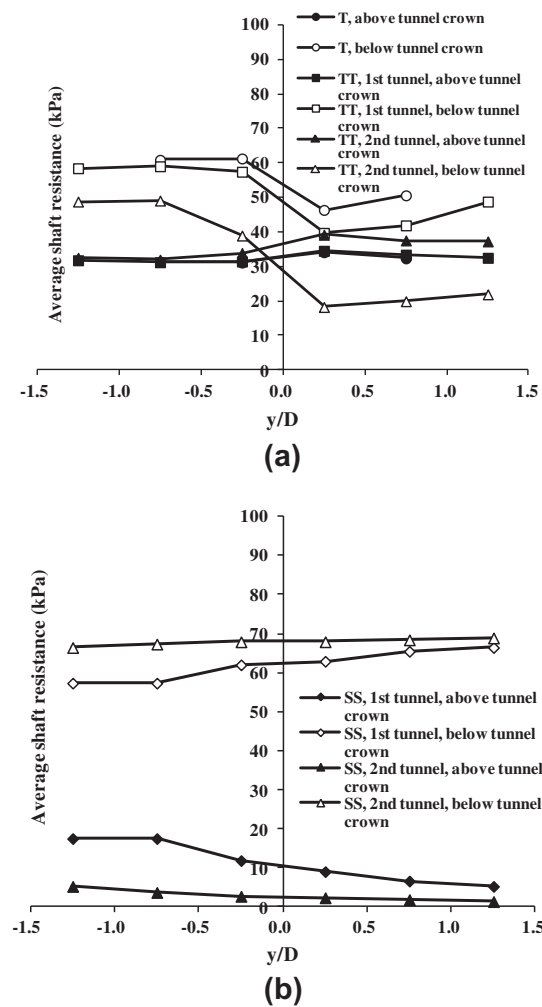


Fig. 9. Average shaft resistance along pile: (a) Test T and Test TT; (b) Test SS.

excavation, the end bearing resistance and shaft resistance of the pile at depths below the tunnel crown (i.e., $z/D > 2.7$) was reduced. In order to maintain vertical equilibrium, the pile had to settle more than the surrounding soil to mobilize shaft resistance at the upper portion of the pile shaft. This caused an increase in load taken by the upper portion and is called upward load transfer.

As the tunnel face passed the pile (i.e., as it advanced from $y/D = 0.25-0.75$), the shaft resistance of the pile above the tunnel crown (i.e., $z/D < 2.7$) decreased whereas that below the tunnel crown (i.e., $z/D > 2.7$) increased. Due to the downward soil movement and the decrease in normal stress acting on the pile induced by tunnel excavation, the shaft resistance decreased along the pile above the tunnel crown (i.e., $z/D < 2.7$). To maintain the vertical equilibrium, the shaft resistance along the pile below the tunnel crown (i.e., $z/D > 2.7$) and the end bearing resistance increased as shown in Fig. 8c. The decrease of pile load from the upward portion resulted in an increase of load in the lower portion of the pile for maintaining the vertical equilibrium. This is called downward load transfer. This is in contrast to the load transfer mechanism when tunnel face was close to the pile ($y/D = -0.25$ and 0.25). As a result, the axial force increased when the tunnel face passed the pile and advanced from $y/D = 0.25-0.75$. Therefore, the maximum reduction in axial force occurred when the tunnel face reached the pile as shown in Fig. 8. This is due to the two distinct load transfer mechanisms.

In Test TT, during the excavation of the first tunnel, the development of average shaft resistance above and below the tunnel crown was consistent with that in Test T. Two types of load transfer can again be observed. When the second tunnel was being excavated, the reduction in average resistance below the tunnel crown was larger than that in the excavation of the first tunnel. This is because part of the applied working load had been transferred to the lower part of the pile after the excavation of the first tunnel, as illustrated in Fig. 8b.

Fig. 9b shows the average shaft resistance along the pile in Test SS. Unlike in Test TT, only downward load transfer was observed in Test SS. During the excavation of the first tunnel, the average shaft resistance decreased significantly above the tunnel crown (i.e., $z/D < 1.5$) and increased below the tunnel crown (i.e., $z/D < 1.5$). Because vertical equilibrium of pile can be achieved by transferring the load taken by the upper part of the pile to the lower part of the pile, settlement of pile was relatively small compared with that when the tunnel face was near the pile toe as illustrated in Fig. 6. This is consistent with the centrifuge results reported by Lee and Chiang (2007).

When the second tunnel was being excavated, the average shaft resistance decreased above the tunnel crown (i.e., $z/D < 1.5$) and increased below the tunnel crown (i.e., $z/D < 1.5$), similar to that when the first tunnel was being excavated. At the end of the construction of the two tunnels, the mobilized shaft resistance of the pile was significantly reduced to almost zero above the crown of each tunnel. The change in average shaft resistance due to the excavation of the second tunnel was much smaller than that due to the excavation of the first tunnel. This is consistent with the measured pile settlement results shown in Fig. 6. The ALPC induced by the excavation of the second tunnel (6%) was only 43% of that induced by the first tunnelling (14%). After the excavation of the first tunnel, a significant amount of applied working load was transferred to the pile shaft below the tunnel crown and the pile toe. Thus, the effect of the second tunnel at the same depth was smaller. Clearly, the three-dimensional load transfer mechanism for twin tunnelling near the pile shaft is different from that for twin tunnelling near the pile toe. A pile suffers significant settlement when an upward load transfer is observed, but it experiences smaller settlement when the load transfer is downward. In this study, the ALPC for twin tunnelling near the pile toe (36%) was 1.8 times of that for tunnelling near the mid-depth of pile shaft (20%), as illustrated in Fig. 6.

3.6. Induced bending moments in the pile

Fig. 10a shows the measured tunnelling induced bending moment along the pile in Test T and Test TT. Bending moments were taken to be positive if tensile stress was induced at the side facing the first tunnel. In Test T, the maximum tunnelling-induced bending moment occurred near the tunnel crown (i.e., $z/D = 2.7$) with a magnitude of 61.5 kN m, which was 7.7% of the bending moment capacity of the pile ($M_{yield} = 800$ kN m). In Test TT, the maximum bending moment occurred near the crown of the first tunnel (i.e., $z/D = 2.7$) after its excavation. The maximum induced bending moment was 84.3 kN m (10.5% of M_{yield}). After the excavation of the second tunnel, the maximum bending moment decreased to 70.8 kN m (8.9% of M_{yield}). Centrifuge test results reported by Loganathan et al. (2000) are also included in the same figure for comparison. The maximum bending moment also occurred near the tunnel crown based on their test results. The bending moment at $z/D < 2.0$ in this study is different from that reported by Loganathan et al. This may be because the pile head in this study was constrained by the hydraulic jack. The general profiles of bending moment are similar though.

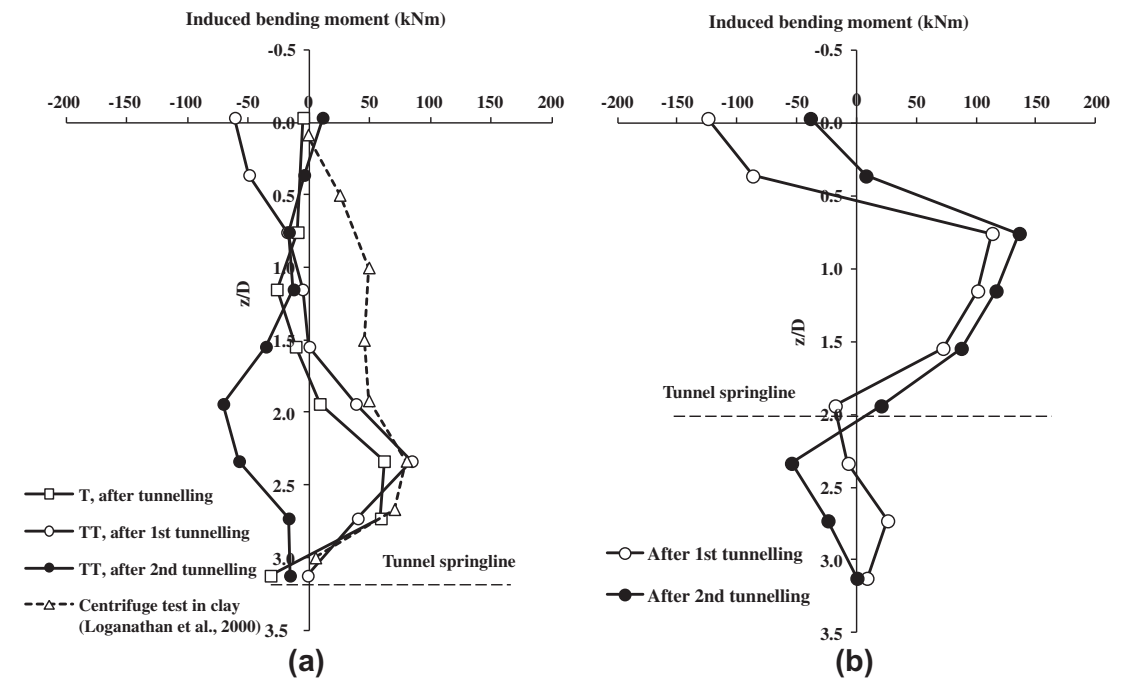


Fig. 10. Tunnelling-induced bending moment on pile: (a) Test T and Test TT; (b) Test SS.

Fig. 10b shows measured tunnelling induced bending moment along the pile in Test SS. After the first tunnel was excavated, the maximum bending moment occurred above the tunnel crown (i.e., $z/D = 0.8$). The magnitude is 113.3 kN m (14.2% of M_{yield}). A bending moment of 38.7 kN m occurred near the ground surface. This may be also due to constrain of the hydraulic jack. After the second tunnelling, the maximum bending moment was 136.0 kN m (17.0% of M_{yield}). It is the maximum value in all the three tests. Therefore, it can be concluded that the induced bending moment to the pile by twin tunnelling is relatively insignificant.

4. Summary and conclusions

A series of centrifuge model tests were carried out to investigate the effects of twin tunnel construction on an existing single pile in dry sand. In each centrifuge model test, two tunnels were simulated three-dimensionally one after the other in-flight. Based on the test results, the following conclusions may be drawn:

- The settlement of a pile induced by twin tunnelling is closely related to the depth of each tunnel relative to the pile. Near the pile toe (i.e., Test TT), the excavation of the first tunnel results in a pile settlement of about 1.9% of the pile diameter. The magnitude of incremental pile settlement due to the construction of the second tunnel only is about the same. Based on the displacement-failure load criterion proposed by Ng et al. (2001a), the apparent loss of pile capacity (ALPC) is about 21% after the construction of the first tunnel construction, and increases to about 36% (cumulative) after the construction of the second tunnel.
- For twin tunnelling near the mid-depth of the pile shaft (i.e., Test SS), the pile settlement induced by excavating the first tunnel is 1.1% of the pile diameter, which is only about 60% of that induced by the first tunnel constructed near the toe in Test TT. Due to the load transfer from the upper to lower part of the pile after the construction of the first tunnel, the construction of the second tunnel (also near

the pile shaft) induces a much smaller pile settlement of only 0.5% of the pile diameter. The ALPCs are about 14% and 20% after the excavation of the first and second tunnels, respectively.

- The pile settlement induced by twin tunnelling is closely related to C/D ratios (cover-to-diameter ratio) of tunnels and the relative location of a tunnel to the pile. The cumulative pile settlement due to tunnelling near the toe is about 2.2 times of that due to tunnelling near the mid-depth of the pile shaft.
- For construction of each tunnel near the pile toe, two distinct load transfer mechanisms, i.e., an upward first and then a downward load transfer can be identified in Tests T and TT. An upward load transfer is identified when a tunnel face approaches to within $0.25D$ of the pile. Due to the reduction in confining stress as a result of the approaching tunnel near the toe, both the shaft resistance near the toe and the end bearing resistance of the pile decrease. As a result, a larger shaft resistance is mobilized in the upper half of the pile (or upper load transfer) while the pile settles to maintain the vertical equilibrium under the applied pile load. On the contrary, a downward load transfer is observed after the tunnel face has passed the pile by a distance of $0.25D$. The shaft resistance along the upper portion of the pile decreases due to downward soil movement and stress relief induced by tunnelling, resulting in an increase in the shaft resistance along the lower portion of the pile and in the end bearing resistance so that the vertical equilibrium of the pile can be maintained. Due to the two distinct types of load transfer, the maximum reduction in axial force occurs when a tunnel face reaches the pile (in Test TT).
- When each tunnel is excavated near the mid-depth of the pile shaft (in Test SS), only a downward load transfer can be identified. The shaft resistance along the upper half of the pile decreases whereas the shaft resistance along the lower half of the pile increases as tunnel advances. However, there is an increase of 320 kN and 423 kN (i.e., equivalent to

17% and 22% of the working load) in the pile axial force above the crown after the construction of the first and second tunnels, respectively. At the end of the construction of the two tunnels, shaft resistance of the pile is significantly reduced to almost zero above the crowns of the tunnels.

- (f) The induced bending moment due to twin tunnelling is insignificant. The maximum bending moment induced in the pile by excavation of single or twin tunnels is only about 17% of the ultimate bending moment capacity.
- (g) When C/D is 1.5, the surface settlement induced by the excavation of the second tunnel is larger than that induced by the excavation of the first tunnel. Simply predicting ground surface settlement by summing the two Gaussian curves can underestimate the actual value by up to 16%.
- (h) In this study only volume loss induced due to tunnelling is modelled. The effect of removal of soil inside of tunnel is not simulated. Since all the tests were carried out using the same method (by simulating volume loss), measured results obtained from different cases investigated are comparable and conclusions drawn from this study should not be affected.

Acknowledgements

The authors would like to acknowledge the financial support provided by the Research Grants Council of the HKSAR (General Research Fund Project No. 617608).

References

- Addenbrooke, T.I., 1996. Numerical Modeling in Stiff Clay. Ph.D. Thesis, Imperial College, London.
- Attewell, P.B., Farmer, I.W., 1974. Ground deformations resulting from shield tunnelling in London clay. *Can. Geotech. J.* 11, 380–395.
- Attewell, P.B., Yeates, J., Selby, A.R., 1986. Soil Movements Induced by Tunnelling and Their Effects on Pipelines and Structures. Chapman and Hall, New York.
- Bezuijen, A., Schrier, J.S., 1994. The influence of a bored tunnel on pile foundations. *Centrifuge 94*, Singapore, pp. 681–686.
- Chapman, D.N., Ahn, S.K., Hunt, D.V.L., 2007. Investigating ground movements caused by the construction of multiple tunnels in soft ground using laboratory model test. *Can. Geotech. J.* 44 (10), 631–643.
- Ishihara, K., 1993. Liquefaction and flow failure during earthquakes. *Géotechnique* 43 (3), 351–415.
- Jacobsz, S.W., Standing, J.R., Mair, R.J., Hahiwara, T., Suiyama, T., 2004. Centrifuge modeling of tunnelling near driven piles. *Soil Found* 44 (1), 49–56.
- Lee, C.J., Chiang, K.H., 2007. Responses of single piles to tunnelling-induced soil movements in sandy ground. *Can. Geotech. J.* 44 (10), 1224–1241.
- Lee, T.K., Ng, C.W.W., 2005. Effects of advancing open face tunnelling on an existing loaded pile. *J. Geotech. Geoenviron. Eng., ASCE* 131 (2), 193–201.
- Loganathan, N., Poulos, H.G., Stewart, D.P., 2000. Centrifuge model testing of tunnelling-induced ground and pile deformations. *Géotechnique* 50 (3), 283–294.
- Mair, R.J., Taylor, R.N., Bracegirdle, A., 1993. Subsurface settlement profiles above tunnels in clay. *Géotechnique* 43 (3), 315–320.
- Mair, R.J., Taylor, R.N., 1997. Bored tunnelling in the urban environment. State-of-the-art report and theme lecture. In: *Proceedings of 14th International Conference on Soil Mechanics and Foundation Engineering*, vol. 4, Hamburg, Balkema, pp. 2353–2385.
- Mair, R.J., 2008. Tunnelling and geotechnics: new horizons. *Geotechnique* 58 (9), 695–736.
- Mroueh, H., Shahrour, I., 2002. Three-dimensional finite element analysis of the interaction between tunnelling and pile foundations. *Int. J. Numer. Anal. Methods Geomech.* 26, 217–230.
- Ng, C.W.W., Yau, T.L.Y., Li, J.H.M., Tang, W.H., 2001a. New failure load criterion for large diameter bored piles in weathered geomaterials. *J. Geotech. Geoenviron. Eng., ASCE* 127 (6), 488–498.
- Ng, C.W.W., Van Laak, P.A., Tang, W.H., Li, X.S., Zhang, L.M., 2001b. The Hong Kong geotechnical centrifuge. In: *Proc. 3rd Int. Conf. Soft Soil Engineering*, pp. 225–230.
- Ng, C.W.W., Van Laak, P.A., Zhang, L.M., Tang, W.H., Zong, G.H., Wang, Z.L., Xu, G.M., Liu, S.H., 2002. Development of a four-axis robotic manipulator for centrifuge modeling at HKUST. In: *Proc. Int. Conf. Physical Modeling in Geotechnics*, St. John's Newfoundland, Canada, pp. 71–76.
- Ng, C.W.W., Zhang, L.M., Wang, Y.H., 2006. In: *Proceedings of 6th Int. Conf. on Physical Modelling in Geotechnics (TC2)*, vols. 1 and 2. Taylor & Francis.
- O'Reilly, M.P., New, B.M., 1982. Settlements above tunnels in the United Kingdom—their magnitude and prediction. In: *Proceedings of the Conference Tunnelling '82*, IMM London, pp. 173–181.
- O'Neill, M.W., Reese, R.C., 1999. *Drilled Shaft: Construction Procedures and Design Methods*. Federal Highway Administration, Washington, DC.
- Pang, C.H., 2007. The Effect of Tunnel Construction on Nearby Pile Foundation. Ph.D. Thesis, National University of Singapore.
- Peck, R.B., 1969. Deep excavation and tunnelling in soft ground. In: *Proc. 7th Int. Conf. Soil Mech. Found. Engng.*, pp. 225–290.
- Schofield, A.N., 1980. Cambridge geotechnical centrifuge operations. *Géotechnique* 30 (3), 227–268.
- Taylor, R.N., 1995. *Geotechnical Centrifuge Technology*. Blackie Academic and Professional, London.
- Weltman, A.J., 1980. *Pile Load Testing Procedures*. DOE and CIRIA Piling Development Group Rep. PG7. Construction Industry Research and Information Association, London.



Contents lists available at SciVerse ScienceDirect

Tunnelling and Underground Space Technology

journal homepage: www.elsevier.com/locate/tust



Centrifuge and numerical investigation of passive failure of tunnel face in sand

K.S. Wong^{a,*}, C.W.W. Ng^a, Y.M. Chen^b, X.C. Bian^b

^a Department of Civil and Environmental Engineering, Hong Kong University of Science and Technology, Clear Water Bay, Kowloon, Hong Kong

^b Department of Civil Engineering, Zhejiang University, 388 Yuhangtang Road, Hangzhou 310058, China

ARTICLE INFO

Article history:

Received 19 July 2011

Received in revised form 20 October 2011

Accepted 13 December 2011

Available online 9 January 2012

Keywords:

Tunnel face
Failure mechanism
Passive failure pressure
Surface displacement
Sand

ABSTRACT

Tunnelling is one of the major construction methods to sustain the increasing demand on development in cities. Although many studies have been carried out to investigate the active failure mechanism of tunnel face in sand, the study of passive failure of tunnel face is relatively rare and most of studies are analytical solutions based on the upper bound theorem. In this paper, centrifuge model tests and three-dimensional finite element analyses have been conducted to study the passive failure mechanisms of tunnel face in sand for tunnels located at cover over diameter (C/D) ratios equal to 2.2 and 4.3. Passive failure pressures of tunnel face as well as ground surface displacements were investigated in centrifuge tests. From both centrifuge and numerical investigations, it is found that for a tunnel located at C/D ratio equals to 2.2, the soil in front of the tunnel face is displaced by the advancing tunnel face while the soil further away from the tunnel face is forced upwards to the ground surface. A funnel-type failure mechanism is observed and the extent of the failure mechanism is narrower than a five-block failure mechanism commonly assumed in an existing upper bound solution. However, the calculated passive failure pressure by the upper bound solution is fairly consistent with the measured face pressure. It is observed that the funnel-type failure mechanism induces surface heaves. Both observed longitudinal and transverse heaves are well described by Gaussian distributions. For a tunnel located at C/D ratio equals to 4.3, the displacements of soil are confined around the vicinity of an advancing tunnel face and a localised failure mechanism associated with ground settlement is observed and computed. There is a large discrepancy between the localised failure mechanism and the five-block failure mechanism. The calculated failure face pressure is higher than the corresponding measured value by 50%. However, reasonable consistency can be found between measured and computed passive face pressures.

© 2011 Elsevier Ltd. All rights reserved.

1. Introduction

In cities, tunnelling has become one of the major construction methods to sustain the increasing demand on development. When a tunnel is excavated, the tunnel face pressure shall be maintained within the minimum and maximum support pressures to prevent active or passive failure at the tunnel face. The failure may endanger human life and cause catastrophic damage to the structures within the influence zone.

Over the decades, numerous theoretical and experimental studies have been performed to investigate the active failure of tunnel face (Anagnostou and Kovári, 1994, 1996; Chambon and Corte, 1994; Dias et al., 2008; Leca and Dormieux, 1990; Leca and Panet, 1988; Mollon et al., 2010; Soubra, 2002). But the study of passive failure of tunnel face is relatively rare and most of them are analytical solutions and numerical simulations (Dias et al., 2008; Leca and Dormieux, 1990; Mollon et al., 2010; Soubra, 2002; Soubra

et al., 2008). Passive failure during drilling of the 2nd Heinenroord Tunnel (Bezuijen and Brassinga, 2005) imply that passive failure at tunnel face is not a theoretical risk. It is of important to know the passive failure pressure of tunnel face to prevent the passive failure.

Leca and Panet (1988) and Leca and Dormieux (1990) used lower and upper bound theorems to predict the passive failure pressure of tunnel face in sand. For upper bound solutions, they adopted a truncated cone as the failure mechanism. It is a planar on vertical plane of symmetry running longitudinally along centreline of tunnel. Soubra (2002) improved the upper bound solutions by introducing a log spiral instead of planar on the vertical plane of symmetry. The log spiral was idealised using multiple truncated rigid cones. But only an inscribed elliptical area to the entire circular tunnel face is involved in deriving the upper bound solutions, due to the conical shape of the rigid cones used in the derivation (Mollon et al., 2010).

While existing analytical and numerical analyses provide valuable information and knowledge on passive failure of tunnel face, the problem has not been studied systematically and fully understood. In view of this, centrifuge model tests were carried out to

* Corresponding author. Tel.: +852 9673 2276/2358 0216; fax: +852 2243 0040.
E-mail addresses: wksaa@ust.hk (K.S. Wong), charles.ng@ust.hk (C.W.W. Ng), chenyunmin@zju.edu.cn (Y.M. Chen), bianxc@zju.edu.cn (X.C. Bian).

investigate passive failure of tunnel face in sand for tunnels located at cover over diameter, C/D ratios equal to 2.2 and 4.3. In addition, finite element analyses were conducted to back-analyse the centrifuge model tests and provide further information to understand the problem. This paper presents: (a) details of centrifuge model setup and test procedures; (b) details of the finite element analyses; (c) failure mechanisms and passive failure pressure of tunnel face obtained from the centrifuge model tests and finite element analyses as well as comparisons with the existing analytical solutions; and (d) the induced ground surface displacement due to tunnel face displacement obtained from centrifuge tests.

2. Centrifuge modelling

2.1. Experimental program

The centrifuge model tests were performed in the Geotechnical Centrifuge Facility (GCF) at the Hong Kong University of Science and Technology (HKUST). The geotechnical centrifuge at HKUST (Ng et al., 2001, 2004) has a rotating arm of approximately 8.4 m in diameter. The maximum modelling capacity of the centrifuge is 400g ton. It is capable of simulating an elevating gravity field over 150 times that of the earth's gravity (g) for static model.

Three tunnelling cases with different C/D ratios were carried out in saturated sand to study the passive failure of tunnel face. Tests S2 and S4 were designed to investigate the passive failure of tunnel face for tunnels located at C/D ratios equal to 2.2 and 4.3 respectively. The performance and reliability of load cells submerged in the water deteriorated over time due to water ingress. Tunnel located at C/D ratio equals to 2.2 was repeated in Test S2R using an internal load cell as described in Section 2.2 to obtain the variation of tunnel face pressure with tunnel face displacement. Some details of the centrifuge tests are given in Table 1.

2.2. Model setup

Fig. 1 shows the plan and elevation views of the centrifuge model setup. A rectangular model container of plan dimensions 1245×350 mm and depth 850 mm with a perspex viewing window in the front face was used in the centrifuge model tests. A 12.7 mm thick glass, measuring 850 mm by 714 mm, was bolted to 25.4 mm thick perspex with similar dimensions to form a composite panel. The composite panel was attached to the front face of the model container with the glass side in contact with sand. The glass served the purpose for ease of PIV control marker placement while reducing the friction between the front face and the sand. The face of the glass which was in contact with the sand formed the vertical plane of symmetry. A 25.4 mm thick aluminium plate was used to separate the sand from the loading system. The aluminium plate was braced by six aluminium struts with diameter of 41.3 mm attached to the side wall of the model container.

Fig. 2 shows the model tunnel used in the Test S2R. A tunnel lining consisted of an aluminium hollow tube, 50 mm in diameter and 200 mm long with wall thickness of 2.7 mm, which was split longitudinally along the centre plane. A hollow loading piston, 20 mm in diameter and 140 mm long was screwed to the a 60 mm long tunnel face block. A 25 mm long end block was placed

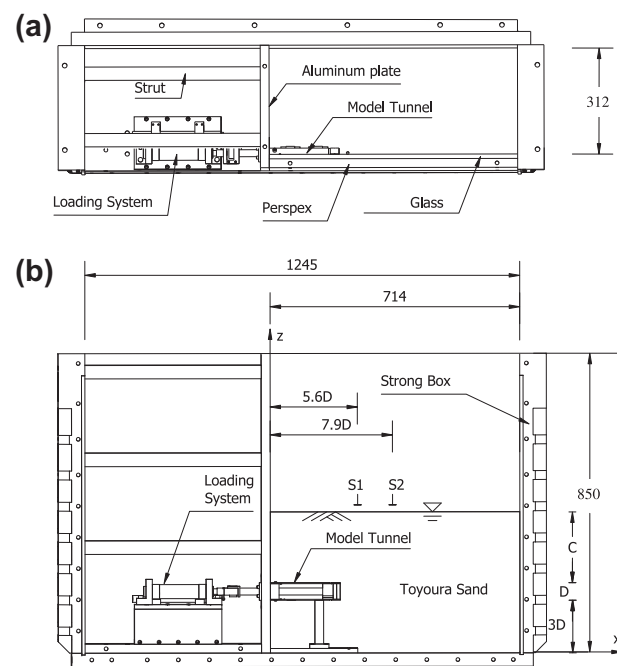


Fig. 1. Basic configuration of a centrifuge package (dimensions in mm): (a) plan view and (b) elevation view.

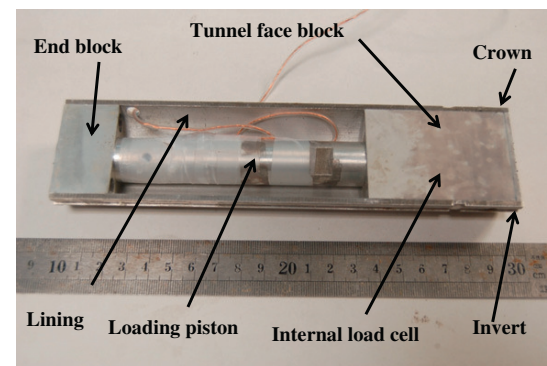


Fig. 2. Model tunnel.

at another end of the loading piston. The tunnel lining was placed on the tunnel face block and bolted to the end block.

The tunnel face block consisted of a tunnel face, an internal load cell and a sleeve. The internal load cell was made of hollow aluminium tube with semiconductor strain gauges bonded on the external surface. Epoxy coating was used to protect the strain gauges from abrasion. Full Wheatstone bridge strain gauges were arranged to compensate for temperature effects. The load cell was attached to the tunnel face and protected by the sleeve. There were two O-rings at both ends of the load cell in contact with the inner face of the sleeve. This minimised the friction between sleeve with lining/soil and glass to be transferred to the load cell. The O-rings

also served the purpose to isolate the load cell from water ingress. There was a ring of filler to separate the sleeve from the tunnel face to ensure load from the tunnel face was measured by the load cell only. The silica gel was squeezed into the hollow section of the load cell and isolated the strain gauges from water.

Model tunnel used in Tests S2 and S4 was similar to that used in Test S2R except the loading piston and tunnel face block also served as load cells with full Wheatstone bridge strain gauges bonded to its external surface and protected by epoxy coating. The performance and reliability of the load cells deteriorated over time due to water ingress.

Fig. 3 shows the loading system used in the centrifuge tests. The loading system consisted of a hydraulic actuator, mounted on an actuator support by using two L-shape brackets and connected to an oil supply system through two oil supply tubes. A linear variable differential transformer (LVDT) was fastened to the actuator support and its core was bolted to a fitting cap. The fitting cap was attached to the piston of the actuator. The actuator support was made of four 12.7 mm thick aluminium plates and bolted to a 25.4 mm thick base plate, which was mounted to the bottom of the model container. A connecting piston used to connect the loading system and model tunnel was slot to the fitting cap and secured by a L-shape fitting. The connecting piston also served as an external load cell with full Wheatstone bridge strain gauges bonded to its external surface and protected by epoxy coating.

The model tunnel was supported by an aluminium column at one end and bolted to the aluminium plate via two screws at another end as shown in Fig. 1. The connecting piston of the loading system passing through the aluminium plate was connected to the loading piston of the model tunnel. The hole on aluminium plate had a groove, fit with an elastomeric O-ring, which encircled the connecting piston to ensure watertight during the movement of the piston. Perforated drainage pipes wrapped with geotextiles were used to form a drainage system. The drainage system was placed on the bottom of the model container.

2.3. Instrumentation

In Tests S2 and S4, tunnel face pressure was given by an external load cell as shown in Fig. 3. In Test S2R, tunnel face pressure was given by an internal load cell in the tunnel face block as described in the previous section. Horizontal displacement of tunnel face was measured by LVDT attached to the actuator support.

Particle image velocimetry (PIV) and close-range photogrammetry originally developed by White et al. (2003) was used to monitor the subsurface soil displacement on the vertical plane of symmetry. The precision of the measurement is 0.1 mm. Digital images were captured using in flight camera mounting on the swinging platform. Each image was divided into soil patches and each patch represented

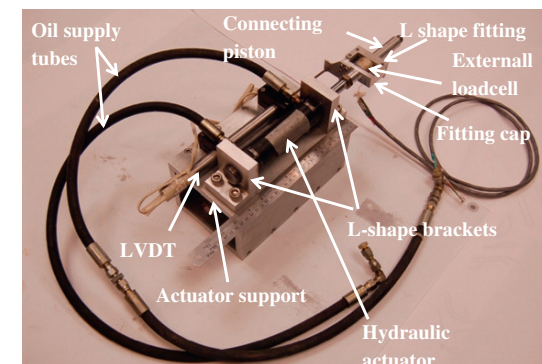


Fig. 3. Loading system.

a measurement point. The movement of soil patches between two successive images was traced based on cross-correlation. PIV can only measure the displacement in the image-space coordinates. Close range photogrammetry was used to convert the image-space coordinates to object-space coordinates. Details of PIV and close-range photogrammetry can be obtained from White et al. (2003). Longitudinal surface displacements were deduced from the PIV results. The transverse surface displacements were monitored using LVDTs at Sections S1 and S2 located at $5.6D$ and $7.9D$ respectively along the x direction as indicated in Fig. 1. For Test S2, four LVDTs were placed at Section S1. Four LVDTs were placed at Section S2 for Test S4. Four LVDTs were placed at Section S1 and three LVDTs were placed at Section S2 for Test S2R.

2.4. Model preparation

Toyoura sand used in the tests has the maximum and minimum void ratios of 0.977 and 0.597 respectively. The sand has a specific gravity of 2.65 (Verdugo and Ishihara, 1996). The sand was pluviated to the strong box through a hopper and the drop height of the sand was set as 500 mm. The relative density, D_r , of the sand sample at 100g was 67%, 56% and 63% for Tests S2, S4, and S2R respectively. The relative density and corresponding saturated unit weight of the sand sample for Tests S2, S4 and S2R are listed in Table 1.

In order to saturate the sand, aluminium cover with elastomeric O-ring was placed on top of the model container. Vacuum was applied to the sand for 2 h. Then, carbon dioxide was injected through drainage system to replace the residual air. After that, the vacuum was reapplied for another 3 h. While maintaining the vacuum, deaired water from water tank was supplied through the drainage system to the soil mass. When the water level reached required level above the ground surface of the sand sample, the saturation process was terminated. The whole saturation process required around 40 h.

2.5. Test procedures

After completion of model preparation and final check, the model container was transferred to the swinging platform. The water level was maintained at around 15 mm above the ground surface after connecting the strong box to the stand pipe on the platform. Four cameras were set up to capture photographs during centrifuge testing. Three videos were installed to monitor the test. The data logger was then set to record data at 1 Hz, and upon centrifuge spinup, photographs were taken at 150 s intervals and saved to the computer.

When the acceleration of the centrifuge reached 100g and equilibrium condition was achieved, the camera settings were changed to take photographs every 30 s. The tunnel face block was pushed toward the sand in 0.2 mm per second. The speed was chosen to ensure enough time for the water to flow into the tunnel lining so that suction was not created behind tunnel face block. The tunnel face displacement was prescribed and the corresponding face pressure was measured. After pushing the tunnel face block for a maximum displacement of 35 mm, the centrifuge was spun down. It should be noted that in actual shield tunnelling, pressure controlled is normally adopted. The measured results from centrifuge tests may not be directly applicable to the actual tunnel construction. On the other hand, pressure controlled was used in the numerical simulations described later in this paper.

3. Three-dimensional numerical modelling

3.1. Finite element mesh and boundary conditions

Three-dimensional numerical modelling were performed using Plaxis finite element code (Brinkgreve and Broere, 2004). Fig. 4

Table 1

Test program.

Test	C/D	Relative density (%)	Unit weight (kN/m^3)	Remarks
S2	2.2	67	19.2	Performance of load cells submerged in water deteriorated over time
S4	4.3	56	19.0	Performance of load cells submerged in water deteriorated over time
S2R	2.2	63	19.1	-

shows the finite element mesh used in the numerical modelling for tunnel located at C/D ratio equals to 2.2. The finite element mesh was 700 mm long, 300 mm high and 300 mm wide. For tunnel located at C/D ratio equals to 4.3, the finite element mesh was 700 mm long, 400 mm high and 300 mm wide. This is similar to the dimensions of the soil samples in the model container.

Only half of the tunnel was modelled, taking advantage of symmetry about $y = 0$ mm. 15-noded wedge elements and 8-noded plate elements were used to model the sand and the tunnel lining respectively. On the left and right boundaries of the mesh, the movement in the y direction was restrained. The movement in the x direction on the front and rear boundaries was restrained. Pin supports were applied to the base boundary to restrict movements in the x , y and z directions. The water table was located at the ground surface, with a hydrostatic initial pore-water pressure profiles. The tunnel lining and shield was submerged under water.

3.2. Constitutive models and model parameters

The response of the sand is modelled using a non-linear hardening-soil (H-S) constitutive model employed the Mohr–Coulomb failure criterion with a non-associated flow rule. The H-S model is a non-linear elastic–plastic formulation using multiple yield loci as a function of plastic shear strain and a cap to capture volumetric hardening as described by Schanz et al. (1999). Loading and unloading within the current yield surface, which is defined by a unloading and reloading modulus, E_{ur} , are assumed to be elastic. Critical state angle of friction, ϕ_{cs} , is defined by maximum angle of dilation, ψ and peak angle of friction, ϕ' according to Eq. (1a). The mobilised dilation angle, ψ_m is related to mobilised angle of friction, ϕ'_m and ϕ_{cs} as shown in Eq. (1b).

$$\sin \phi_{cs} = (\sin \phi' - \sin \psi) / (1 - \sin \phi' \sin \psi) \quad (1a)$$

$$\sin \psi_m = (\sin \phi'_m - \sin \phi_{cs}) / (1 - \sin \phi'_m \sin \phi_{cs}) \quad (1b)$$

Soil dilatancy, defined by the ratio of the plastic volumetric strain rate to the plastic shear strain rate is equal to $\sin \psi_m$. A cut-off for dilation is allowed when void ratio reaches the nominated maximum void ratio. Under triaxial condition, the model predicts a hyperbolic relationship for the drained secant Young's modulus, E , as given in Eq. (2).

$$E = 2E_{50}(1 - R_f q/q_f); \quad E_{50} = E_{50}^{ref} (\sigma'_3/p_{ref})^m \quad (2)$$

where q is the deviatoric stress; E_{50}^{ref} is the E value when q is 50% of the maximum deviatoric stress, q_f at the reference confining stress,

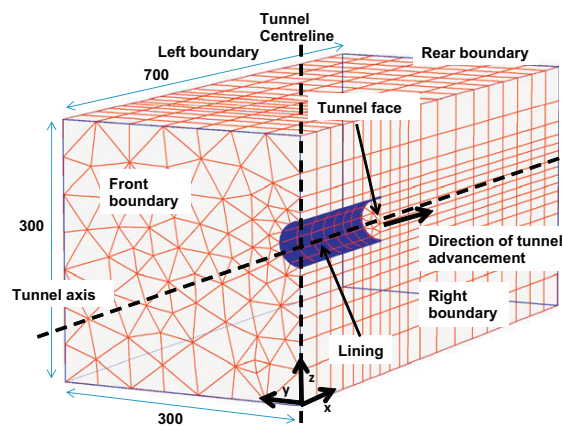


Fig. 4. Finite element mesh adopted for three-dimensional numerical modelling (dimensions in mm).

Table 2
Soil parameters used in the finite element analyses.

Parameter	Value
Saturated unit weight, γ_{sat} (kN/m ³)	19.0
Effective cohesion, c' (kPa)	1.0
Effective angle of friction, ϕ' (°)	37°
Angle of dilation, ψ (°)	7°
Effective secant modulus, E_{50} (MPa)	27
Effective unloading/reloading modulus, E_{ur} (MPa)	81
Effective oedometer modulus, E_{oed} (MPa)	27
Poisson's ratio, ν'	0.2
m	0.5
Failure ratio, R_f	0.9
At-rest earth pressure coefficient, K_0	0.5

p_{ref} ; R_f is the failure ratio and m controls the stress level dependence of the stiffness; σ'_3 is the confining stress. In this study, p_{ref} was taken as 100 kPa. Beside, effective oedometer modulus, E_{oed} which control the cap of the model is also stress level dependence.

The relative density of the sand was taken as 60%, which corresponds to a saturated unit weight, γ_{sat} of 19.0 kN/m³. According to Verdugo and Ishihara (1996), the critical state angle of friction, ϕ_{cs} for Toyoura sand is 31° under triaxial condition. In order to obtain shear strength and stiffness parameters for numerical simulations in this study, triaxial compression tests conducted by Maeda and Miura (1999) were simulated numerically. The fitted ϕ' and ψ are 37° and 7° respectively. Small cohesion, c' of 1 kPa was assigned to the soil. In the numerical simulations, E_{50} at confining stress of 100 kPa was taken as 27 MPa. E_{oed} was set as 27 MPa (Schanz and Vermeer, 1998). The unloading and reloading modulus, E_{ur} was taken as 81 MPa, which is three times of E_{50} (Brinkgreve and Broere, 2004). The Poisson's ratio of the sand was taken as 0.2. The coefficient of earth pressure at-rest was set equal to 0.5. Soil parameters used for the numerical modelling are summarised in Table 2. The tunnel lining was modelled as linear elastic material with a Young's modulus of 70×10^6 kPa, a Poisson's ratio of 0.15, and a thickness of 2.7 mm.

3.3. Numerical modelling procedures

The analysis was started by applying an acceleration of 100g to increase the gravity of the numerical model to simulate the stress state in the centrifuge test. As tunnel was assumed to be wished-in-place and submerged under water, tunnel excavation was simulated by deactivating the soil elements within tunnel excavation zone and activated the shell elements of the lining in a single step. Such a simplified modelling approach had been adopted successfully in previous studies (Li et al., 2009). In order to ensure the sand around the vicinity of tunnel face remained at at-rest condition, a constant pressure which equal to the at-rest earth pressure at the centre of tunnel face was applied to the tunnel face. Subsequently, pressure controlled boundary was adopted at the tunnel face to investigate the passive failure of tunnel face.

4. Failure mechanism

Fig. 5a shows the measured normalised displacement vectors on the vertical plane of symmetry at normalised tunnel face displacement, S_x/D of 0.8, for tunnel located at C/D ratio equals to 2.2. The corresponding normalised tunnel face pressure, $N_{\gamma m}$ is 91. The normalised tunnel face pressure following Leca and Dormieux (1990) is given by $N_{\gamma m} = \sigma'_t/\gamma D$, where σ'_t = tunnel face pressure and γ = effective unit weight of sand. The displacement vectors were obtained from the centrifuge tests using PIV analyses and normalised by tunnel face displacement. The displacement vectors illustrate that the soil in front of the tunnel face is displaced by the

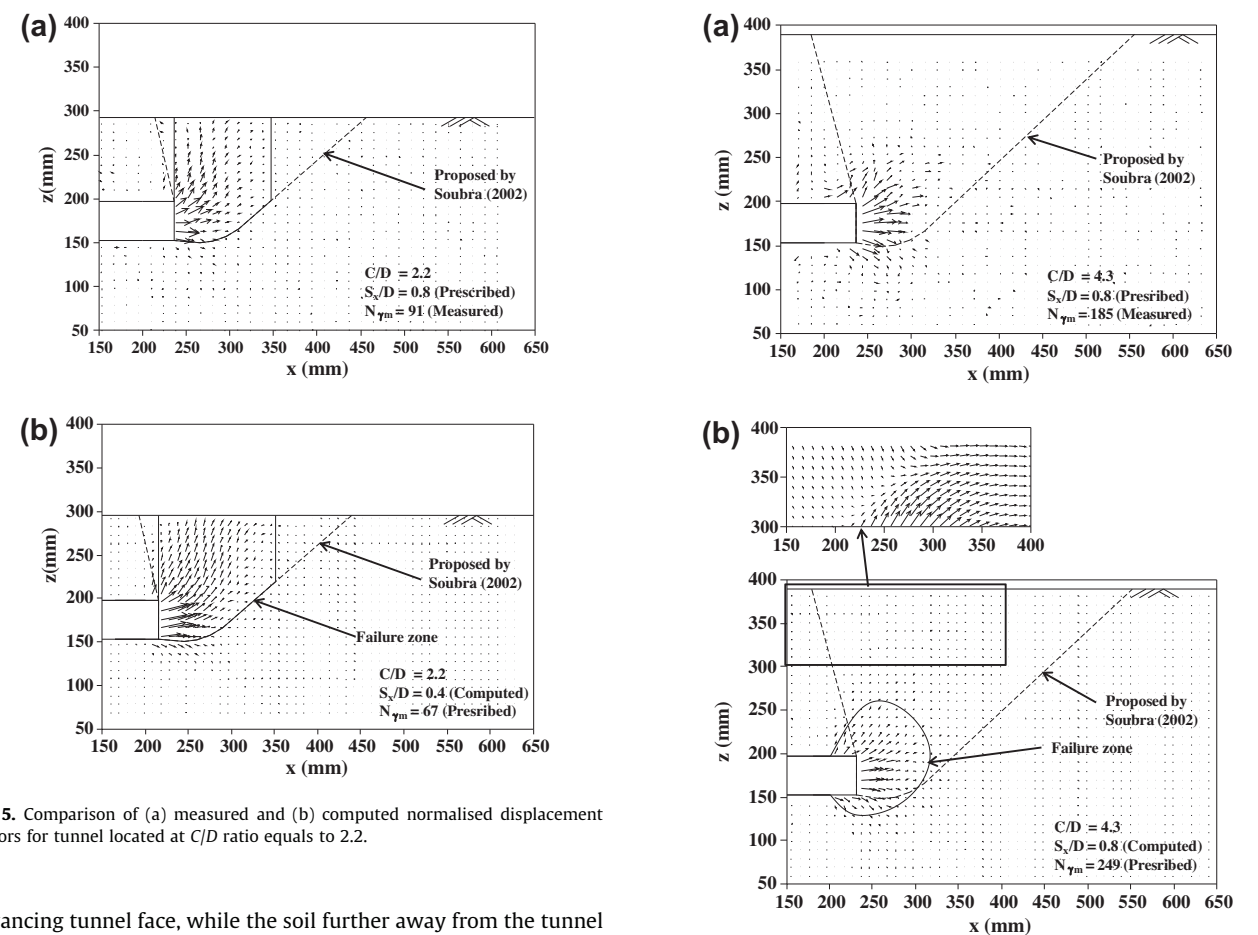


Fig. 5. Comparison of (a) measured and (b) computed normalised displacement vectors for tunnel located at C/D ratio equals to 2.2.

advancing tunnel face, while the soil further away from the tunnel face is forced upwards to the ground surface and hence the soil surface heaves. The observed failure mechanism is compared to a five-block failure mechanism (dashed lines in the figure) proposed by Soubra (2002) in obtaining upper bound solutions. The five-block failure mechanism is obtained by assuming the sand obeys normality where $\psi = \phi_{cs}$, which is rarely observed during drained failure of sand. The normality assumption may be one of the reasons that the five-block failure mechanism is wider than the observed failure mechanism. Previous studies (De Borst and Vermeer, 1984; Loukidis and Salgado, 2009; White et al., 2008) also revealed that a wider failure mechanism is obtained when the soil is more dilative. When the observed failure mechanism is idealised by solid lines, a funnel-type failure mechanism may be postulated.

Fig. 5b shows the computed normalised displacement vectors at S_x/D of 0.4 and $N_{\gamma m}$ of 67. The computed displacement vectors are localised around the tunnel face at S_x/D of 0.8 for tunnel located at C/D ratio equals to 4.3. The corresponding $N_{\gamma m}$ is 185. The soil in front of the tunnel face is displaced forwards, whereas the soil in regions located further away from the tunnel axis is forced outwards. Obviously, the observed failure mechanism illustrated by the displacement vectors is differed from a five-block failure mechanism (dashed lines in the figure) proposed by Soubra (2002).

Fig. 6a shows the measured normalised displacement vectors are localised around the tunnel face at S_x/D of 0.8 for tunnel located at C/D ratio equals to 4.3. The corresponding $N_{\gamma m}$ is 185. The soil in front of the tunnel face is displaced forwards, whereas the soil in regions located further away from the tunnel axis is forced outwards. Obviously, the observed failure mechanism illustrated by the displacement vectors is differed from a five-block failure mechanism (dashed lines in the figure) proposed by Soubra (2002).

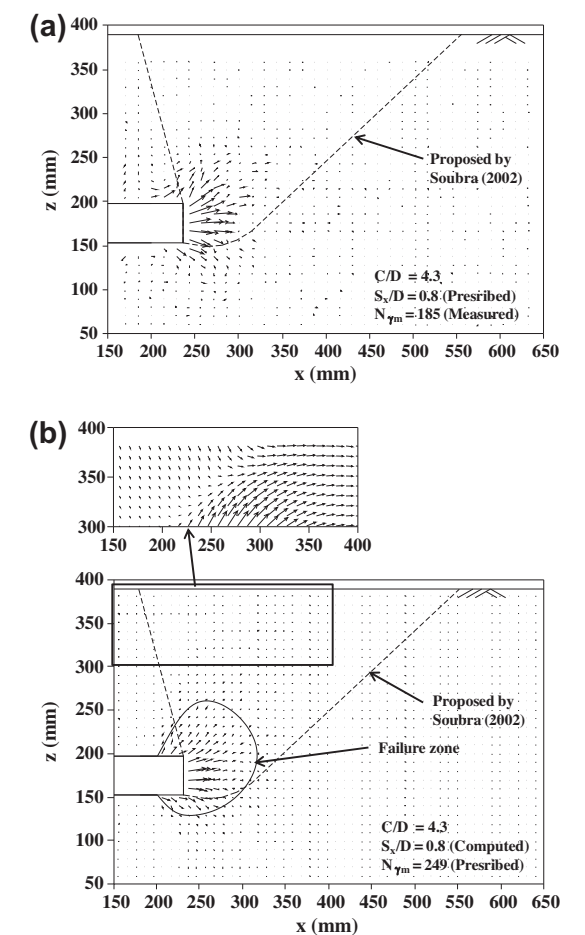


Fig. 6. Comparison of (a) measured and (b) computed normalised displacement vectors for tunnel located at C/D ratio equals to 4.3.

Fig. 6b shows the computed displacement vectors at S_x/D of 0.8 and $N_{\gamma m}$ of 249. The failure mechanism illustrated by the computed displacement vectors shows fairly close agreement with the localised failure mechanism. The finite element results reveal that the soil elements adjacent to the tunnel face reached failure. Computed failure zone is reasonably consistent with the observed displacement vectors shown in Fig. 6a. The displacement vectors at a region close to the ground surface are scaled up to 20 times for clarity. The displacement vectors illustrate surface settlements. The mobilised shear above the crown of tunnel face might drag the soil mass forwards and induce the surface settlements.

5. Passive failure pressure of tunnel face

Fig. 7 shows the variations of $N_{\gamma m}$ with S_x/D for tunnels located at C/D ratios equal to 2.2 and 4.3. For tunnels located at C/D ratio equals to 2.2, $N_{\gamma m}$ increases with S_x/D but at a reducing rate and approaches a steady state. The variation of $N_{\gamma m}$ with S_x/D for Test S2 is comparable to that obtained from Test S2R. Some of data was missing due to improper electrical gain was used in Test S2. It is observed that $N_{\gamma m}$ in Test S2 is larger than that in Test S2R. This may be reasonable as the $N_{\gamma m}$ obtained from external load cell in Test S2 was affected by the friction between tunnel face block and the lining, glass or sand. It is fortuitous that the computed pressure-displacement curve is in good agreement with the measured response. It should be noted that a displacement controlled

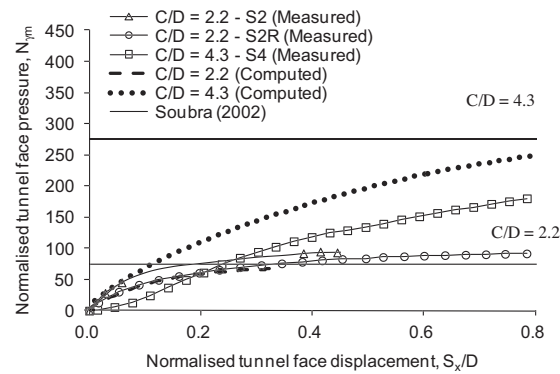


Fig. 7. Comparison of measured and computed variations of normalised tunnel face pressure with tunnel face displacement for tunnels located at C/D ratios equal to 2.2 and 4.3.

boundary was used in the centrifuge test while pressure controlled was adopted in the numerical simulation. Calculated passive failure pressure by using the upper bound solution, which were derived by Soubra (2002) are included for comparison. The calculated passive failure pressure is fairly consistent with the measured face pressure.

For tunnel located at C/D ratio equals to 4.3, the measured N_{ym} increases slowly when S_x/D is less than 0.1. Subsequently, N_{ym} increases rapidly but in a reducing rate. The computed N_{ym} increases in a reducing rate and a steady state value was not reached at S_x/D ratio equals to 0.8. The computed N_{ym} is larger than the measured one. This may be due to the presence of localised loose deposit in front of tunnel face created at 1g condition. The calculated passive failure face pressure is higher than the corresponding measured value by 50%. The discrepancy may be because the measured pressure did not reach the failure one as the pressure was still increasing. This might be also attributed to the large discrepancy between the localised failure mechanism and the five-block failure mechanism.

6. Surface displacement

It is well known that measured transverse surface settlements due to tunnelling may be represented by a Gaussian distribution as suggested by Peck (1969). The Gaussian distribution can be described by:

$$\Delta = \Delta_{\max} \exp(-s^2/2i^2) \quad (3)$$

where Δ is the transverse surface settlement; Δ_{\max} is the maximum transverse surface settlement on the tunnel centreline; s is the horizontal distance from the tunnel centreline; and i is the point of inflection of the settlement trough. The point of inflection is equal to Kz_0 , whereas z_0 is depth of tunnel. The relation was proposed by O'Reilly and New (1982) and validated using field data by (Lake et al., 1992; Mair and Taylor, 1997). Mair and Taylor (1997) found that the K values vary from 0.25 to 0.45 for sand and gravel. Instead of fitting settlement profiles, Gaussian distribution is attempted to fit measured heaves in this study.

Fig. 8a shows the measured normalised soil displacements, Δ/D at $0.6D$ below the ground surface on the vertical plane of symmetry for tunnels located at C/D ratios equal to 2.2 and 4.3. The soil displacements along the longitudinal direction were obtained from the PIV analyses. Gaussian distributions are obtained by setting K equal to 0.27 and the Δ_{\max} are deduced from the measured heaves. For tunnel located at C/D ratio equals to 2.2, heaves increase with S_x/D . This is consistent with the funnel-type failure mechanism, which extends to the ground surface. The measured heaves are

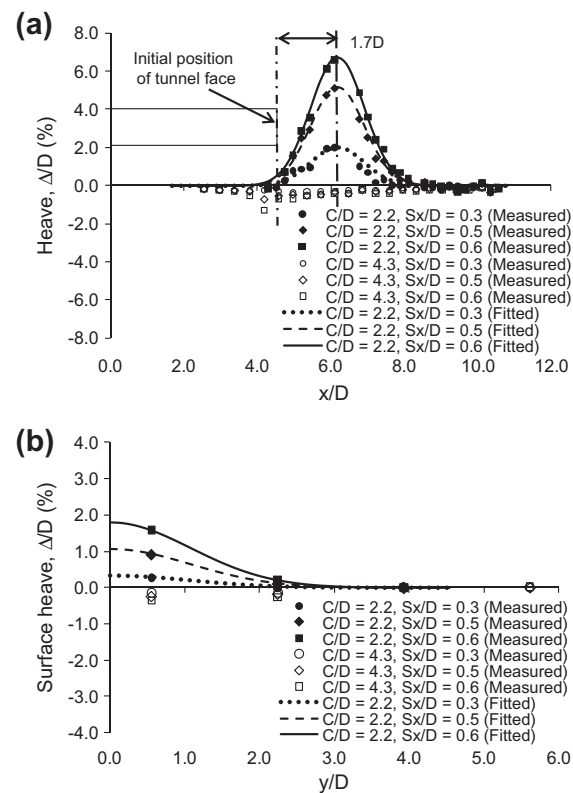


Fig. 8. Measured heaves at different tunnel face displacement for tunnels located at C/D ratios equal to 2.2 and 4.3: (a) longitudinal direction and (b) transverse direction.

well described by the Gaussian distributions. The extent of the heaves and location of the maximum heave remain around $4D$ and $1.7D$ respectively from the initial position of tunnel face for different S_x/D . For tunnel located at C/D ratio equals to 4.3, instead of heaves, settlements are induced as S_x/D is increased. This is consistent with the localised failure mechanism, which induces surface settlement as shown in Fig. 6b. The maximum settlement are located near to the initial position of tunnel face.

Fig. 8b illustrates the measured normalised transverse surface heaves induced by tunnel face displacements at a section located at $3.4D$ in front of the initial position of the tunnel face. The surface heaves were measured by using LVDTs. For tunnel located at C/D ratio equals to 2.2, heaves increase with S_x/D and the extent of heave remains at $3D$ from the longitudinal tunnel axis. Gaussian distributions are fitted to the transverse surface heaves. The fitted values of Gaussian distributions are obtained by using K equal to 0.4. The transverse surface heaves are well described by the Gaussian distributions. For tunnel located at C/D ratio equals to 4.3, settlements are induced and the extent of the settlements is around $3D$ from the tunnel axis.

7. Conclusions

The results of centrifuge model tests and finite element back-analyses investigating the passive failure of tunnel face in sand are reported. The soil failure mechanisms and passive failure pressures of tunnel face are described and discussed. In addition, the induced ground surface displacements due to the increase in tunnel face displacement are also reported.

For both centrifuge and numerical investigations, it is found that for tunnel located at C/D ratio equals to 2.2, the soil in front

of the tunnel face is displaced by the advancing tunnel face. The soil further away from the tunnel face is forced upwards to the ground surface and hence the soil surface heaves. A funnel-type failure mechanism is observed and the extent of the funnel-type failure mechanism is narrower than a five-block failure mechanism commonly assumed in the existing upper bound solution. However, the calculated passive failure pressure by the upper bound solution is fairly consistent with the measured face pressure. Besides, the computed pressure-displacement curve is in good agreement with the measured response. It is found that the extent of longitudinal surface heaves and the location of maximum heave remain around $4D$ and $1.7D$ respectively in front of the initial position of tunnel face at different S_x/D ratio. The extent of transverse surface heaves remains at $3D$ from longitudinal tunnel axis for different S_x/D ratio at a section, which is $3.4D$ in front of the initial position of tunnel face. Both observed longitudinal and transverse heaves are well described by Gaussian distributions.

For a tunnel located at C/D ratio equals to 4.3, the displacements of soil are confined around the vicinity of an advancing tunnel face and a localised failure mechanism associated with ground settlements is observed and computed. There is a large discrepancy between the localised failure mechanism and the five-block failure mechanism. The calculated failure face pressure is higher than the corresponding measured value by 50%. However, reasonable consistency can be found between measured and computed passive face pressures.

Acknowledgements

The authors would like to acknowledge the Research Grant 617608 from the Research Grants Council of HKSAR, the National Science Foundation of China for awarding the second author the Overseas and Hong Kong, Macau Young Scholars Collaborative Research Fund (No. 50629802) and financial support from the National Basic Research Program of China (Research Grant: 2007CB714001).

References

- Anagnostou, G., Kovari, K., 1994. The face stability of slurry-shield-driven tunnels. *Tunnelling and Underground Space Technology incorporating Trenchless* 9 (2), 165–174.
- Anagnostou, G., Kovari, K., 1996. Face stability conditions with earth-pressure-balanced shields. *Tunnelling and Underground Space Technology* 11 (2), 165–173.
- Bezuijen, A., Brassinga, H.M., 2005. Blow-out pressures measured in a centrifuge model and in the field. *Tunnelling*. In: Bezuijen, A., Lottum, H.v. (Eds.), *A Decade of Progress – GeoDelft 1995–2005*. Taylor & Francis, London, pp. 143–148.
- Brinkgreve, R.B.J., Broere, W., 2004. PLAXIS 3D Tunnel Version 2, PLAXIS bv, Netherlands.

- Chambon, P., Corte, J.F., 1994. Shallow tunnels in cohesionless soil: stability of tunnel face. *Journal of Geotechnical Engineering – ASCE* 120 (7), 1148–1165.
- De Borst, R., Vermeer, P.A., 1984. Possibilities and limitations of finite elements for limit analysis. *Geotechnique* 34 (2), 199–210.
- Dias, D., Janin, J. P., Soubra, A. H., & Kastner, R., 2008. Three-dimensional face stability analysis of circular tunnels by numerical simulations. In: *Proc., Geotronics 2008*, ASCE, Geotechnical Special Publication vol. 179, pp. 886–893.
- Lake, L.M., Rankin, W.J., Hawley, J., 1992. Prediction and Effects of Ground Movements Caused by Tunneling in Soft Ground Beneath Urban Areas. CIRIA Report 30, Construction Industry Research and Information Association, London.
- Leca, E., Dormieux, L., 1990. Upper and lower bound solutions for the face stability of shallow circular tunnels in frictional material. *Geotechnique* 40 (4), 581–606.
- Leca, E., Panet, M., 1988. Application du Calcul à la Rupture à la stabilité du front de taille d'un tunnel. *Revue Française de Géotechnique* 43, 5–19.
- Li, Y., Emeriault, F., Kastner, R., Zhang, Z.X., 2009. Stability analysis of large slurry shield-driven tunnel in soft clay. *Tunnelling and Underground Space Technology* 24 (4), 472–481.
- Loukidis, D., Salgado, R., 2009. Bearing capacity of strip and circular footings in sand using finite elements. *Computers and Geotechnics* 36 (5), 871–879.
- Maeda, K., Miura, K., 1999. Relative density dependency of mechanical properties of sands. *Soils and Foundations* 39 (1), 69–79.
- Mair, R.J., Taylor, R.N., 1997. Bored tunnelling in the urban environment. In: *Proc. 14th Int. Conf. Soil Mech. Found. Engng.*, vol. 4, pp. 2353–2385.
- Mollon, G., Dias, D., Soubra, A.H., 2010. Face stability analysis of circular tunnels driven by a pressurized shield. *Journal of Geotechnical and Geoenvironmental Engineering* 136 (1), 215–229.
- Ng, C.W.W., Van Laak, P., Tang, W.H., Li, X.S., Zhang, L.M., 2001. The Hong Kong geotechnical centrifuge. In: *Proc. 3rd Int. Conf. Soft Soil Engineering*, pp. 225–230.
- Ng, C.W.W., Li, X.S., Van Laak, P.A., Hou, Y.J., 2004. Centrifuge modeling of loose fill embankment subjected to uni-axial and bi-axial earthquakes. *Journal of Soil Dynamics and Earthquake Engineering* 24 (4), 305–318.
- O'Reilly, M.P., New, B.M., 1982. Settlements above tunnels in the United Kingdom – their magnitude and prediction. In: *Tunnelling '82. Papers Presented at the 3rd International Symposium*, pp. 173–181.
- Peck, R.B., 1969. Deep excavations and tunneling in soft ground. In: *Proceedings of the 7th International Conference on Soil Mechanics and Foundation Engineering*, State of the Art, pp. 225–290.
- Schanz, T., Vermeer, P.A., 1998. On the stiffness of sands. *Pre-failure Deformation Behaviour of Geomaterials* 383–387.
- Schanz, T., Vermeer, P.A., Bonnier, P.G., 1999. The hardening soil model: formulation and verification. *Beyond 2000 in computational geotechnics*. In: *Ten Years of PLAXIS International. Proceedings of the international symposium, Amsterdam, March 1999*, pp. 281–296.
- Soubra, A.H., 2002. Kinematical approach to the face stability analysis of shallow circular tunnels. *Proceedings of the Eight International Symposium on Plasticity* 443, 445.
- Soubra, A.H., Dias, D., Emeriault, F., Kastner, R., 2008. Three-dimensional face stability analysis of circular tunnels by a kinematical approach. *Geotechnical Special Publication* 894, 901.
- Verdugo, R., Ishihara, K., 1996. The steady state of sandy soils. *Soils and Foundations* 36 (2), 81–91.
- White, D.J., Take, W.A., Bolton, M.D., 2003. Soil deformation measurement using particle image velocimetry (PIV) and photogrammetry. *Geotechnique* 53 (7), 619–631.
- White, D.J., Cheuk, C.Y., Bolton, M.D., 2008. The uplift resistance of pipes and plate anchors buried in sand. *Geotechnique* 58 (10), 771–779.

中九龍幹線

Central Kowloon Route



路政署
Highways Department

ARUP  Mott MacDonald

奧雅納-莫特麥克唐納顧問聯營公司
Arup-Mott MacDonald Joint Venture

聲明：凡在《中九龍幹線-設計及建造》過程中向路政署提供意見和建議的個人或團體，將被視作同意路政署可將部分或全部提供的內容(包括個人姓名及團體名稱)公布。如你不同意這個安排，請於提供意見和建議時作出聲明。